# Flexible and Intelligent Human Collaborative Robotics for Non-Destructive Evaluation

Amine Hifi

Department of Electronic and Electrical Engineering

University of Strathclyde

A thesis submitted for the degree of

*Doctor of Philosophy*

November 2025

# Copyright



Signed: 

Date: November 2025

# Acknowledgements

I would like to firstly thank my supervisors Dr Randika Kosala Wathavana Vithanage and Professor Gareth Pierce, for giving me the opportunity to pursue this doctorate and for their continued support over the past three years. I am deeply grateful for the trust you have placed in me, allowing me to explore and develop my many, many ideas.

I want to extend my sincerest thanks to my colleagues and friends in the SEARCH lab group, who have shared their time, patience and expertise with me, making my time as enjoyable as possible.

To my parents, Yasmine and Nabile, I am eternally grateful for your many sacrifices, endless support and for continuing to push me to be better every day. To my brother, Iliane, thanks for listening and laughing to all the terrible stories throughout the years.

This thesis is dedicated to the ones in my heart, my family, my friends and to all those who walked with me throughout the ups and downs.

- Maman! C'est fini!!

…

pour de vrai cette fois!

# Abstract

This research investigates how collaborative mobile robotic systems can overcome long-standing challenges in NDE, specifically the reliance on precise fixturing, predefined component placement, and tightly controlled environments. The overarching aim is to develop inspection systems that maintain or exceed the performance of traditional fixed setups while remaining suitable for shared human–robot workspaces. Through continuous engagement with industrial partners, the work focuses on addressing realistic operational constraints and aligning scientific advancements in system integration and control with practical deployment needs.

The thesis addresses four core objectives: (1) evaluating the feasibility and performance of mobile robotic platforms for high-value manufacturing environments; (2) developing a flexible robotic NDE scanning methodology that reduces or eliminates the need for prior part knowledge; (3) designing and integrating a novel collaborative robotic inspection system that combines established phased-array ultrasonic testing (PAUT) techniques with simultaneous force-position control and 3D vision–based autonomous path planning; and (4) demonstrating a fully automated, human-collaborative mobile NDE system capable of inspecting multiple component types.

Across these contributions, the research advances the concept of process-to-part inspection, enabling robots to autonomously identify components, generate inspection trajectories, and execute complete scans without strict placement requirements. A detailed quantification of mobile manipulator performance provides the foundation for

establishing measurement-science-based benchmarks, while the developed autonomous scanning system demonstrates the feasibility of real-world deployment without relying on fixed fixtures or deterministic part positioning.

Overall, this thesis presents a novel framework for intelligent, collaborative mobile NDE. It demonstrates, the potential for fully automated process-to-part inspections using mobile manipulators working safely alongside humans. The findings highlight the transformative potential of such systems for the aerospace and wider high-value manufacturing sectors, offering a pathway toward flexible, autonomous, and operator-independent inspection technologies, while acknowledging that further qualification and standardisation activities would be required for certified industrial deployment.

# Table of Contents

# List of Figures

# List of Appendix Figures

# List of Tables

# List of Acronyms

| | |
|---|---|
| **AGV** | Automated Guided Vehicle |
| **AI** | Artificial Intelligence |
| **AM** | Additive Manufacturing |
| **AMCL** | Adaptive Monte Carlo Localization |
| **AIP** | American Institute of Physics |
| **AR** | Augmented Reality |
| **ASTM** | American Society for Testing and Materials |
| **BAPS** | British Aerospace Panel Standard |
| **BINDT** | British Institute of Non-Destructive Testing |
| **CAD** | Computer-Aided Design |
| **CAM** | Camera |
| **CFRP** | Carbon Fiber Reinforced Polymer |
| **CT** | Computed Tomography |
| **DOF** | Degrees of Freedom |
| **ECT** | Eddy Current Testing |
| **EMAT** | Electromagnetic Acoustic Transducer |
| **ER** | Enabled Robotics |
| **GUI** | Graphical User Interface |
| **IEEE** | Institute of Electrical and Electronics Engineers |
| **ID** | Identification |

| | |
|---|---|
| **ISO** | International Organization for Standardisation |
| **KAIROS** | Robotnik RB-KAIROS+ Mobile Manipulator |
| **KMP** | KUKA Mobile Platform |
| **KMR** | KUKA Mobile Robot |
| **KUKA** | KUKA Robotics |
| **LBR** | Leichtbauroboter (Lightweight Robot) |
| **MAM** | Mobile Additive Manufacturing |
| **NDE** | Non-Destructive Evaluation |
| **NDT** | Non-Destructive Testing |
| **NIST** | National Institute of Standards and Technology |
| **OBJ** | Object |
| **OS** | Operating System |
| **PAUT** | Phased Array Ultrasonic Testing |
| **PCA** | Principal Component Analysis |
| **PC** | Personal Computer |
| **PSNR** | Peak Signal-to-Noise Ratio |
| **RB** | Robotnik |
| **RGB** | Red, Green, Blue |
| **RGBD** | Red, Green, Blue + Depth |
| **ROB** | Robot |
| **ROS** | Robot Operating System |
| **SD** | Standard Deviation |
| **SICK** | SICK Sensor Company |
| **SLAM** | Simultaneous Localization and Mapping |

| | |
|---|---|
| **SNR** | Signal-to-Noise Ratio |
| **TAURUS** | Tecnatom Automated Ultrasonic System |
| **TWI** | The Welding Institute |
| **TVG** | Time-Varied Gain |
| **UK** | United Kingdom |
| **UR** | Universal Robots |
| **UT** | Ultrasonic Testing |
| **VT** | Visual Testing |
| **WBIS** | Wind Blade Inspection System |

# Chapter 1

# Introduction

## 1.1. Context of Research

Non-destructive Evaluation (NDE) encompasses various methods for testing and evaluating systems and materials to ensure the integrity of structures without damaging the inspected components. This is heavily used in high-value manufacturing, especially in sectors such as aerospace and energy, which design and construct safety-critical components. The NDE global market is growing and is estimated to reach valuations of $35.3 billion by 2032, a rise from the $15.9 billion in 2023 [1]. Showing a rapidly growing industry with immense innovation potential, particularly in the automation and integration of inspection systems.

In NDE, there are various techniques that can be used depending on the applications. These methods include Ultrasonic Testing (UT), radiographic testing, thermographic testing, electromagnetic testing, and visual inspection. With safety-critical components, resolution and sensitivity are two major factors when choosing which technique to apply. Sensitivity in NDE refers to the smallest feature that can be detected by that technique, while the resolution refers to the ability to differentiate closely spaced features [2].

Radiography and UT are techniques capable of achieving the necessary resolution and sensitivities required for inspection and evaluations, capable of inspecting the volume of components. However, as a result of the strict control and safety requirements for the use of radioactive sources, UT is the most commonly used bulk inspection method due to its flexibility, ease of use, and safety [3].

UT detection is based on the method of interaction of the acoustic waves within the medium of interest. This interaction includes the absorption, reflection, scattering, and attenuation of the ultrasonic waves [4]. Phased Array Ultrasonic Testing (PAUT) is a UT variant using multiple ultrasonic elements to enable increased beam scanning, steering, and focusing capabilities by utilising time delays of the transmission and reception of individual elements[5], [6]. The underlying PAUT physics is well established, however, its effective deployment is strongly influenced by probe positioning, coupling conditions, and motion control accuracy.

Traditionally, NDE is performed manually by operators who move probes over the surface of samples and components [7]. Manual inspections require highly trained operators and are a cumbersome task, especially when sample sizes increase. There is a clear need for innovative design in NDE, one such being the automation of NDE processes. Automation would be put in place to fundamentally improve the repeatability of inspections, minimise the total time required for a full evaluation, and ultimately lower operational costs. This has become a priority for high-value manufacturing, with emphasis on time-cost savings associated with the use of automated NDE [8].

The adoption of automated solutions for NDE, both through robotics and Artificial Intelligence (AI), has been coined as NDE 4.0, and is driving the innovation and progress of NDE in the industry: *"The rapid development and integration of advanced technologies such as Artificial Intelligence (AI) and robotics are significantly transforming the landscape of NDE."* [9],[10].

PAUT has been seen to be the preferred bulk NDE method in industries such as aerospace and renewable energy, where it is predominantly used for inspecting high-value, safety-critical components like airplane fuselages and wind turbine structures [11], [12]. Advancements in robotics, particularly the use of industrial manipulators, have further enabled the rapid and precise deployment of UT sensors. Inspections can be conducted using robotics, with components placed in carefully calibrated fixtures and gantries.

Robotic manipulators have become accurate and repeatable to sub-millimetre accuracies [13], and are therefore able to complete inspections to precise margins. Industrial manipulators are limited, however, to known pre-taught paths and the restrictions of their work envelopes. Collaborative robots (Cobots) are a further development of robotic technology, with current robots containing onboard sensors that allow the robot to detect collisions and stop operations [14]. Developments like these have allowed robots to be used outside of cells and enclosures, enabling more collaborative working environments.

The next iteration of these robotic developments has brought forward mobile robotics. There are several types of mobile robots, ranging from drones and crawlers to mobile robotic manipulators; a solution that enables robotic processes to be brought to the components. Robotic mobile manipulators are constructed using a robotic manipulator

mounted onto a movable mobile base. The flexibility of bringing the process to part is an innovation that introduces greater flexibility and adaptability for manufacturing processes, but also introduces additional sources of uncertainty that directly interact with PAUT inspection requirements. The introduction of collaborative mobile robotic platforms combines flexibility for systems and the safety to work in environments with operators, without requiring separate enclosures for robotic manoeuvring.

Utilising modern sensor technologies and algorithms, mobile robotic platforms have shown increased ability and accuracy in localisation and path planning, making them well-suited for bringing the inspection process to the part. Mobile systems introduce greater flexibility and independence from infrastructures, such as gantry-based systems, decreasing the amount of capital equipment required to accommodate components.

### 1.1.1. Definition of Key Concepts

Given the varying interpretations of key concepts and terminologies within the research fields of robotics and automation, it is necessary to clearly define the terminology used in this thesis. To ensure conceptual clarity, and avoiding ambiguity, these definitions help to establish a consistent framework for which this research has been conducted in and explained within the thesis.

The updated ISO 10218-2:2025 [15] removed the classification of collaborative robots as a separate robot type. Instead, collaborative applications are defined as properly risk-assessed operations using industrial robots. In this thesis the term Cobot is retained as an industry-accepted shorthand for industrial robots specifically designed for collaborative

applications. This terminology is used for readability and alignment with existing literature, without implying a separate safety classification under ISO 10218-2:2025.

In the context of this thesis, a Cobot is defined as a robot that is intentionally designed to operate within a shared physical workspace with a human operator, where task execution involves direct coordination.

A human-collaborative environment refers to a setting in which human operators and robotic systems share workspaces and tasks. In this thesis, the term refers to environments in which humans and robots are working within the same workspaces, performing tasks sequentially.

Within this thesis, the terms “fully automated” and “autonomy” refer to the ability of both the algorithms and the hardware to operate without any human intervention.

Flexibility, in the context of this thesis, refers to the increased freedom in positioning of components for inspections within the workspace

## 1.2. Research Aims

This research aims to address the strict requirements for placement-intensive calibrations and precise fixturing of inspection components, while developing systems that are suitable for shared work environments. By achieving results comparable to or exceeding traditional fixed setups, the research aims to enable safe collaboration between humans and robots, reducing the need for separate enclosures or cells for fully autonomous systems. Additionally, the research has incorporated industrial feedback and focuses on solving real-world industrial challenges.

The central scientific question addressed in this thesis is: To what extent can established PAUT inspection performance be preserved when integrated with mobile robotic platforms operating under positioning uncertainty, feedback-driven control, and incomplete geometric knowledge?

This work aims to achieve the following objectives:

- Investigate the usability of mobile robotic platforms for use in high-value manufacturing environments.
- The development of a flexible robotic NDE scanning technology that reduces the need for prior part knowledge and hard-coded component information.
- Design and integration of an innovative system utilising a collaborative robotic arm, integrating PAUT sensing for inspection, simultaneous force-position control, and a 3D vision-based autonomous path planning framework for intelligent component recognition.
- Design and implementation of a fully automated human collaborative mobile NDE system, capable of inspecting various components.

## 1.3. Knowledge Contribution

The knowledge contributions produced as a result of the work of this doctorate are outlined below:

- Evaluation of current robotic technologies through accuracy and repeatability, in the context of NDE requirements, to identify limitations and areas for improvement.

- Development of a fully automated and flexible robotic NDE scanning system that eliminates the need for prior knowledge of part geometry, precise fixturing, or complex programming by incorporating computer vision to automatically generate efficient scan paths for complex geometries representative of real industrial aerospace components, thereby reducing human intervention in path generation.
- Implementation of a fully automated, flexible mobile robotic NDE solution incorporating station-based alignment algorithms, computer vision–based part recognition to extract components from station environments, ultrasonic feedback for optimised coupling, and automated report generation, enabling comprehensive inspection of multiple components and stations with enhanced efficiency without operator intervention.
- Advancement of system integration know-how, encompassing the automation of programming, computer vision–based path planning, AI-driven defect detection, and the coordination of advanced NDE instrumentation and subsystems, highlighting interconnectivity, system engineering, and integration methodology as the primary scientific contributions of this work to enable fully automated inspection workflows.

## 1.4. System Requirements and Success Criteria

To assess the effectiveness of the proposed mobile robotic NDE system, a set of measurable requirements and success criteria has been defined. These criteria reflect both the technical demands of the PAUT inspection and the practical constraints associated with deployment.

Acceptable system performance requires as the ability to autonomously complete inspections without human intervention, while maintaining stable probe contact, reliable ultrasonic coupling, and repeatable scan execution across multiple components and deployments. The system should position and maintain the ultrasonic probe during PAUT inspection, despite uncertainty introduced by mobile base localisation and incomplete prior knowledge of component geometry.

From an inspection perspective, success requires consistent and interpretable ultrasonic data. This includes repeatable signal quality along inspection paths, controlled coupling conditions, and minimal degradation due to positioning or force-control errors, so that inspection performance remains comparable to established fixed or manually deployed PAUT systems.

## 1.5. Thesis Structure

This thesis has been structured as follows:

- **Chapter 2:** Presents the research background, further investigating the motivations behind this work. Reviewing previous research into robotic NDE and robotic applications and identifying the research gap addressed by this work.
- **Chapter 3:** Presents the investigation for the deployment of mobile collaborative robots in high-value manufacturing. Focusing on an investigative procedure aimed at understanding the accuracy and repeatability associated with mobile collaborative robots.
- **Chapter 4:** Explores the work developed for an operator-independent adaptable system used for NDE. The chapter describes the various modules created and investigated to combine a vision system, with adaptable path planning and simultaneous force-position controlled PAUT inspection. Concluding analyses highlight validation findings and evaluate the system's operational capabilities.
- **Chapter 5:** Presents the research and development of a fully automated collaborative mobile robotic NDE solution, detailing the integration of vision, control, and ultrasonic testing (UT) for a comprehensive inspection system. The chapter concludes with validation results and a discussion of system performance.
- **Chapter 6:** This chapter summarises and concludes the work done during this doctorate and discusses how this work could be extended in the future.

The structure of the thesis and the interrelations between its chapters is illustrated in Figure 1.1.

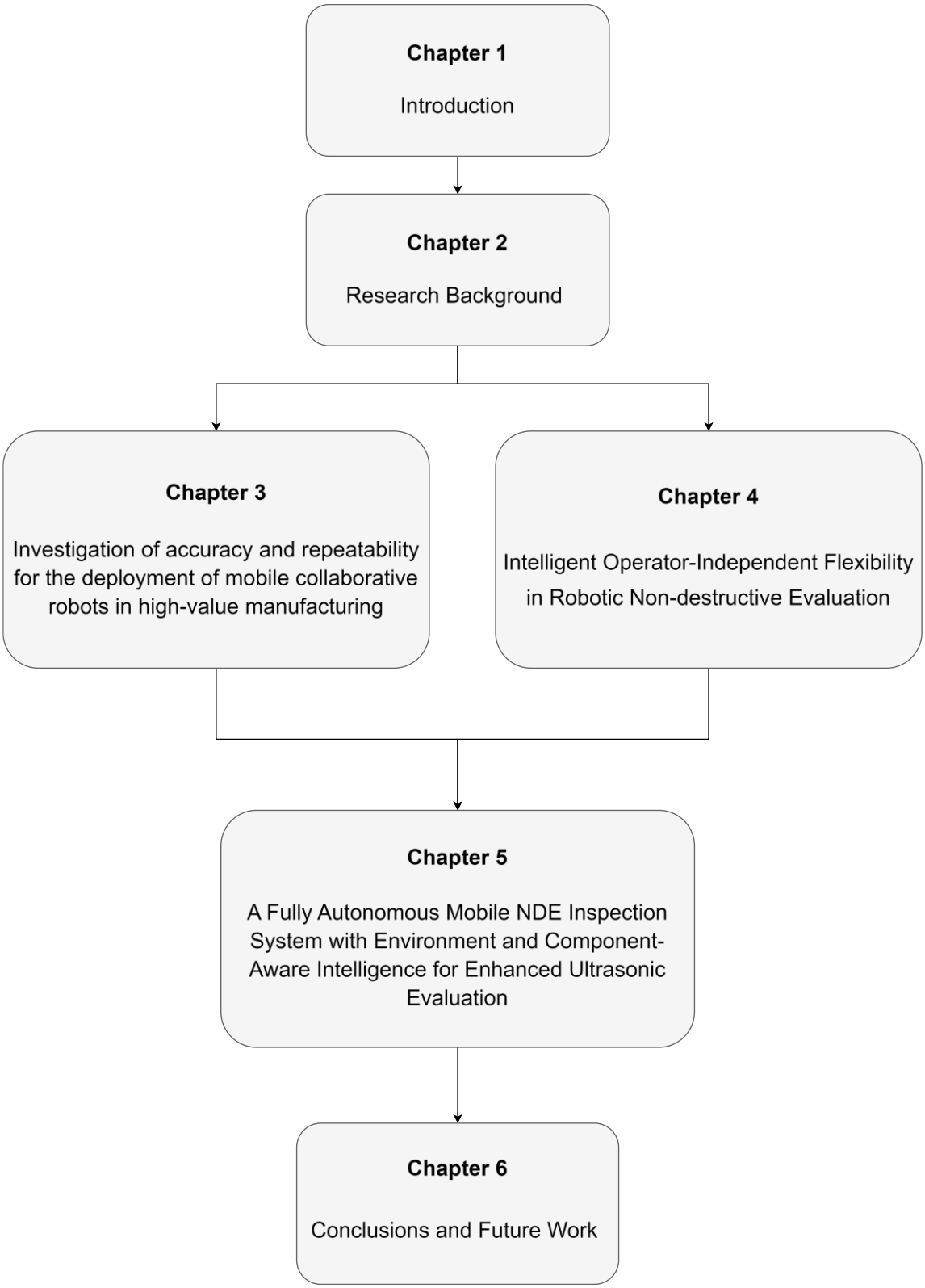


*Figure 1.1. Structure of Thesis*

## 1.6. Publications

### 1.6.1. Journal Contributions

Lead author journal publications arising from the work produced by this thesis:

- **A. Hifi**, W. Jackson, C. Loukas, M. Shields, A. Poole, E. Mohseni, S. G. Pierce, C. N. MacLeod, G. Dobie, T. O'Hare, G. Munro, J. O'Brian-O'Reilly, R. K. W. Vithanage, *"A quantitative investigation of accuracy and repeatability for deployment of mobile collaborative robots in high-value manufacturing",* IOP: Measurement Science and Technology – **Published August 2025** and explored in Chapter 3.
- **A. Hifi**, S. McKnight, V. Tunukovic, E. Nicolson, R. Gomes, R. K.W. Vithanage, E. Mohseni, A. Poole, S. G. Pierce, T. O'Hare, G. Munro, "*Intelligent Operator-Independent Flexibility in Robotic Non-destructive Evaluation",* Wiley: Advanced Intelligent Systems – **Published January 2026**, explored in Chapter 4.

Co-author journal publications are outlined below:

- V. Tunukovic, S. McKnight, **A. Hifi**, E. Mohseni, S. G. Pierce, R. K. W. Vithanage, G. Dobie, C. N. MacLeod, S. Cochran, T. O'Hare, *"Human-machine collaborative automation strategies for ultrasonic phased array data analysis of carbon fibre reinforced plastics"*, NDT&E – **Published September 2025**.

- S. McKnight, V. Tunukovic, **A. Hifi**, S. G. Pierce, E. Mohseni, C. N. MacLeod, T. O'Hare, *"3-DUSSS: 3-Dimensional Ultrasonic Self Supervised Segmentation"*, Engineering Applications of Artificial Intelligence – **Published August 2025.**

### 1.6.2. Conference Contributions

Lead author conference contributions are outlined below:

- Oral presentation at the BINDT Aerospace Event, April 2023, titled "*A study of the accuracy and repeatability of mobile collaborative robots for non-destructive evaluations".*
- Oral presentation at the 50th Annual Review of Progress in Quantitative Non-destructive Evaluation (QNDE), July 2023, titled *"Flexible robotics for automated non-destructive testing".*

Co-author conference contributions during the doctorate are outlined below:

- R. Gomes, E. Mohseni, S. G. Pierce, K. Burnham, **A. Hifi**, C. N. Macleod, V. Maes, M. Chandler, A. Barnes, & G. Munro. (2024). *"Detection of out-of-plane waviness in carbon-fibre reinforced plastics: comparing different non-destructive evaluation modalities"*, 2024 IEEE SENSORS – Conference paper.
- S. McKnight, V. Tunukovic, **A. Hifi**, S. G. Pierce, E. Mohseni, C. N. MacLeod, T. O'Hare, *"3D Ultrasonic Self-Supervised Segmentation for Composite Components"*, 2024 IEEE UFFC-JS – Oral presentation

- G. Pierce, E. Mohseni, R. K. Wathavana Vithanage, A. Poole, **A. Hifi**, M. Shields, M. Vasilev, C. Loukas, C. N. MacLeod, G. Dobie, J. O'Brien-O'Reilly, G. Munro, T. O'Hare, M. Grosser, & A. Oakley, *"Considerations for process to part inspection for flexible manufacturing NDT",* 60th Annual British Conference on NDT (BINDT) – Oral presentation
- R. K. Wathavana Vithanage, K. C. Burnham, M. Vasilev, C. Loukas, **A. Hifi**, A. Poole, R. Zimermann, D. Lines, C. N. MacLeod, G. Pierce, A. Gachagan, S. Williams, J. Ding, T. O'Hare, G. Munro, & J. O'Brien-O'Reilly. *"Flexible robotics to inspect aerospace components"*, BINDT Aerospace Event 2023 – Oral presentation.
- R. K. Wathavana Vithanage, A. Poole, G. Pierce, **A. Hifi**, C. N. MacLeod, M. Vasilev, G. Dobie, T. O'Hare, G. Munro, & J. O'Brien-O'Reilly, *"Process to part inspection of composites"*, BINDT Aerospace Event 2023 – Oral presentation.
- E. Mohseni, S. G. Pierce, R. W. K. Vithanage, C. N. MacLeod, G. Dobie, S. McKnight, V. Tunukovic, M. McInnes, **A. Hifi**, R. Gomez, M. Shields, A. Poole, R. Pyle, T. O'Hare, G. Munro, & J. O'Brien-O'Reilly, *"Mapping SEARCH capabilities to Spirit AeroSystems NDE and automation demand for composites",* BINDT Aerospace Event 2023 – Oral presentation.

# Chapter 2

# Research Background

## 2.1. Overview of NDE Techniques

In NDE, various techniques can be used depending on the application. Some of the common NDE methods are radiographic testing, eddy-current testing, visual inspection, and Ultrasonic Testing (UT), the technique this thesis focuses on using.

### 2.1.1. Ultrasonic Testing

UT is the most commonly deployed NDE inspection type [3]. UT uses an ultrasonic transducer that generates acoustic waves that propagate through the material and listens to returning waves reflected or scattered by acoustic impedance changes. The sound waves used are in the frequencies above the human hearing range, with most NDE applications using frequencies between 1-10 MHz [16]. With its ability to adjust various parameters such as voltage, frequency, and ultrasonic configuration, UT is versatile and allows for full volumetric penetration. The technique allows for accurate defect detection, as well as the ability to size, locate, and characterise defects.

Piezo-electric transducers are the most widely used method for generating and detecting ultrasound for NDE. These transducers can be constructed as single elements, dual

elements, or in an array structure. Single-element probes function in whereby the signal is transmitted and received from the same transducer. Dual-element probes feature separate transmit and receive elements, and arrays are capable of using multiple elements to send and receive signals. The dual and single element transducer configurations are illustrated and annotated in Figure 2.1.

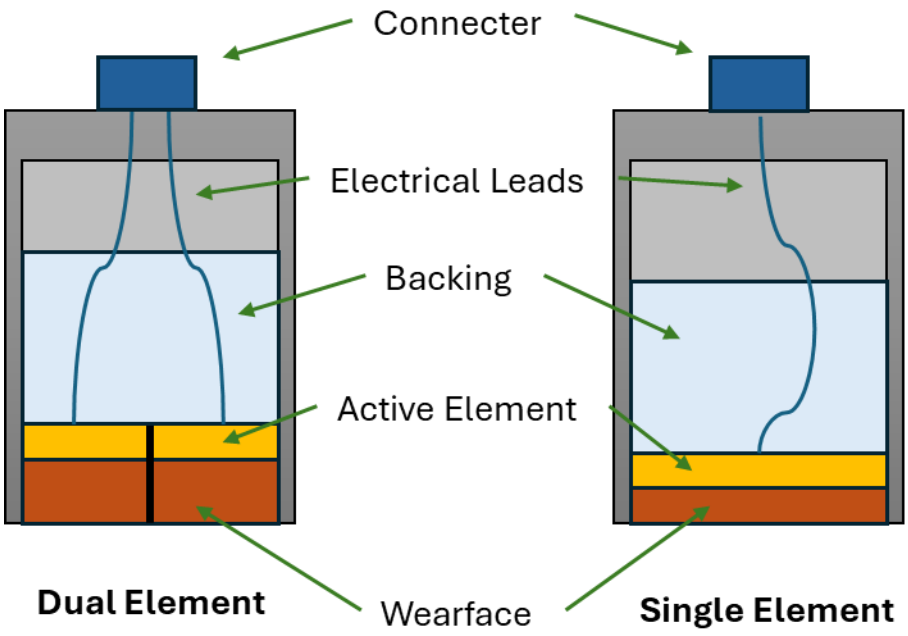


*Figure 2.1. Dual and Single Element Transducer Schematics*

Piezo-electric ultrasound transducers typically require a liquid coupling medium (coupling gel, oil, or water[17], [18]) to transfer the ultrasound energy into the inspection component. UT requires an effective coupling medium to transfer ultrasonic energy, as air is highly attenuative at Megahertz (MHz) frequencies and a poor transmitter of ultrasonic waves. Furthermore, the significant mechanical impedance mismatch between air and materials causes substantial reflection at the material–air interface, of air gaps, which can

arise from air gaps created by defects such as delaminations or debonds, severely limiting the amount of energy transmitted. Inspections can be conducted using the transducer and coupling directly on the surface of a component or can be done in immersion.

Another type of transducer is the electromagnetic acoustic transducer. A variation of which is the magnetostrictive transducer, which operates based on the magnetostrictive effect — a phenomenon where a ferromagnetic material changes its dimensions when exposed to an alternating magnetic field. Rapid and repeated deformation of the material generates mechanical vibrations, which in turn produce ultrasonic waves. [19], [20]. These transducers can be referred to as Electromagnetic Acoustic Transducers (EMAT), and are single-element transducers; however, they are not so widely used due to their limited frequency capabilities. [21].

PAUT is a UT variant that utilises multiple ultrasonic transducers. These are arrays of transducers arranged in a specific configuration, whereby each array element is capable of independently generating and detecting ultrasound. The array elements are linked together and can be controlled by applying time delays to the electrical signals, allowing the manipulation of the ultrasonic beam characteristics. The adjustments of time delays allow the control of the beams for steering and focusing capabilities[5], [6]. Figure 2.2 a) shows a linear beam imaging approach where all the elements are fired simultaneously. Figure 2.2 b), c), and d) show the effects of different firing delays and how they can generate focused and steered beams.

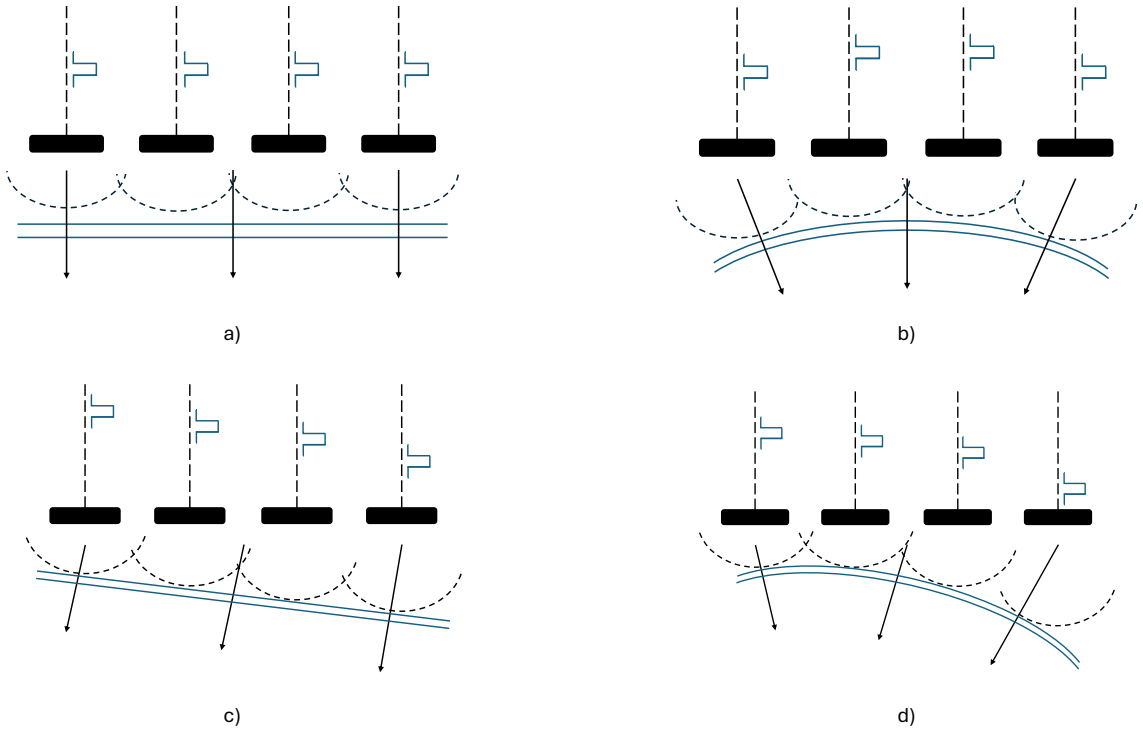


*Figure 2.2. PAUT beam forming with respective firing delays for (a) Linear Beam, b) Focused Beam, c) Beam Steering, d) Focused and Beam Steering*

Ultrasound phased arrays are available in 1D and 2D element configurations, facilitating 2D and 3D ultrasonic imaging, respectively [22].

#### 2.1.1.1. Non-Contact Ultrasonic Testing

One non-contact method of generating and detecting ultrasound is using lasers [23]. It has the benefit of being applied from a range of distances from a sample. Some applications have reached a generation from tens of meters away from the target, making it a possible solution for non-contact applications [24].

Laser ultrasound utilises a pulsed laser to generate surface vibrations by exposing the material to short laser pulses. The energy from the laser pulse causes localised heating,

leading to thermal expansion and the creation of surface waves (i.e., ultrasonic waves)[23]. These waves then propagate through the material.

The detection of these waves is typically done using a second laser. This laser is used to monitor the surface displacement caused by the propagating ultrasonic waves. The reflected light is analysed using interferometry to measure the surface motion, allowing for the characterisation of the material's internal properties, such as defects or thickness variations.

Similarly to piezo-electric transducers, there has also been work on the development of phased arrays for lasers. This has been done both with a single laser source using multiple optical delays and using multiple laser sources. The first method uses a single laser source, which is then split and delivered to the target following a range of optical delay paths to attain the desired time delay. This has been achieved by using multiple optical fibres of variable length [25]. The second method uses an array of laser cavities, fired at the desired time delay [26]. These solutions both offer a unique ability for imaging at a higher resolution than the standard laser ultrasound but bear the disadvantage of a much higher cost for setup.

Laser ultrasound has been in various high-value manufacturing applications such as the inspection of composite parts from F-22 and F-35 fighters, detection of cracks and flaws in metals, and in additively manufactured components. [27].

One major disadvantage of the use of laser-based systems is the strict requirements. Lasers are classified based on their power output and class 2 lasers can cause flash-blindness and

dazzling. Class 3 lasers are more powerful and can cause eye damage, increasing with exposure time. Class 4 is the most powerful laser and is hazardous to the eyes and skin. The use of higher-class lasers is strictly governed by the Control of Artificial Optical Radiation at Work Regulations 2010 [28], [29].

#### 2.1.1.2. Displaying Ultrasonic Data

Ultrasonic data is visualised in a range of formats to allow the user to interpret and understand the information more easily. There are three commonly used methods for displaying UT data being the A-scan, B-scan, and C-scan. Each of these methods presents its benefits for displaying the information during inspection.

Ultrasonic inspection data is initially acquired as an amplitude versus time signal, commonly referred to as an A-scan. This is the most fundamental and widely used display format in ultrasonic testing, serving as the basis for all other representations [30]. A-scan signals can be visualised in various forms, including the native radio frequency (RF) waveform, a fully rectified signal, or as either the positive or negative half-wave of the RF signal, depending on the operator's preference [30]. A sample A-scan is presented in Figure 2.3, simulating a hole-like defect.

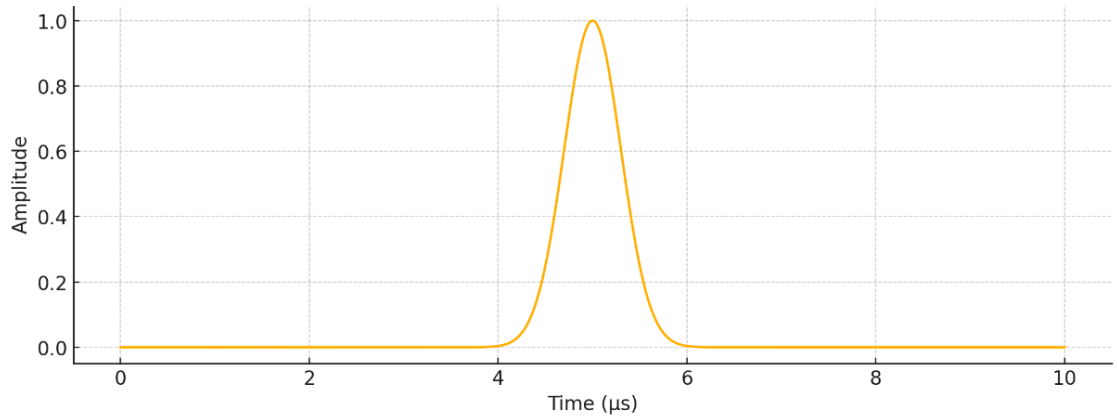


*Figure 2.3. Sample A-scan.*

By aligning successive A-scans along the axis of transmission, a B-scan image can be generated. This format presents a two-dimensional cross-sectional view of the test object [31]. B-scans are particularly common in PAUT and assist in interpreting defect locations and depths. A sample B-scan is shown in Figure 2.4, based on the A-scan from Figure 2.3. The hole-like feature is better visualised using the B-scan method.

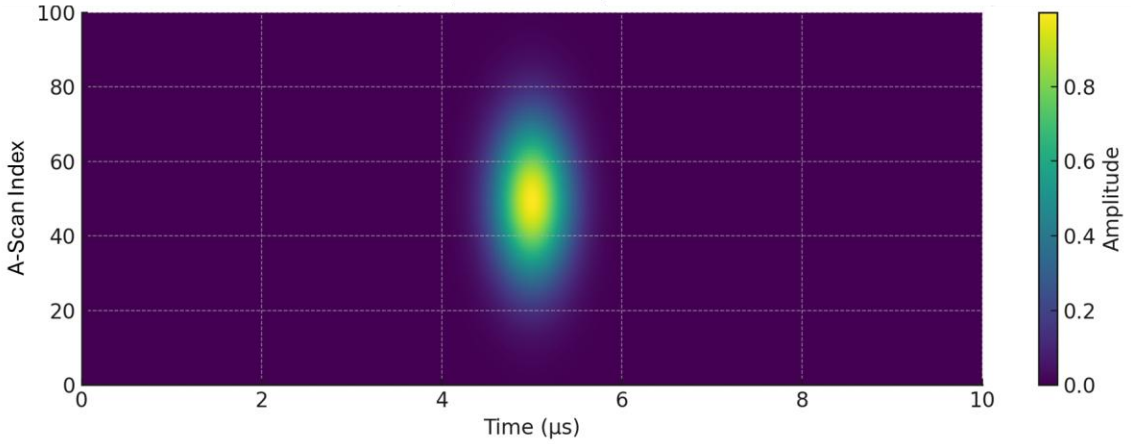


*Figure 2.4. Sample B-scan.*

A C-scan provides a plan-view, two-dimensional image parallel to the surface of the component under test. This format is produced by gating the A-scan signal to extract a

single data point from each position, which is then represented using a colour map [32], [33]. These C-scan displays can help to enhance interpretability for operators and analysts as they offer a more intuitive representation of flaw distribution or material loss across a surface area. The sample C-scan shown in Figure 2.5 is based on the A-scan data presented in Figure 2.3. The C-scan shows the best view of the hole feature as compared to the A-scan and B-scan.

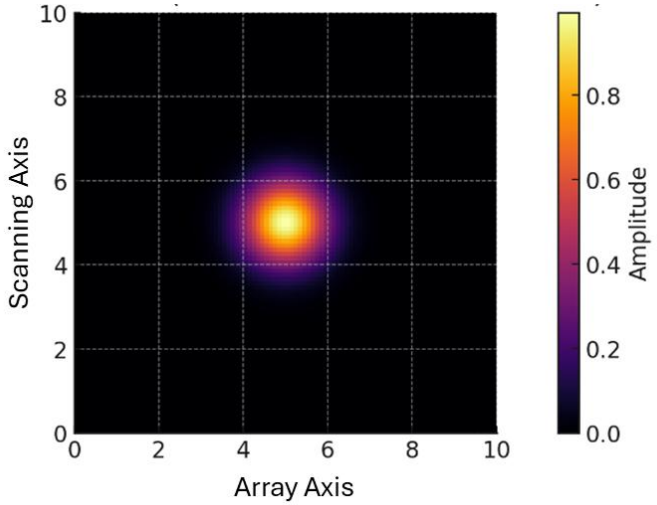


*Figure 2.5. Sample C-scan.*

## 2.1.2. Other NDE techniques

### 2.1.2.1. Radiography

Radiography, more specifically X-ray radiography, is conducted by using a radioactive source to transmit high-energy electromagnetic radiation into a target sample. Radiography has the major advantage of achieving high-resolution imaging. Advancements in x-ray technology have allowed imaging resolution down to as low as 1 μm, with some x-ray setups even reaching around <0.1 μm [34]. These are for imaging a

wide range of materials, including ceramics, composites, and metals. X-ray systems are capable of analysing internal material properties and structures with a high degree of precision. The use of X-ray radiography is also extended past a simple receiver and transmitter, with the development of computed tomography (CT). CT was developed during the 1960s and 1970s and has been heavily utilised in the medical sector. CT was the first to image the human body noninvasively, that were not influenced by the overlapping of different anatomical structures [35]. CT offers an exceptional method for non-destructively imaging the internal structure of materials, with a resolution range from meters down to tens of nanometres. It takes advantage of the penetrative capability of X-rays to produce a series of two-dimensional (2D) radiographs captured from multiple angles around the object, a process commonly known as a CT scan. Using a reconstruction algorithm, these 2D projections are then compiled into a stack of cross-sectional slices. This results in a digital 3D representation (referred to as a tomogram) of the object's internal structure in greyscale. This tomogram can be quantitatively analysed, sliced in any direction, and specific components can be digitally colour-coded or made transparent to highlight the 3D morphology [36].

Radiography-based solutions offer a lot of advantages, but do, however, have a series of disadvantages, which means that they are not the most prominently used inspection methods.

Large material density and thickness are aspects that affect imaging capabilities for X-rays. Attenuation in the X-ray is observed with the increase of material thickness. This can be somewhat compensated for by increasing the tube power; however, the trade-off

then comes at the cost of a reduction in resolution. Resulting in an inability to inspect thicker and denser components at higher resolutions. Another disadvantage of radiography solutions is the cost.

The cost of purchasing an X-ray source, detector, and rotary stage for CT can range from 100,000 to over 1 million USD. [37]. A system has been constructed for a price of 35,000 USD; however, it is limited to components of size <100 mm [38]. The size of the components required for inspection has a direct correlation with the cost of the system. These costs also do not take into account the energy costs required to power and run the CT systems for acquisitions.

The fact that there is ionising radiation requires strict Health & Safety procedures to be put in place, and is another key disadvantage of using radiography.

#### 2.1.2.2. Eddy-Current Testing

Eddy-Current Testing (ECT) is another commonly used NDE technique that utilises alternating electromagnetic fields to identify defects within components. It is well suited for inspecting the surface and sub-surface of conductive samples, typically metals.

ECT work by using alternating currents (AC) that pass through a coil, generating a magnetic field that oscillates at the frequency of the current. When this coil is placed near a conductive material, the magnetic fields induce circulating currents, known as eddy currents, within the material. These induced eddy currents flow in closed loops within the conductive material. When a defect, such as a crack or corrosion, is present, it disrupts the flow of eddy currents, causing changes in their amplitude, phase, or frequency. These

changes are detected by the sensor coil, which measures variations in the impedance of the coil due to the altered electromagnetic field caused by the presence of the defect.

ECT operates at the surface of components and is highly effective for detecting any discontinuities on or near the surface of the inspected samples. Since it is capable of detecting near-surface indications, it has the advantage of being able to inspect surfaces that are painted or coated. For this reason, one use of ECT is for the accurate thickness measurements of coatings [39]. ECT is deployed relatively fast and requires minimal surface preparation. One of its advantages is that it can be mounted permanently to a fixture or end-effector and is a portable and lightweight solution. The main disadvantage of ECT is that it is unable to image or inspect further than the surface or near-surface regions of a component, providing limited information about the internal volume. This limitation arises from the material's skin depth, where high-conductivity materials restrict eddy currents to the surface, while lower-conductivity materials allow for slightly greater penetration, though sensitivity remains largely surface and near-surface.

#### 2.1.2.3. Visual Testing

Visual Testing (VT) is considered the simplest and most inexpensive NDE technique. Despite its basic nature, it is crucial in identifying surface-breaking defects, which can often have the most significant impact on the strength and safety of a component. Such defects, which could compromise the structural integrity of a material, are visible to the naked eye upon careful inspection. This visibility enables the immediate identification of issues, allowing for prompt rejection or repair of the component. As a result, VT can

prevent the need for more expensive and time-consuming inspection methods, offering a practical first step in the evaluation process.

## 2.2. Overview of current robotic technologies

Within the manufacturing industry, a variety of robots are used with the aim of improving precision, safety, and productivity within the pipeline. The most used types are industrial robotic arms and human-collaborative robots (Cobots). Figure 2.6 shows a Cobot (a) and an industrial robot (b). The main visual difference between the two robots is the absence of pinch points on the Cobot, an intentional design feature aimed at reducing the risk of injury. Cobots also generally feature more rounded designs and are smaller in size than industrial robots; however, it should be noted that Figure 2.6 is not to scale.

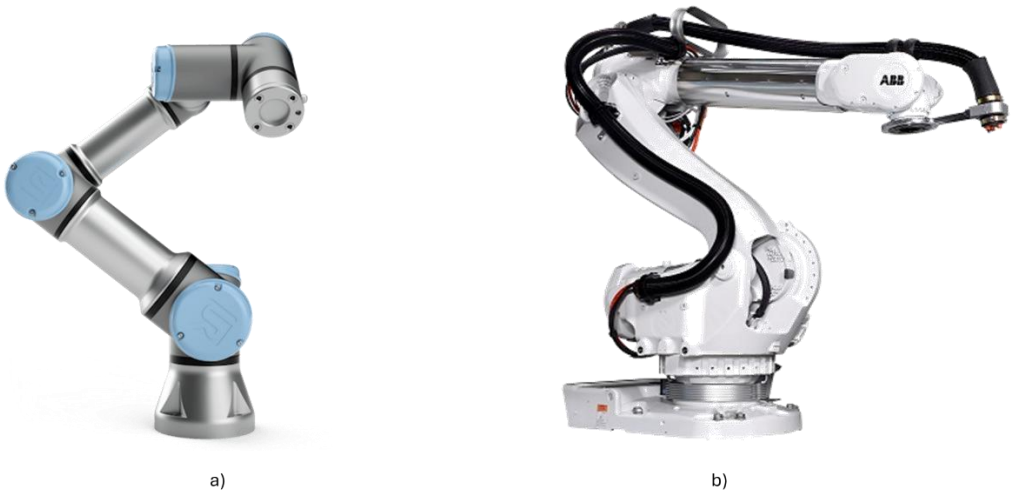


*Figure 2.6. Robotic Manipulators a) Cobot [40], b) Industrial robot [41]*

Recently, mobile robots have gained significant popularity due to their ability to achieve significant flexibility in navigating environments. Mobile robots offer versatility, as their configuration, size, and mode of transport can be adapted to suit the needs of the

application. These mobile platforms are used for a variety of tasks like inspection, grinding, and logistical operations.

In robotics, accuracy and repeatability describe two distinct aspects of positional performance. Repeatability refers to the robot's ability to return to the same position regardless of how close that position is to the intended target. Accuracy, in contrast, describes how close the robot's achieved position is to the true, physical location in space. A robot may therefore be highly repeatable, with the ability to return to the same point consistently, while still exhibiting poor accuracy if its absolute position deviates from the true coordinates.

Manufacturers have been seen to provide very limited information regarding these metrics, or, where values are provided, they are heavily idealised and unable to perform at the quoted values [42].

Industrial robotic arms, as the most commonly used robots, are utilised in manufacturing for tasks such as inspection, assembly, pick-and-place, and welding. These robots are usually articulated, meaning they feature multi-joint configurations, typically 6-axis, which allow them to execute more complicated motion paths, with six Degrees of Freedom (DoF) [43], [44]. The usefulness of robotic arms, capable of lifting various loads depending on the size and their repeatability, makes them suitable for various applications, including automotive, electronics, logistics, and pharmaceuticals [44], [45]. Their ability to execute pre-taught programs accurately and repeatedly enhances their functionality and usefulness in high-volume production lines, significantly improving operational efficiency. Despite their widespread use in manufacturing, traditional industrial robotic

arms present several challenges and limitations. These systems often lack the flexibility and reconfigurability required for applications involving complex geometries or frequent task changing. Additionally, many industrial robots require fixed installations and safety enclosures such as safety fences, which significantly increase spatial and infrastructure demands. The capital expenditure (CAPEX) and non-recurring costs (NRC) associated with setup, integration, and maintenance can be substantial, particularly in low-volume or customised production settings. These systems typically also require specialised programming skills, resulting in high programming overheads and limiting accessibility for non-expert users. These constraints collectively reduce the cost-effectiveness and scalability of industrial robotic arms, especially in situations where parts and components change often.

Cobots represent a class of articulated robots designed to collaborate with human operators. The desire for automation in industry has highlighted the importance of human-robot collaboration, where the accuracy, repeatability, and speed of robots complement human operators [46], [47]. Cobots are particularly advantageous in environments where tasks require flexibility and adaptability, allowing for a more dynamic interaction between humans and machines [46]. This collaboration can lead to safer and more efficient manufacturing processes. A crucial factor for operators collaborating with robots is trust, which is why Cobots feature onboard sensors and safer builds to ensure the safety and well-being of operators around. The onboard joint torque sensors enhance safety by continuously monitoring the torque at each joint. In the event of a collision, if the measured torque exceeds a predefined safety threshold, a collision detection protocol is

activated, which either locks the joints or engages the brakes. These collision detection algorithms are proprietary and vary between Cobots, but the underlying principle remains the same. Based on the force or torque detected, the protocol may temporarily halt the robot, assess whether the force persists, and either resume the task or fully terminate operation.

Within mobile robotics, there exist two main types commonly used in industrial manufacturing applications. These are defined as Autonomous Mobile Robots (AMRs) and Automated Guided Vehicles (AGVs).

Autonomous Mobile Robots (AMRs) are equipped with navigation and perception systems that enable them to operate autonomously within a manufacturing environment. These platforms leverage the onboard sensors and algorithms to map their surroundings, navigate complex layouts, and avoid obstacles, making them particularly well-suited for dynamic environments and interactions with human operators [48],[49]. Their integration into manufacturing processes reflects a broader shift toward increased automation and system connectivity [50]. An example of an AMR is the KUKA KMP 3000 mobile platform, which features omnidirectional movement, a payload capacity of up to 3 tons, and the option to mount a robotic manipulator, as shown in Figure 2.7.


*Figure 2.7. KMP 3000 mobile platform [51]*

AGVs, in contrast, are programmed to follow predefined paths and are primarily used for transporting goods within a facility. They typically rely on guiding systems for navigation, such as strips on the ground, which limits their flexibility compared to AMRs [49]. AGVs are frequently utilised in repetitive tasks where their predictable routes contribute to efficiency and safety [52]. While AGVs are less adaptable than AMRs, they can be implemented into an established workflow simply which is a great advantage. Additionally, their simpler operational structure often requires fewer onboard systems and lower initial implementation costs.

Mobile manipulators combine the mobility of a mobile platform with the manipulation capabilities of robotic arms. This integration allows the systems to navigate through a manufacturing space while performing their tasks, such as assembly or inspection [48]. The flexibility gained from merging a robotic arm with a mobile base enables the freedom to deploy these robots in various locations as required, offering significant versatility, especially in environments that are frequently reconfigured or adapted to new tasks [53]. An example of a mobile manipulator is the KUKA KMR iiwa, featuring omnidirectional

movement similar to the KMP 3000, but with the added benefits of the LBR iiwa Cobot, as shown in Figure 2.8. This robot has 7 degrees of freedom from the LBR manipulator, and a further 2 degrees of freedom from the platform base.


*Figure 2.8. KUKA KMR iiwa mobile manipulator[54]*

Mobile robots designed for applications within manufacturing, such as inspection, often incorporate technologies such as machine vision and AI to enhance their functionality. Vision-guided robots, for example, can identify and manipulate items on production lines, significantly improving the flexibility of the system, accuracy, and speed in handling tasks [55]. Tailored mobile robotic solutions are increasing in demand, with a clear need for automation solutions that can address unique, flexible challenges in manufacturing settings.

## 2.3. Robotics in NDE

### 2.3.1. Need for Automated NDE

As part of the shift towards NDE 4.0, there has been a great amount of interest in introducing and capitalising on "smart" technologies [56]. One of the smart technologies of interest is utilising robotics for automating the process of NDE inspection.

A motivating factor for this shift is the increasing average age of NDT operators. Although recent survey data is lacking, trends from 2006 to 2014 indicated a rise in the average age from 41 to 48 years [57]. Similarly, a 2007 survey of British Institute of NDT (BINDT) members revealed that 60% of the 1,600 respondents were over the age of fifty [58]. While efforts have been made to attract new entrants through apprenticeship schemes, these initiatives have seen limited success due to low enrolment and high dropout rates [59].

In addition to the ageing workforce, several other factors have driven growing interest in automation within NDE. Safety remains a significant concern, particularly in high-risk environments such as nuclear, oil and gas, or aerospace sectors, where operators are often required to work in dangerous environments. Automated systems reduce the need for human presence in such environments, thereby minimising exposure to physical risks.

Ergonomics is another motivating factor. Many traditional NDE tasks involve repetitive, strenuous, or difficult manual operations that can lead to operator fatigue. Automation offers a solution by offloading physically demanding tasks to robotic systems, which can improve working conditions and reduce injury-related downtime.

Repeatability and consistency are also critical in inspection routines, especially when high volumes or complex geometries are involved. The automated systems are capable of maintaining consistent inspection parameters and positioning across multiple operations, thereby improving data reliability.

The potential for human error remains a major limitation in manual NDE processes. Interpretation of results, probe placement, and calibration can vary between operators, leading to discrepancies in defect detection and characterisation. Automation not only enhances precision but also enables integration with advanced data analysis and machine learning algorithms to further reduce subjectivity and improve defect identification.

### 2.3.2. Commercial systems

This section will discuss some of the commercial systems currently used in the NDE sector.

#### 2.3.2.1. The Welding Institute IntACOM

The Welding Institute (TWI) has developed an inspection system called IntACOM [60], which is composed of a dual industrial robotic manipulator setup. This setup utilises a water jet–coupled UT system to inspect various components positioned on a test bench. The inspection system can inspect with the dual arms independently or in unison. When working independently, the ultrasonic inspection is done using pulse-echo, meaning the sending and receiving of the ultrasound is done by the individual probes. When the arms are working synchronously, they can inspect using through-transmission, meaning that one probe sends and the other probe receives. The system uses 3D Computer-Aided

Design (CAD) of the components to generate path planning. The system is shown below Figure 2.9.


*Figure 2.9. TWI IntACOM robotic setup[60]*

The benefit of a water jet-coupled UT inspection is that it allows the inspection process to be completed without making contact with the sample. Not making contact with the sample can be beneficial, especially when inspecting complex geometries. However, a downside is that the robots have to be aligned on each side of the inspection components. This can become a greater challenge with complex components, and issues with synchronisation between robots have been shown to cause misalignments between 0.186mm to 1.108mm [61]. The use of the water jet-coupled UT means that there has to be a proper drainage setup to remove all of the running water. The setup also has to be fixed and precise to ensure that the inspection is carried out properly. The use of industrial

robots also limits the space and requires strict safety measures, such as guarding, to be in place.

#### 2.3.2.2. Tecnatom Systems

Tecnatom is a Spanish company that has great capabilities in the NDE sector with various solutions ranging from magnetic particle testing to ultrasound and radiology [62]. They have been partnered with and providing NDE solutions to aerospace companies for over ten years [63], demonstrating the first commercial system to use phased array through-transmission testing (PATTU) to significantly reduce the time of component inspections. Their focus on R&D has meant that solutions are delivered to accommodate the needs of customer inspection requirements.

They have four main solutions [64], WiiPA – their wireless manual NDE solution, which combines PAUT with motion capture to enable flexibility and traceability into the inspection process. To be used with parts of varying complexity from flat to curved geometries. BACUS – an immersion inspection platform, which does immersion scanning for bars, billets, or plates. With target use in industrial and nuclear environments. INLINE – a high-speed production line inspection system, integrated straight into the factory pipeline. The system also uses PAUT to provide real-time inspection results of tubes and bars to support continuous operations.

The last system, TAURUS – a robot-based inspection system that supports ultrasonic techniques such as pulse echo, PAUT, and through-transmission (TTU). This is the system used within aerospace for parts such as skins. This is their most robust system, utilising

industrial robot manipulators to perform inspections on complex components such as composite or metallic parts. Their system is shown in Figure 2.10.

*Figure 2.10. Tecnatom TAURUS system [64]*

Tecnatom systems benefit from end-to-end development, with proprietary software tightly integrated with their in-house hardware solutions.

#### 2.3.2.3. ACCUBOT

The ACCUBOT is a commercial system, developed by Fill [65], [66], a machine engineering/plant construction company. The system has been developed for its use in the

composite manufacturing industry, with its aim of addressing the need for precise inspection along curved edges and spherical surfaces. The system is shown in Figure 2.11.


*Figure 2.11. ACCUBOT NDE system design*

The design incorporates the use of secondary encoders, combined with a high-order kinematic model for real-time compensation, claiming accuracy of 0.15mm. This level of precision may be attributed in part to the use of STÄUBLI manipulators, which are themselves capable of positional accuracies of ±0.02 mm. [67]. This precision is the most attractive feature of the ACCUBOT, making it suitable for use in CAD-based processes in the aerospace manufacturing industry. Their system is mounted in various configurations, from tracks to gantries with a range of NDE payloads.

#### 2.3.2.4. Eddyfi VersaTrax

The Eddyfi VersaTrax [68] is a mobile robotic inspection crawler, developed by Eddyfi, an established developer of NDE technologies. The VersaTrax system is designed for conducting inspection, maintenance, and NDE in complex and hazardous environments. These systems are specifically engineered to perform tasks that traditionally require human operators in confined, difficult-to-reach, or dangerous spaces.

The crawlers are equipped with sensors enabling them to navigate confined spaces such as pipelines, storage tanks, and reactors. They are designed to allow traversing a variety of surfaces, including steel, concrete, to ensure they are adaptable for a broad spectrum of inspection tasks. NDE payloads of VersaTrax crawlers include UT and ECT, which allow for the evaluation of material integrity and condition. They are used for identifying issues such as corrosion, cracks, and structural weaknesses within safety-critical structures. The VersaTrax crawlers are also customisable, with the systems able to be tailored with different payloads and sensor configurations. The crawler design is shown in Figure 2.12.

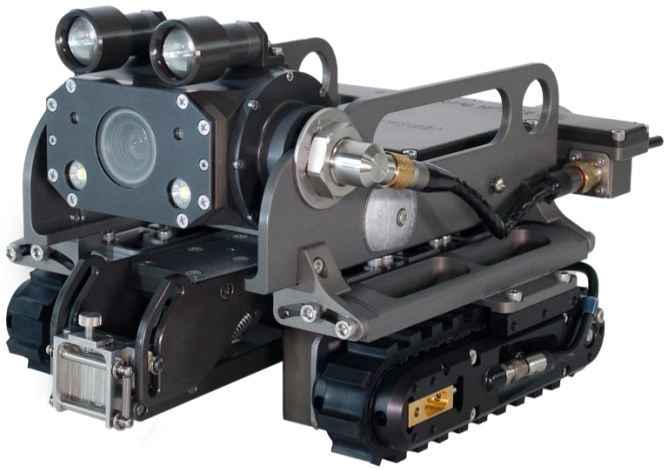

*Figure 2.12. Eddyfi VersaTrax crawler[68]*

Inspection crawlers, with their ability to navigate challenging environments, perform advanced non-destructive testing, and reduce risks associated with human labour, make them valuable tools for ensuring the safety, reliability, and longevity of critical infrastructure across various industries.

#### 2.3.2.5. Evident WBIS

The evident Wind Blade Inspection System (WBIS) is a concept that has been advertised by Evident, a subsidiary of Olympus [69]. This concept showcases a Cobot mounted onto an AGV with a Phased Array mounted on the flange, shown in Figure 2.13.

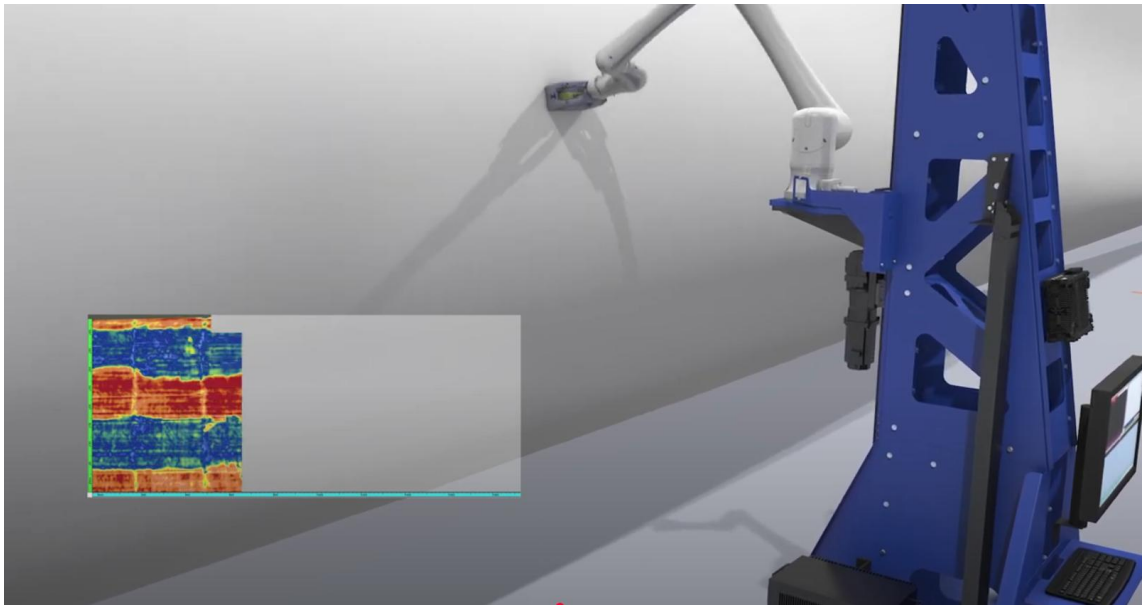

*Figure 2.13. Evident WBIS system inspecting the Carbon Fiber-Reinforced Polymer (CFRP) sample.*

The system was designed with the aim of inspecting large components such as Carbon Fiber-Reinforced Polymer (CFRP) wind blades. CFRP is a composite material widely

used for its high strength-to-weight ratio and fatigue resistance, typically comprising multiple layers of carbon-fibre plies impregnated with a resin matrix. The Evident system is proposing teaching a start and end point, and then allowing the automated system to complete the inspection process. The AGV utilises onboard sensors to navigate the environment in case the path is blocked. The inspection process utilises feedback of the component's shape from the Cobot and navigates its raster scans without the use of CAD programming.

A solution such as this is the future of inspection systems. Utilising mobile systems that can bring the inspection process to the part will help to streamline the overall inspection operations. Allowing for components to be specified within a mapped environment and allowing the inspection to move rather than requiring precise calibrations and lifting to ensure components are in exact positions.

The concept proposed by Evident is very sought after within manufacturing [70], but the WBIS, remains a concept, with just a rendering of the system being available. The development of a mobile collaborative system that can be fully automated is something that is worthwhile pursuing.

### 2.3.2.6. Summary of Systems

A summary of the commercial systems presented in the above section is listed in Table 2.1.

*Table 2.1. Summary of commercial system features*

| System | TWI IntACOM | Tecnatom Systems | ACCUBOT | Eddyfi VersaTrax | Evident WBIS |
|---|---|---|---|---|---|
| **Deployed** | Yes | Yes | Yes | Yes | No |
| **Robot Setup Type** | Dual KUKA industrial robots | Various systems built around industrial robots | Dual STÄUBLI-based arms on a track system | Crawler System | Mobile Cobot |
| **NDE Technology** | Water jet-coupled UT | PAUT | Various, including-Water jet-coupled UT and X-ray | EC and UT | PAUT |
| **Inspection Scenarios** | Various component types | Various components in manufacturing | Various component types | Pipes, storage tanks, and reactors | CFRP wind blades |
| **Space Required** | Large Specialised Enclosure | Large Specialised Enclosure | Large Specialised Enclosure | Minimal, the system is flexible and mobile | Minimal, the system is flexible and mobile |

The trend flow of robotics in industry is highlighted below in Figure 2.14, showing the current interest in mobile manipulator systems.

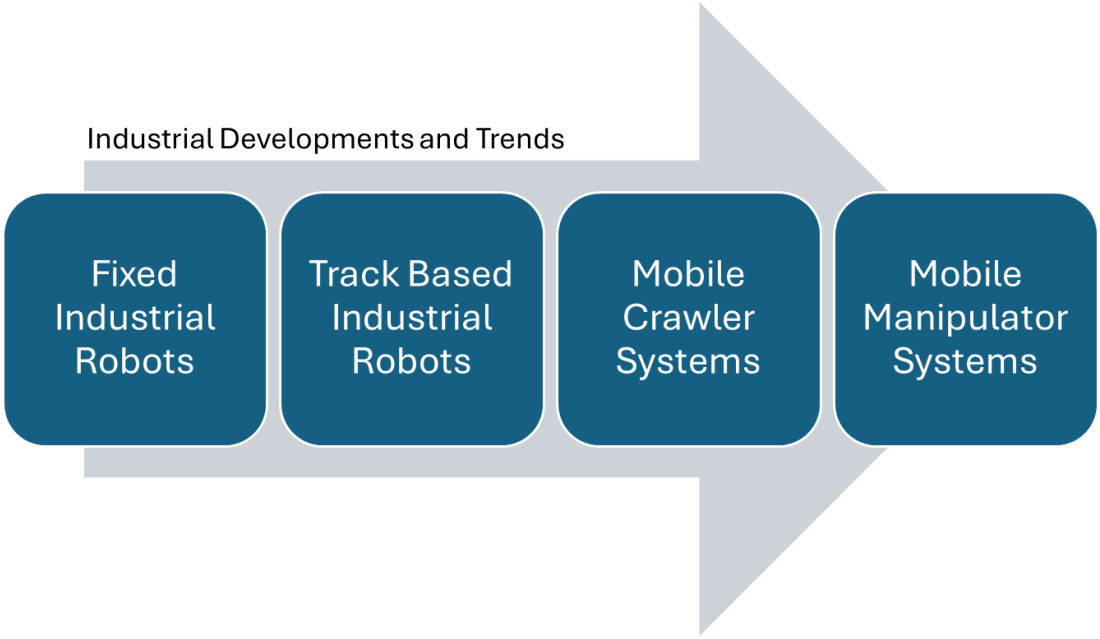


*Figure 2.14. Industrial developments and trends for robotics*

## 2.4. Mobile Manipulator Applications

### 2.4.1. Current Mobile Manipulator Solutions

Mobile manipulators are becoming increasingly popular due to their capabilities in mobility and accurate onboard manipulator. There are various mobile manipulator solutions available on the market, each with its benefits. Some of the popular commercial solutions include the Robotnik RB-KAIROS+[71], the ER-FLEX [44], the Clearpath Husky [73], and the KUKA KMR iiwa [54].

#### 2.4.1.1. RB-KAIROS+[71]

The RB-KAIROS+, developed by Robotnik, is a mobile manipulator designed for indoor applications, particularly in industrial and logistics environments. Its compact steel-framed structure is optimised for navigating confined spaces, while the omnidirectional

Mecanum wheels provide enhanced manoeuvrability, enabling multidirectional movement in cluttered and dynamic settings. This agility makes the RB-KAIROS+ particularly well-suited for applications requiring spatial efficiency. The system is presented in Figure 2.15.

*Figure 2.15. Robotnik RB-KAIROS+ mobile manipulator*

The RB-KAIROS+ can support a payload capacity of up to 250 kg. This makes it suitable for handling significant loads in a variety of industrial environments, where material transport is essential. Additionally, the platform's modular architecture, based on the Robot Operating System 2 (ROS 2), facilitates flexibility and customisation, allowing the robot to be tailored to meet the specific needs of diverse operational tasks.

The RB-KAIROS+ utilises Universal Robots (UR) as the onboard manipulator [40]. Its compatibility with UR means the various-sized manipulators can be used, allowing for a completely tailored build.

For safety, the RB-KAIROS+ is equipped with dual 2D safety scanners and an RGBD, which captures both colour (RGB) and depth (D) information, camera, which facilitate secure navigation and interaction within dynamic environments. Additionally, the robot employs a Simultaneous Localisation and Mapping (SLAM)-based localisation system, ensuring precise navigation in complex indoor spaces. These safety and navigational features are required for the robot's usability in environments where there is a human operator present.

However, some potential limitations of the RB-KAIROS+ may arise from its reliance on specific hardware integrations and configurations.

For instance, although the robot's design offers substantial flexibility, the scalability of such a system may be limited due to its reliance on UR e-Series manipulators and, therefore, may not be suitable for all environments or industries.

#### 2.4.1.2. ER-FLEX [74]

The ER-FLEX, developed by Enabled Robotics [74], is another mobile manipulator combining the mobility of an autonomous platform with the versatility of a collaborative robotic arm.

A strength of the ER-FLEX lies in its modular design, similar to the RB-KAIROS+, which supports various configurations and customisable module heights. This feature allows for the integration of different UR manipulators depending on the specific payload and reach requirements. The ER-FLEX design is displayed in Figure 2.16.

*Figure 2.16. ER-FLEX modular mobile manipulator [74]*

The system is integrated with the ER-ABILITY platform, a web-based interface designed for programming and task scheduling. The platform supports block-based drag-and-drop programming, making the setup process more accessible to users without extensive technical expertise. Moreover, the ER-FLEX supports integration with existing infrastructures to ensure that the robot can be incorporated into existing workflows.

The robot is also equipped with dual 2D laser scanners and 3D cameras for safety and navigation, allowing the detection of obstacles and adjusting its path accordingly. Its design, therefore, enables it to operate alongside human workers without the need for safety fences, optimising the use of floor space within industrial settings.

A key difference between the platforms is the wheel design of the ER-FLEX. The system uses a combination of two centrally located powered drive wheels with four castor wheels [75]. The drive wheels provide propulsion, while the castor wheels offer balance and enable rotational movement. This configuration effectively makes the system a powered

trolley. This type of drive system is best suited for environments with smooth, even floor surfaces.

Similarly to the RB-KAIROS+, the reliance on the robotic arm options available might not be suitable for all industries or specific tasks. These manipulators are not suitable for heavy payloads or mounting large sensors on the flange, and they may also struggle to reach larger or more complex components. The need for a compatible robotic arm may limit the system's flexibility in some cases, depending on the specific application or the weight and reach requirements.

#### 2.4.1.3. Clearpath Husky[73]

The Clearpath Husky is a rugged unmanned ground vehicle (UGV), designed for mobile autonomy, inspection, and outdoor deployment. It is a widely adopted platform for research and development applications [76], [77]. Constructed with an aluminium chassis, the Husky is rated for operations in cold, wet, and challenging terrains. The platform is presented in Figure 2.17, showing the base model in Figure 2.17 a) and the manipulator model offered by Clearpath in Figure 2.17 b).


a) b)

*Figure 2.17. Clearpath Husky a) Base Model, b) Platform with manipulator configuration[73]*

The system uses skid-steer drive, with the latest model offering four brushless motors for the drive system, to deliver the torques required for outdoor use and differential steering [78]. Unlike omnidirectional wheels, which enable lateral and rotational movement, or the castor-wheel system found on platforms like the ER-FLEX, skid steering involves turning by varying the relative speed of wheels on each side of the vehicle. While effective for rough terrain, this design can lead to occasional wheel slip, making precise movements and complex turns more difficult to execute reliably.

The platform is built on the ROS2 architecture [79], which brings the flexibility of open source and customisation. This enables users to choose their sensors for perception and navigation, as well as select from a range of manipulators to suit specific research or operational needs [80].

#### 2.4.1.4. KUKA KMR iiwa [54]

The KUKA KMR iiwa is an autonomous mobile robot that integrates the capabilities of KUKA's LBR iiwa lightweight Cobot with a mobile platform, facilitating human-robot collaboration and enabling a broad range of industrial applications. The LBR iiwa features seven revolute joints, each equipped with in-built joint torque sensors, allowing the robot to detect external contact and respond accordingly. This feature enables the KMR iiwa to perform tasks in proximity to humans without the need for safety barriers, which enhances workspace efficiency. The in-built joint torque sensors allow for the estimation of end effector forces without the need for external sensors. Additionally, the robot's mobile platform is equipped with laser scanners for autonomous navigation, enabling it to detect obstacles and adapt its movement in dynamic environments. It also includes encoders that enable it to operate without requiring a pre-mapped or known environment.

The KMR iiwa is designed with Mecanum wheels [81], which provide omnidirectional movement and the ability to rotate 360 degrees. This feature enhances the robot's manoeuvrability, enabling it to navigate through tight spaces and reduce idle times within manufacturing environments. Furthermore, the platform offers an important level of precision, with a manufacturer-quoted positioning accuracy of up to ±5 millimetres. This would make the KMR iiwa suitable for applications that demand careful handling and placement, such as those found in electronics assembly or automotive manufacturing. The robot is equipped with KUKA.NavigationSolution, which allows for dynamic path planning and reliable obstacle avoidance and further enhances its operational capabilities.

A great advantage of the KMR iiwa is its scalability within the KUKA range, with the platforms and manipulators having scalability dependent on the application requirements.

#### 2.4.1.5. Summary of Systems

A summary of the features of the compared robotic manipulators is compiled into Table 2.2.

*Table 2.2. Summary of mobile manipulators' features*

| Feature | RB-KAIROS+ | ER-Flex | Clearpath Husky | KUKA KMR iiwa |
|---|---|---|---|---|
| **Primary Function** | Material transport and manipulation | Collaborative mobile manipulator | Academia, autonomy, mapping, | Mobile collaborative robotics for Human-robot collaboration |
| **Safety Features** | Dual 2D safety scanners, RGBD camera | Dual 2D laser scanners, 3D cameras | E-stop buttons | Joint torque sensors, laser scanners |
| **Navigation System** | SLAM-based localisation system | Integrated with a navigation system | Programmable via ROS | KUKA.NavigationSolution, dynamic path planning |
| **Omnidirectional Movement** | Yes (Mecanum wheels) | Yes (Castor wheels) | No (Differential drive) | Yes (Mecanum wheels) |
| **Integration with Existing Systems** | Flexible integration with IT infrastructure | Seamless integration with IT infrastructure | Programmable via ROS | Requires compatibility with existing systems |
| **Applications** | Industrial material transport, manipulation | Machine tending, material handling, and laboratory automation | Mobile autonomy, inspection, and outdoor deployment | Collaborative tasks, precise handling, and dynamic environments |
| **Intelligence and Software** | ROS 2 for customisation | ER-ABILITY web-based platform, drag-and-drop programming | ROS 2 | Integrated KUKA.NavigationSolution, obstacle avoidance |

### 2.4.2. Advanced Mobile Manipulator Applications

With the increased interest in mobile manipulators, there have been several developments academically.

#### 2.4.2.1. Robotic Chemist

One such application of mobile manipulators was for research into a mobile robotic chemist [82], to accelerate chemical discovery through autonomous experimentation. The robot position was measured for over 563 movements, which showed that the (x, y) positioning precision was better than ± 10 mm, and orientation within ±2.5°, sufficient for moving between stations but not for fine tasks like vial placement. Precision was improved using a touch-sensitive 6-point calibration on cubes at each station, enhancing accuracy to ±0.12 mm and ±0.005° orientation. This calibration enabled delicate manipulations and instrument operation.

Over eight days, the system autonomously performed 688 complex experiments, handling reagents, protocols, and monitoring without human intervention. This automation increased throughput and reduced labour. The robot used a Bayesian optimisation algorithm to efficiently explore a ten-variable experimental space, selecting promising conditions based on prior data rather than random testing.

Notably, the robot identified photocatalyst mixtures with sixfold improved catalytic activity and autonomously refined its experimental strategy by favouring beneficial components and discarding harmful ones. This self-directed decision-making reduced human bias and expanded the scope of discovery.

The system's technical capabilities included precision pipetting, titration, and real-time analysis, all operating autonomously. The study showcased the powerful combination of robotics and machine learning to automate and optimise scientific research, highlighting potential applications beyond the lab, including manufacturing.

#### 2.4.2.2. Concrete Additive Manufacturing

Within the manufacturing industry, there have also been developments for the use of mobile manipulators. An application that has been explored is Additive Manufacturing (AM), in the construction industry [83].

Mobile Additive Manufacturing (MAM) systems represented an emerging technology that offered scalability by enabling the cooperation of multiple mobile robots on individual 3D printing tasks. These systems' mobility and autonomy allowed for deployment in both new and existing construction contexts, providing the flexibility to coordinate operations with direct and indirect human interaction. The MAM system is presented in Figure 2.18.

*Figure 2.18. Collaborative mobile robot platforms used for in situ AM with clay 3D printing systems[83].*

Context-awareness was identified as a critical factor for the success of MAM systems. This capability allowed for the fabrication of building components in the correct location and with the necessary alignment. Accurate localisation was achieved through a combination of global tracking via markers or marker-less tracking, and relative localisation to the workpiece. This approach enabled precise positioning of mobile systems, which was essential for collaboration between multiple mobile robots in performing construction tasks. The ability to maintain accurate alignment, even in dynamic and changing environments, allowed for seamless continuation of building components.

Collaboration between humans and robots emerged as another significant advantage of MAM technology. The autonomy of MAM systems enabled robots to carry out highly precise tasks requiring geometric accuracy, while humans could focus on more complex, cognitively demanding work. This interaction opened new possibilities for design flexibility in AM of buildings, with robots complementing human workers by performing tasks that required high geometric precision, force-adaptivity, or substantial payload capacity. The synergy between human expertise and robotic precision promised to enhance productivity and accuracy on construction sites.

#### 2.4.2.3. Automated Mobile Robotic Welding System

In response to the welding challenges in industry, a mobile robotic welding system that integrates a mobile manipulator was proposed[84]. This system was designed to autonomously perform welding tasks across construction sites, offering the flexibility to move through large and complex environments without the need for fixed, stationary rigs.

The results demonstrated that the mobile robotic welding system could autonomously execute welding tasks with high precision and consistency. The system successfully navigated complex construction environments and adapted to dynamic conditions.

The mobile robotic welding system offered several significant advantages over traditional welding methods. The ability to operate continuously without breaks improved overall efficiency, particularly in large-scale construction projects. The automation of the welding process ensured uniformity in weld quality, reducing variability and the potential for errors that were common in manual welding. The mobility of the robot also provided

flexibility, enabling it to be deployed at various locations on the construction site, adapting to various project requirements. Additionally, by removing humans from high-risk welding tasks, the system enhanced safety on the job site.

However, further research was required to refine the system's capabilities, particularly in terms of enhancing its autonomy, scalability, and adaptability to varied materials and environmental conditions. By combining autonomous navigation, real-time positioning, and precise welding techniques, the system addressed critical challenges such as labour shortages, inefficiencies, and variability in welding quality.

#### 2.4.2.4. Mobile Manipulators for Assistive Work

Another application that has been investigated, thanks to the human collaborative nature of some of these mobile manipulators, has been utilising the system for assistive work, such as transferring parts across to a different location. The authors of this work investigated the case of utilising a KUKA KMR iiwa R820 manipulator mounted on top of a KUKA KMP 200 mobile platform [54], [85]. They conducted a test of accuracy for the movement between a home point and another defined point on the map. The manipulator was equipped with a 3-finger adaptive gripper to move an aluminium bar with the help of an operator. The robot would grasp the bar and would be helped by an operator holding the other side. The manipulator went into compliance mode, measuring the positional offset and force condition values. Based on the haptic feedback from the human operator, the mobile platform moved accordingly along the X or Y axis, on the way to the location of the drop-off. They reported that **"***The maximum deviation of error along the x and the y axis is 0.01257% and 0.006% respectively."*

However, the setup and details of the experiment were not well described. Overall, the study concluded that humans and robots can effectively work together, with the robot enhancing task efficiency and performance.

#### 2.4.2.5. Ultrasonic Inspection Mobile Manipulator

A full-sized mobile platform with a robotic manipulator that can conduct an ultrasonic inspection does not yet exist; however, the use of crawlers and smaller platformed robots has been investigated. The authors of this work developed a teleoperated system that utilised PAUT, a vision system, and a laser to create a solution capable of perceiving its environment and navigating the piping systems that it was designed to inspect [86].

#### 2.4.2.6. External Sensing Capabilities

From the literature, it is clear that for high accuracy applications, the utilisation of external sensors such as vision systems or calibration squares improves accuracy significantly. The performance of mobile manipulators can vary depending on the environment, surface conditions, and wear of the wheels.

To address positional uncertainties, vision systems have been proposed as a solution. It has been recognised as the most effective method for tackling positional inaccuracies for mobile manipulators [87]. The vision system was able to achieve compensation with an average offset of just 0.19 mm, outperforming alternative methods such as fine positioning and Light Detection and Ranging (LiDAR) feedback in terms of correcting positional errors.

Another study explored the use of a dual-arm mobile robot on a shop floor and revealed that relying solely on the SLAM algorithm often resulted in positioning errors of 50-100 mm [88]. However, by incorporating ARTags and a vision system, these errors were reduced to 10 mm or less. The concept of significantly reducing positional errors by more than 80% through the integration of a vision system has proven to deliver considerable improvements. This not only benefits existing mobile systems but also offers significant potential for future platforms, emphasising the importance of incorporating integrated vision systems to enhance accuracy.

## 2.5. Limitations and Gaps in Existing Research

Current literature has primarily focused on the implementation of automated solutions for inspection tasks. These systems have demonstrated high accuracy in inspecting components, but typically rely on fixed setups. A major limitation of such systems is the need for precise positioning and pre-teaching of the components, which significantly increases the overall initial inspection time. This becomes particularly evident in low-volume, high-mix production environments. Such systems increase overheads, placing them beyond the reach of many Small and Medium-sized Enterprises (SMEs), as these firms must either maintain in-house robotic capabilities or pay for external integrators and programmers.

In efforts to improve adaptability, where teaching of points and poses is not required, fixed manipulators still present physical constraints. Components must be transported to and evaluated within a single static setup which limits flexibility and efficiency. These setups

also require careful safety precautions to ensure that no humans can enter the area, with enclosures having to be constructed.

The introduction of human collaborative robots has greatly simplified setups and work environments, and allows for humans and robots to work within the same space. This advancement has opened new possibilities for flexible inspection processes.

Although some research has explored the use of Cobots in NDE, there remains a significant gap in the development of fully automated, flexible Cobot-based NDE systems that do not require prior component information or operator involvement. Specifically, the literature lacks exploration into the use of mobile manipulators for fully automated NDE tasks.

While custom-built mobile robots have been studied and quantified for performance, there is no established procedure or validation for their application in NDE. Furthermore, there is currently no fully automated mobile manipulator system for PAUT that operates independently of human input and incorporates automated decision-making.

This thesis aims to address these gaps by investigating and presenting flexible NDE solutions that utilise both Cobots and mobile robotic manipulators. These systems are designed to enhance flexibility and safety in NDE environments while maintaining the accuracy and defect detection capabilities of traditional fixed manipulators.

The concept of process-to-part inspection is introduced in this thesis, which looks to bring the inspection processes to the component. This approach removes the need to transport components to inspection cells, enhances flexibility, reduces logistical demands, and

enables inspections to be conducted anywhere within the manufacturing environment. The proposed solution also has positive implications for capital cost reduction and minimizes the need for skilled operators to program inspection routines. Finally, the thesis presents a complete pipeline for an operator-independent environment in which components can be placed without teaching, using sensors and algorithms to autonomously detect and inspect components.

# Chapter 3

# A quantitative investigation for the deployment of mobile collaborative robots in high-value manufacturing

## 3.1. Introduction

As introduced in Chapter 2 – Section 2.2, mobile robotic platforms, particularly for warehouse management, are frequently employed for moving goods between stations. Mobile manipulators combine a mobile platform with an onboard multi-axis manipulator. Currently, mobile manipulators have not been extensively used in high-value manufacturing applications, operating autonomously at full capacity, although some examples of their applications are discussed in Chapter 2 – Section 2.4.2. Several factors have impacted the adoption of mobile manipulators, including the costs associated with their implementation, uncertainties in accuracy and repeatability and challenges of floor surface conditions. Additionally, the shortage of qualified personnel to operate these systems and the necessity for updated safety protocols to handle the systems correctly are also significant factors [89].

While fixed arm robots are widely used for automation of cumbersome and repetitive procedures such as welding, metrology, positioning, assembly and inspection in high volume production lines, they are relatively inflexible when it comes to adapting to new components, different component orientations, or new operations [90]. This is because any changes require recalibration of critical aspects such as positioning and path planning. As a result, the environments in which they operate tend to be designed to accommodate the robot's limitations. This is why some businesses opt for manual labour methods instead, especially when dealing with high-mix and low-volume production components [91]. Additionally, reach limitations require installations of additional external axes to introduce more DoF and machining of appropriate gantries or fixtures to handle the components. For instance, aerospace components are often large (>3 m) and necessitate customised systems for manufacturing processes [92] where such systems lack the adaptability and flexibility, introducing delays in manufacturing and impacts on production throughput.

To enhance automation uptake, new methods and processes must be designed to be able to adapt to all aspects of the manufacturing operations, and the introduction of collaborative mobile robotic platforms is one possible solution. Utilising modern sensor technologies and algorithms, mobile robotic platforms have shown increased ability and accuracy in localisation and path planning, making them a candidate for bringing inspection processes to the part.

The target manufacturing process of this chapter is NDE, a non-intrusive method used to evaluate the properties of materials, components, or systems. By using NDE, defects and

irregularities can be detected early on, helping to ensure that no manufacturing or operational non-conformities occur.

A range of NDE sensors can be mounted on robotic manipulators; however, their deployment requires careful configuration. Depending on the sensor used, it may be necessary to maintain direct contact with the component surface or operate at a predefined offset. In both cases, the sensor must also be maintained at specific orientations to optimise signal transmission and data quality. Unlike static robotic manipulator systems, which are calibrated once and used repeatedly, mobile robotic platforms introduce additional variability due to platform movement and the presence of two extra degrees of freedom. Due to the need for precise and reliable results in these procedures, an in-depth analysis of mobile manipulator capabilities is warranted, accompanied by the establishment of attributes that define their performance.

By implementing a mobile manipulator solution, the manufacturing process can be streamlined substantially [93]. A mobile solution that can work with a range of sensors and tools, with the ability to travel to different sections of the production line on a factory floor, means there is no longer any need to have several divided areas of a factory, when the process can come to the part. This can therefore reduce the factory footprint substantially, introducing reductions in costs for overheads and equipment. Mobile manipulators can contribute throughout the entire lifecycle of manufactured goods, from production to disposal, creating a more fully automated process pipeline.

Industry 4.0, synonymous with smart manufacturing, has driven the need for a digital revolution within the industrial sector. While advanced technologies such as AI and data-driven systems support greater efficiency and autonomy in industrial operations, the rising demand for productivity and the shortage of skilled labour are the primary drivers behind increased automation across various industries [8],[94], [95]. The manufacturing industry, in particular, has been identified as having the highest potential for automation due to its repetitive processes and scalability requirements [96]. While automation improves job efficiency and has economic benefits, not all tasks can be automated, creating a need for hybrid work environments combining manual labour with automation [96]. Collaborative Mobile manipulators are seen as a flexible solution to bridge this gap, as they can navigate and adapt to different environments and tasks effectively. Additionally, their collaborative nature allows them to operate safely alongside human workers, reducing the need for isolated cells or safety guarding and enabling a more seamless integration into existing workflows.

At present, the International Organisation for Standardisation (ISO) standard ISO 24647 sets out the criteria for robotic ultrasonic testing, but it does not include mobile manipulators [97]. ISO standard ISO 9283 establishes standardised testing methods for accuracy and repeatability in industrial manipulators [98], however, no equivalent standard currently exists for mobile manipulator platforms, particularly regarding repeatability, accuracy procedures, or the specific requirements of PAUT applications.

Therefore, this work aims to complete a set of tests that will help determine whether the mobile manipulators can achieve the necessary precision required for PAUT inspections.

Any inevitable errors must then be quantified to determine how they can be compensated. This work looks to address this gap by evaluating mobile manipulators in a measurement science context, emphasising the importance of establishing quantifiable performance benchmarks such as repeatability and positional accuracy.

Several popular mobile platforms were considered for this work, including the RB-KAIROS+ and ER-FLEX [71], [72]. These platforms have a range of features, such as built-in vision systems and integrated Universal Robot arms onboard [40]. Ultimately, the KUKA KMR iiwa [51] was selected for these experiments - shown in Figure 3.1 , due to its robust build, integrated laser sensors, omnidirectional Mecanum wheels, and the scalability offered by KUKA's variety of robot systems available. The scalability within the KUKA product range presents the opportunity for the lab-environment developments to be transferred to larger industrial robots or to combinations of industrial manipulators with the KMP 3000 platforms, which have reaches of 2.7 to 3.0 meters.

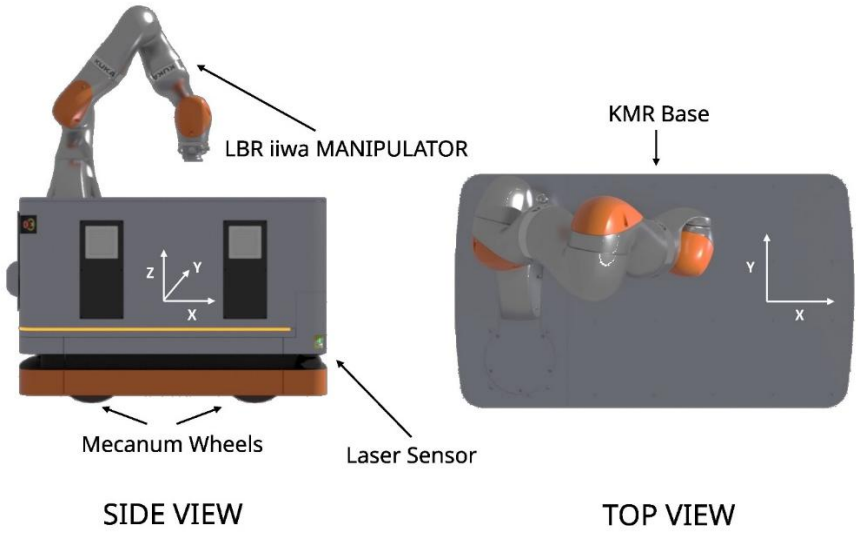


*Figure 3.1. KUKA KMR iiwa mobile manipulator (The coordinate frame refers to the KUKA KMR base frame)*

The KMR platform has been studied for various applications; for example, by using its mapping features and the manipulator onboard the robot, the KMR could open and traverse through doors [99] and the Simultaneous Localisation and Mapping (SLAM), along with Adaptive Monte Carlo Localisation (AMCL), allowed the KMR to create a map of its environment and accurately locate itself within it. The AMCL algorithm uses particles to represent the robot's possible configurations and adjusts their weights based on sensor data to converge towards the actual position. To improve accuracy, additional laser scans are taken in front of the door, and the robot aligns itself with the door to transform its frame relative to the door's frame. This strategy of realigning after an initial movement can be applied to high-value manufacturing for accurate platform positioning.

The accuracy of the inspection process relies on precise positioning and scanning to identify defects accurately. The performance of the mobile platforms can vary, depending on the environment and surface conditions. A vision system has been proposed to mitigate positional uncertainty and has been identified as the most effective approach for this purpose [87]. The concluding results demonstrated that the vision system could compensate for positional errors with an offset of just 0.19 mm, outperforming alternative methods such as fine positioning and LiDAR based feedback.

In [88] a dual-arm mobile robot was investigated for its ability to navigate a shop floor. Utilising the SLAM algorithm solely left the robot out of position by 50-100 mm at times. By introducing ARTags and a vision system, these errors were reduced to 10 mm or less.

The concept of achieving a significant reduction in positional errors by more than 80% through the implementation of an integrated vision system has proven to yield substantial improvement for both existing and possible future mobile systems.

Several researchers have investigated the validation of the positional accuracy for different platforms. One research team proposed the use of an L-shaped approach to validate the accuracy of their mobile platform [100]. This was found to be too tailored to meet the specific expectations of the use case, without any translation to the KMR iiwa platform testing or quantification. Other groups have looked at testing their robots with circular paths and figures of eight [101], [102]. The results were determined by finding the displacement of the robot after these movements.

This work aims to adopt the suggestion of examining the overall displacement after the paths were completed. However, the paths tested by other researchers appeared unfeasible because of the size difference between the KMR and the robots used for these tests, and the effective experimental space limitations [100], [101], [102].

The present NDE environments utilising robotic manipulators are not collaborative in their methods, and still lack the essential technologies to accomplish fully autonomous NDE inspections without human intervention [103]. Currently, no research has presented the use of mobile manipulator platforms for NDE that possess complete autonomy to freely navigate and explore their surroundings.

To get baseline values required for a suitable mobile manipulator, the specifications of an in-house designed phased array ultrasound roller probe for robotic deployment are being

utilised [6]. For this roller probe, there is a fundamental requirement of a high degree of precision to achieve the expected results. From previous studies, experimental validation has deduced that using such sensors necessitates advanced control capabilities [6], [104]. Achieving optimal detection sensitivity in PAUT typically requires high precision, such as maintaining contact force within 0.5 N, positional accuracy better than 0.5 mm, and rotational accuracy within 0.1°. The minimum detectable defect size is governed by both the ultrasonic wavelength and the phased-array element pitch. For a 5 MHz wave in CFRP, the wavelength of approximately 0.58-0.6 mm would theoretically allow detection of sub-millimetre flaws. However, the 0.8 mm element pitch exceeds the $\lambda/2$ sampling criterion and therefore limits the achievable lateral resolution[105]. As a result, the inspection becomes pitch-dominated rather than wavelength-dominated, and the practical minimum detectable defect size is approximately equal to the pitch, around 0.8 mm. Therefore, a positional accuracy of 0.5 mm, lies well below both the wavelength and pitch limits and therefore does not constrain the inspection capability.

The specific defect size that must be detected, however, can vary depending on the sector. For the work presented here , the industrial partner does not require the detection of defects smaller than 6 mm in diameter. The need for such stringent performance metrics further highlights the role of robot metrology in ensuring that robotic systems meet the required tolerances for high-value applications [106]. Programs such as the National Institute of Standards and Technology (NIST) Measurement Science for Manufacturing Robotics (MSMR) initiative have also highlighted the critical importance of standardised testing

and performance benchmarks to enable greater deployment of autonomous robotic platforms in production environments[107].

The novelty and main contributions of this work are:

1. The development of an experimental procedure, which specifically focuses on testing the precision of mobile robotic platforms.
2. The evaluation of a mobile robotic platform for the potential use in high-accuracy PAUT applications.

The rest of the chapter is organised as follows: Section 3.2 describes the experimental design; Section 3.3 introduces the testing procedure. Section 3.4 provides results and a discussion of the work. Lastly, Section 3.5 concludes the work and discusses future work.

## 3.2. Experimental Design

Since there is no standard in place to establish and quantify the capabilities of mobile robots, this chapter proposes a novel strategy, inspired by the ISO 9283 [98], to examine various aspects of the mobile manipulator platform's capabilities. For the KMR that is utilised in this chapter, this includes:

a) Assessment of the mapping features,
b) Understanding the impact of different speeds on the positional accuracy of the KMR,
c) Testing the operational capabilities of the Mecanum omnidirectional wheels

The specification for the testing was to ensure that the different aspects and features of the mobile manipulator platforms were tested, including the behaviour of omnidirectional wheels.

The four mobile platform Mecanum wheels with three DoF enable unrestricted motion and orientation of the platform in two-dimensional (2D) space. Strafing movements can occur with the use of Mecanum wheels, in which the robot will move in any direction without changing its orientation. During strafing, the platform can complete translations in any direction, without doing a full rotation, offering great flexibility in confined environments.

Therefore, given that the KMR can translate to a preset position on the floor either using strafing or a combination of translation and rotation, one logical comparison point for this Mecanum omnidirectionally enabled platform is to compare strafing capabilities, Figure 3.2 a), versus full rotations, Figure 3.2 b). The KMR is also capable of driving with solely the encoders fitted onboard, without relying on the laser scanners for laser mapping. For this reason, a plan was devised to test the motions of the KMR during the strafing and rotations using its encoders as compared against the motions with mapping features enabled. This would clarify the benefits of utilising spatial localisation capabilities. For mobile platforms that lack holonomic capabilities, it is suggested that rotational tests will still yield adequate results concerning accuracy and repeatability capabilities.

The available testing environment was a 3-meter by 3-meter floorspace, to accommodate the size of the KUKA KMR platform within the temperature-controlled laboratory. The

floor was an SR1 Floor constructed [108] with epoxy resin, finished with Polyurethane Floor Paint. This means that the surface will not have a variation greater than 3mm when measured over a distance of 2 meters.

The final path design was constructed in the shape of a square with 1 $m^2$ in area to test the strafing and rotational capabilities. The path design is demonstrated in Figure 3.2 a), with target positions all spaced 1 m from each other. Moreover, the 4 m square test path provided a uniform distance between all target positions and functioned to ensure that the distance travelled accurately reflected the intended 1-meter target for each path. The rotational test followed the same structure as the strafing, shown in Figure 3.2 b). The rotation process is illustrated in Figure 3.2 c); however, the base rotates about the central axis of the platform, thereby maintaining a fixed position throughout the operation.

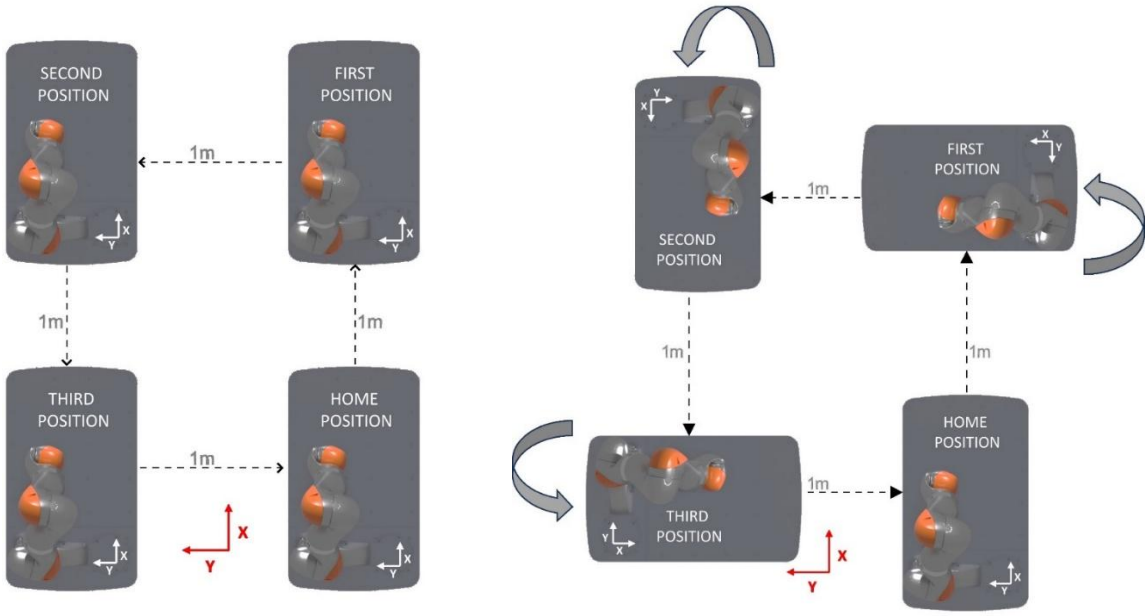

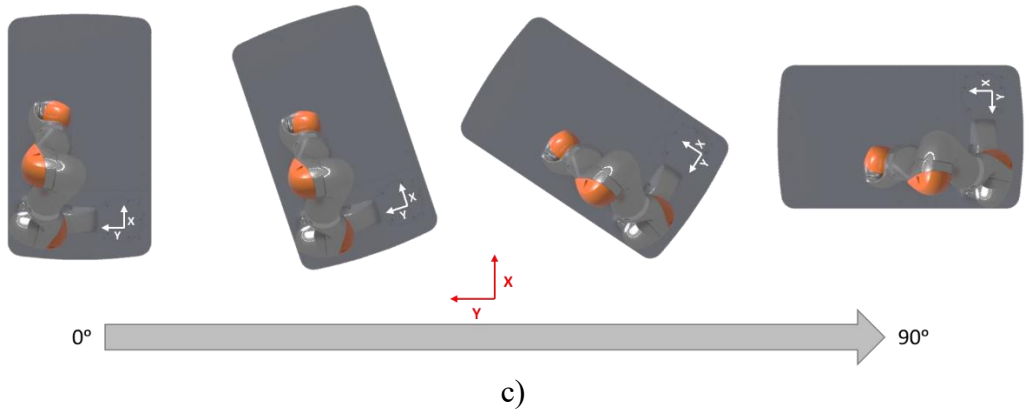


c)

*Figure 3.2. Planned Path Positions. a) Strafing, b) Rotational, c) Rotation Procedure (Global frame in red, KMR frame in white)*

### 3.2.1. Position Tracking

A Leica Absolute Laser Tracker AT901 [109] was used to track the performance and movements of the KMR with a 10 µm precision within a 160m$^3$ volume. Its three DoF capability ensured accurate tracking at different heights and angles. In strafing tests, the platform was always facing the same direction, meaning there were no concerns about the laser signal being disrupted, as demonstrated in Figure 3.2 a). However, the manipulator arm onboard interrupted the laser signal when the platform rotated more than 90 degrees, which required a rotation stage to be placed atop the manipulator, ensuring that its position would always be uninterrupted. This rotation stage was designed to be capable of remaining focused on one point and rotating accordingly in ±2π to always face a "true north". A Vicon T160 camera system [110] with a calibrated absolute error of 0.51mm [111] was used to determine its true north position and adjust the rotation stage orientation accordingly. The Vicon camera system is a 3D motion capture system with 12 cameras mounted surrounding a volume. In this method, infrared cameras were used to track

retroreflective markers. The KMR platform had these reflectors mounted on board, in several different positions, to allow for the Vicon system to detect and track them. A LattePanda minicomputer [112] was connected to a motor supporting the laser Red Ring Reflector 1.5" [113] mounted on top. A custom algorithm was developed to translate the platform's orientation data, obtained from the retroreflectors, into smooth rotational commands for the motor. This closed-loop system, illustrated in Figure 3.3, ensured that the reflector continuously faced the same direction, regardless of the robot's motion or orientation, allowing precise and consistent measurement of the KMR platform's position and heading.

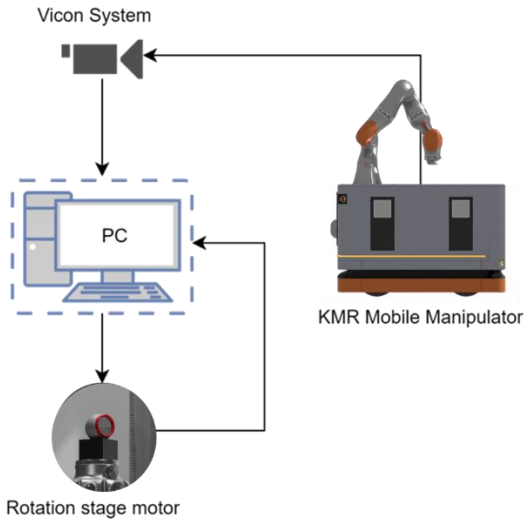


*Figure 3.3. Closed-loop rotation stage control*

The full system diagram is presented in Figure 3.4.

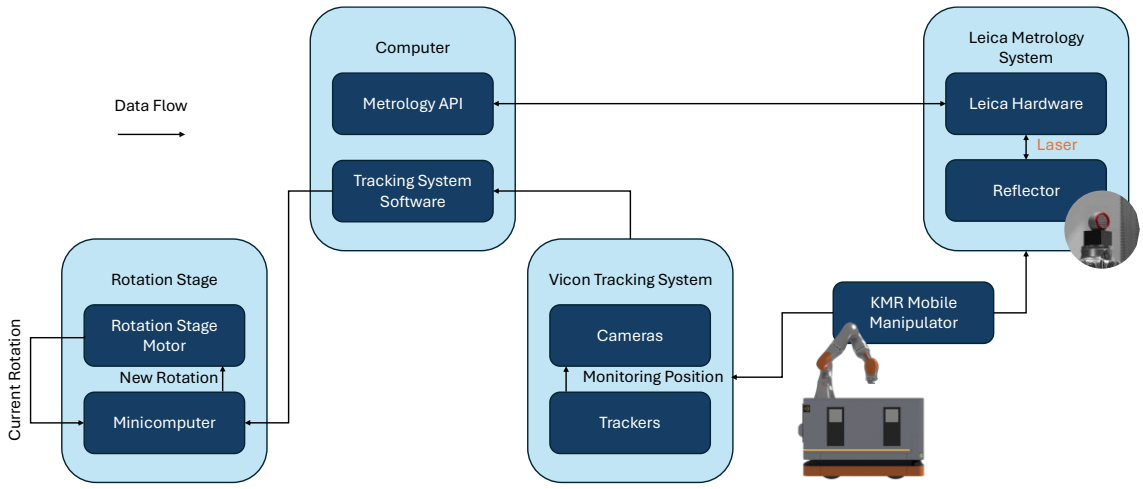


*Figure 3.4. Tracking System Architectural Diagram*

#### 3.2.1.1. Metrology validation

To validate the accuracy of the Leica laser tracker, the reflector was placed in a single position for an hour while the laser tracker recorded every 100 ms. A total of 37,651 entries were recorded, equating to just over 62 minutes of run time, for validation. This was done to verify the variation in the positional measurements. The results of this initial validation gave further confidence that the Leica could measure to a very high precision. The standard deviation was measured at 4.22 µm, 1.89 µm, and 5.21 µm for X, Y and Z components, respectively.

### 3.2.2. Controlled Features

The integrated SICK S300 laser sensors [114] onboard the KMR platform allowed the robot to localise and navigate. The onboard proprietary KUKA path planning algorithm used a variation of SLAM[115].

For laser mapping, there was a need to keep a constant consistent environment; any changes in the layout could impact the mobile manipulator platform's ability to localise. The SLAM utilisation for tracking and mapping in a dynamic environment has been explored previously [116], but its widespread adoption is still pending. This chapter only focuses on benchmarking the capabilities of the KMR platform; therefore, no third-party SLAM algorithms were explored or incorporated into the experiment. The experimental design plan was designed according to ASTM standard F3244-21 for AGV Navigation: Defined Area [117], in which individual tasks are repeated multiple times by the mobile platforms, within a designated floor space outlined by physical barriers. Rigid cardboard boundaries were used to surround the work area, providing a non-reflective solid planar barrier framework. The mapped view of the KMR is shown below in Figure 3.5.

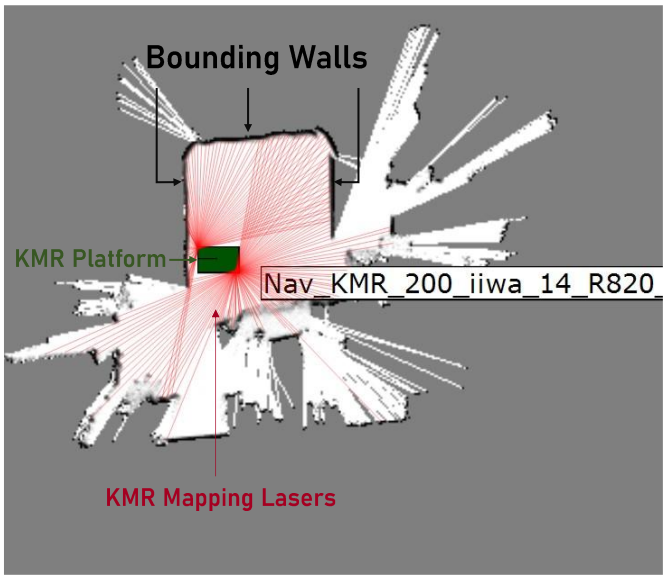


*Figure 3.5. KMR lasers identifying position in SLAM map.*

The complete working setup as described in this section is presented in Figure 3.6.

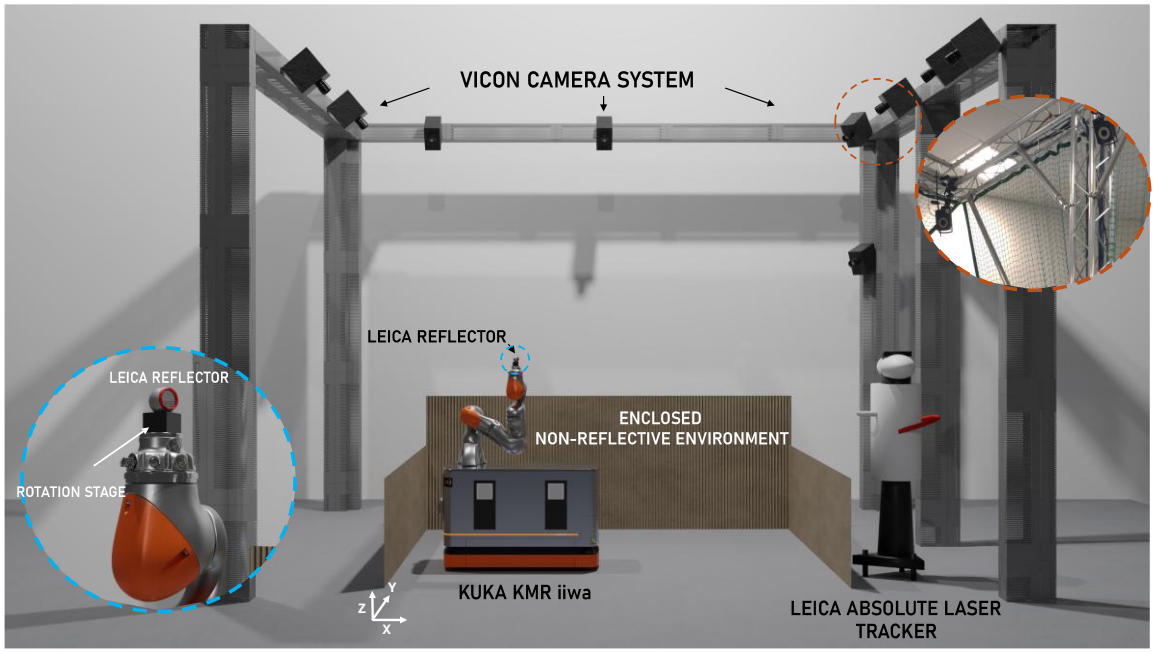


*Figure 3.6. Experimental setup for positional tracking of the KUKA KMR iiwa utilising a Leica laser tracker. (Co-ordinate frame represents the global frame for measurements)*

### 3.2.3. Teaching map and points

The KMR, with its lasers in mapping mode, was manually jogged in an enclosed space to teach the mobile platform the map. To enable the lasers to detect all the features and fluctuations of the surroundings, the KMR was operated slowly in several orientations. The quality of the map's representation of the environment was influenced by factors such as scanning speed, direction, and the number of passes over the area. Once the mapping process was complete, it was initiated through KUKA's software package, KUKA Sunrise OS [118], which enabled communication with the KMR. The generated map was then loaded onto the KMR, and the robot used it to verify its own localisation by navigating the environment. Once satisfied with its localisation, the platform signalled to Sunrise OS

that positioning in the environment was successful. Using Sunrise OS features, positions were taught utilising the platform's integrated laser sensors to map predetermined locations, starting with the home position. After determining the X and Y values of the home position, each additional position on the map was manually taught with its appropriate offset. The robot then drove to these locations, remapping at each to ensure accurate localisation. Both rotational and strafing tests followed this procedure, with the taught positions remaining constant across all tests and speeds.

## 3.3. Procedure

The testing method consisted of the two previously introduced path options, strafing, and rotations; each variation was tested ten times, with consecutive runs commencing from the previous stop, consistent with ASTM standard F3244-21 [117]. This provided additional information about a final displacement that could be compared to the average displacement between runs. The positional data was obtained from both the KMR and the AT901 tracking system. The ground truth Leica data were compared with the KMR positional data. Of the two path options, four further variations were tested.

- A strafing test using only the encoders,
- A strafing test utilising the mapping features,
- A rotation test using only the encoders,
- and finally, a rotation test using the mapping features.

Within these four variations, 3 different speeds were tested. Three speeds were chosen to validate whether there was any relation to the accuracy and repeatability of the platform with speed. The three speeds chosen for testing were, 0.08 m/s, 0.16 m/s and 0.24 m/s as

shown in Table 3.1. Odometry-only measurements were only needed at the lowest speed to establish a baseline, as real inspections would employ the higher precision of the SLAM navigation with odometry combined with absolute laser mapping.

*Table 3.1. Experimental Variations with speeds*

| | **Test Category** | | | |
|---|---|---|---|---|
| **Speeds (m/s)** | Strafing w/ Encoders | Strafing w/ Mapping | Rotations w/ Encoders | Rotations w/ Mapping |
| **0.08** | ✓ | ✓ | ✓ | ✓ |
| **0.16** | | ✓ | | ✓ |
| **0.24** | | ✓ | | ✓ |

The speeds of 0.08 m/s, 0.16 m/s, and 0.24 m/s were selected to evaluate the mobile platform's performance under safe and controlled conditions. The lowest speed, 0.08 m/s, reflects a realistic operational velocity for in-situ inspection tasks, where stability and measurement accuracy are critical. All chosen speeds ensured smooth motion without introducing excessive acceleration or vibration that could cause the platform to shake or reduce the integrity of data capture. Additionally, these speeds were within the tracking capabilities of the onboard laser system, avoiding disruptions or safety-related interruptions due to loss of signal or forced emergency stops.

In the absence of a standard for evaluating the accuracy and repeatability of a mobile platform, a guideline was established with proposed definitions:

- **Repeatability**: The ability of the system to return to its original starting position.
- **Repeatability displacement error**: The distance between the system's returned position and its original starting position.
- **Repeatability displacement accuracy**: The difference between the ground truth position (measured by the Absolute tracker) and the position reported by the KMR.

## 3.4. Results and Discussion

The results are presented in 4 graphs. The graphs of Figure 3.7 and Figure 3.8 display the repeatability error of the mobile platform across each of the runs. For the strafing and rotational tests. The graphs of Figure 3.9 and Figure 3.10 show the displacement error of the platform across each of the runs. This allowed for more insight into the platform's performance. The graphical data is also summarised into 4 tables, with the mean and standard deviations of the data.

### 3.4.1. Repeatability Error

The repeatability errors presented in this section are the difference in values reported between the measured ground truth, from the AT901 tracking system, and the reported value by the KMR platform.

The results from the strafing repeatability tests, presented in Figure 3.7, demonstrate the repeatability errors across each test run. The most notable observation is that the encoder error was consistently larger than the mapping errors by a significant margin. For all test

runs, the differences between the mapping and encoder errors remained above 15 mm, highlighting a substantial performance gap. Furthermore, a trend of decreasing error was observed as the number of runs increased for the encoder tests, suggesting an improvement in the KMR's reporting accuracy over time.

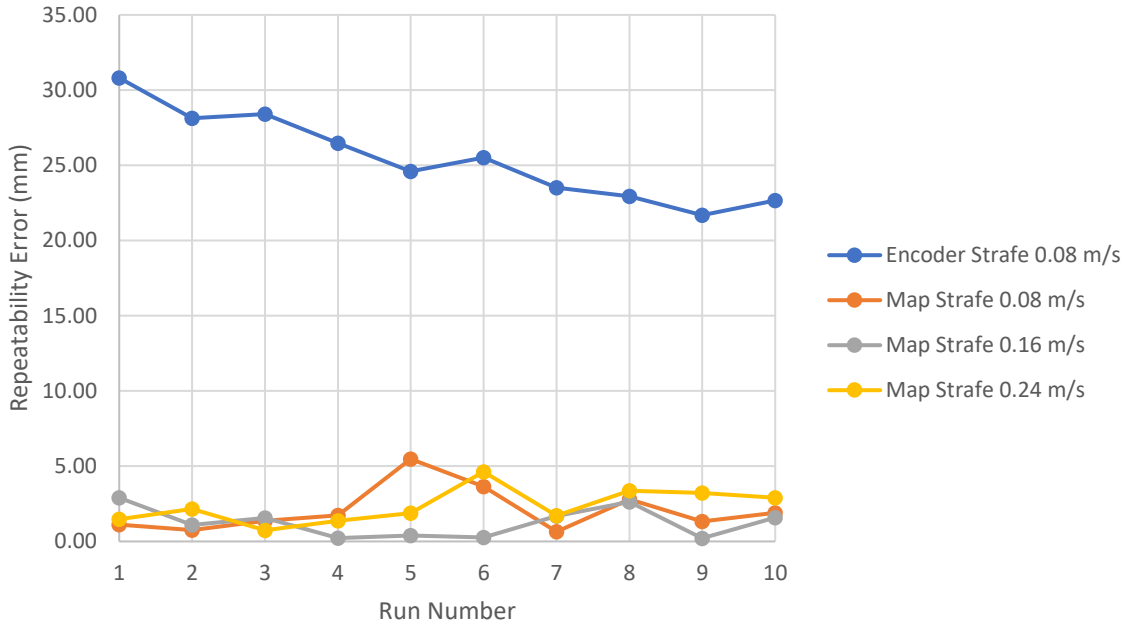


*Figure 3.7. Strafing repeatability errors*

Enabling the mapping features resulted in a noticeable reduction in error, with no mapped run exceeding a 6 mm error in the strafing tests, as shown in Figure 3.7. The errors were more random in nature compared to those observed in the encoder tests, and no evident pattern emerged when mapping was enabled. Additionally, variations in speed had minimal impact on the error results, as reflected by the mean and standard deviation values in Table 3.2.

*Table 3.2. Tabulated Strafing Repeatability Errors*

| **Repeatability Error** Strafing **Tests (mm)** | | | | |
|---|---|---|---|---|
| Runs | Encoder 0.08 m/s | Map 0.08 m/s | Map 0.16 m/s | Map 0.24 m/s |
| 1 | 30.81 | 1.12 | 2.90 | 1.48 |
| 2 | 28.13 | 0.76 | 1.10 | 2.16 |
| 3 | 28.42 | 1.36 | 1.56 | 0.74 |
| 4 | 26.48 | 1.73 | 0.23 | 1.38 |
| 5 | 24.61 | 5.48 | 0.39 | 1.89 |
| 6 | 25.52 | 3.64 | 0.26 | 4.63 |
| 7 | 23.52 | 0.65 | 1.68 | 1.71 |
| 8 | 22.93 | 2.79 | 2.63 | 3.37 |
| 9 | 21.69 | 1.32 | 0.21 | 3.22 |
| 10 | 22.66 | 1.90 | 1.58 | 2.90 |
| **Mean** | **25.48** | **2.08** | **1.26** | **2.35** |
| **SD** | **2.80** | **1.43** | **0.94** | **1.11** |

The largest standard deviation was recorded at 0.08 m/s (1.43 mm), followed by 0.24 m/s (1.11 mm) and 0.16 m/s (0.94 mm). The mean errors also aligned with this pattern, with the 0.16 m/s test yielding the smallest mean error of 1.26 mm, followed by 0.08 m/s (2.08 mm) and 0.24 m/s (2.35 mm). These improvements were substantial, particularly in comparison to the encoder test, which had a mean error of 25.48 mm and a standard deviation of 2.08, representing an improvement of over 90.8% following the activation of mapping features.

The introduction of rotational paths added a new layer of complexity, leading to different results. As seen in Figure 3.8, the repeatability errors for the rotational tests showed a less clear trend than those observed in the strafing tests.

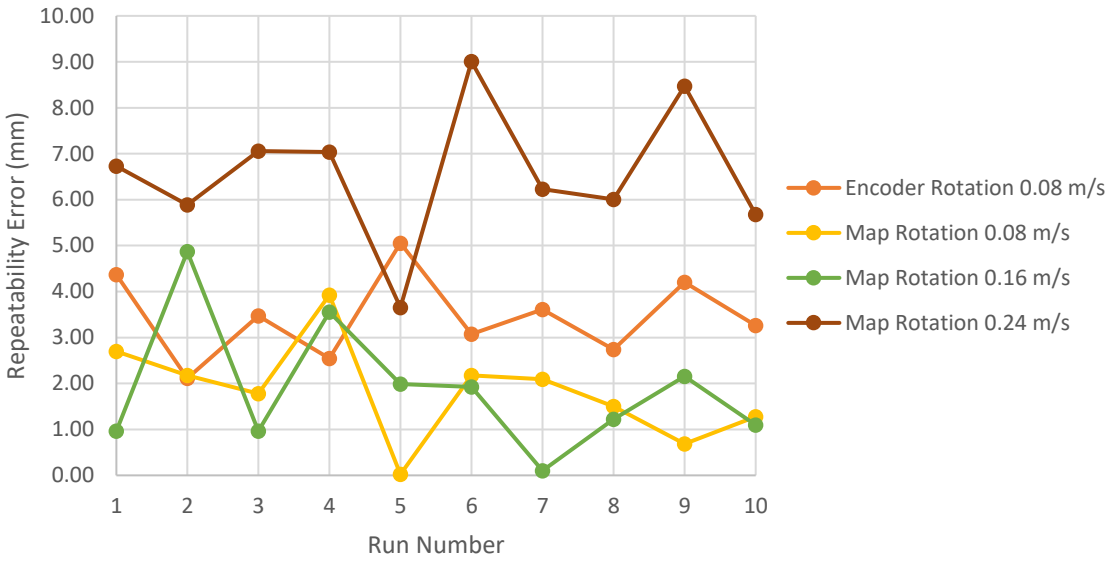


*Figure 3.8. Rotational repeatability errors*

Notably, the encoder errors were not the worst performers in this scenario. Shown in Table 3.3, the 0.24 m/s speed for the mapping test showed a mean error of 6.58 mm, which was larger than the errors for the other mapped tests (1.83 mm and 1.88 mm).

*Table 3.3. Tabulated Rotational Repeatability Errors*

| **Repeatability Error** Rotational **Tests (mm)** | | | | |
|---|---|---|---|---|
| Runs | Encoder 0.08 m/s | Map 0.08 m/s | Map 0.16 m/s | Map 0.24 m/s |
| 1 | 4.37 | 2.70 | 0.96 | 6.73 |
| 2 | 2.11 | 2.18 | 4.87 | 5.88 |
| 3 | 3.47 | 1.78 | 0.96 | 7.06 |
| 4 | 2.55 | 3.93 | 3.55 | 7.03 |
| 5 | 5.06 | 0.02 | 1.98 | 3.65 |
| 6 | 3.07 | 2.18 | 1.92 | 9.01 |
| 7 | 3.61 | 2.09 | 0.10 | 6.23 |
| 8 | 2.74 | 1.50 | 1.22 | 6.01 |
| 9 | 4.20 | 0.69 | 2.16 | 8.47 |
| 10 | 3.26 | 1.28 | 1.10 | 5.68 |
| **Mean** | **3.44** | **1.83** | **1.88** | **6.58** |
| **SD** | **0.85** | **1.02** | **1.33** | **1.42** |

A noticeable difference between the 0.24 m/s test and the lower speeds suggests that the complexity of the path has a threshold beyond which errors increase. In the rotational tests, enabling mapping resulted in a 45.3% reduction in error at the lower speeds but an increase of 90.9% at 0.24 m/s.

### 3.4.2. Displacement Error

To gain further insights into the platform's performance, displacement errors were also evaluated. Displacement error was defined as the difference between the current starting position and the initial position at the beginning of each experiment. The reference point remained consistent when comparing different runs, allowing for a direct comparison of displacement performance across test cycles.

In contrast to the downward trend in repeatability error observed in the encoder test in Figure 3.7, the displacement errors showed an upward trend as the runs progressed, as presented in Figure 3.9.

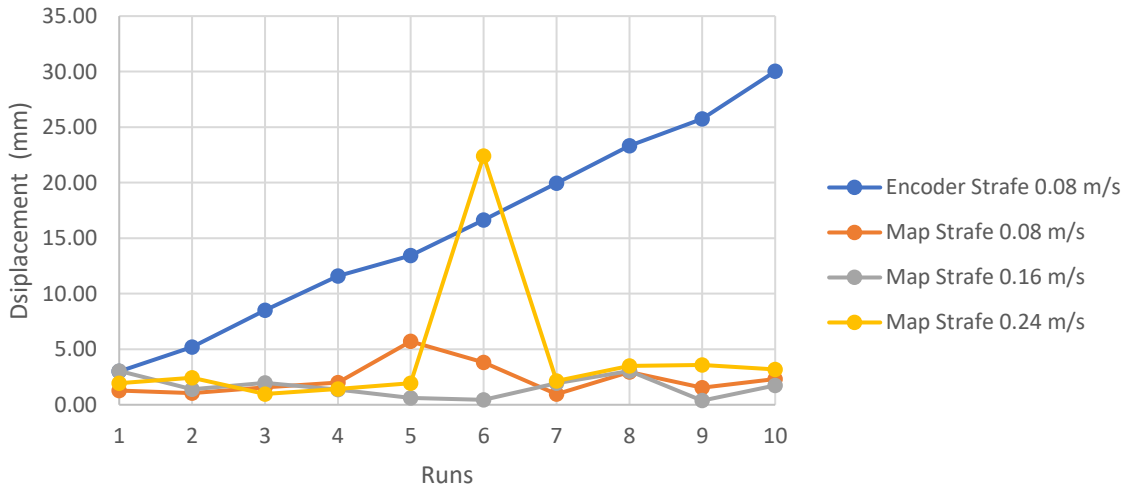


*Figure 3.9. Strafing displacement errors*

This suggests that while encoder performance improved in terms of error reporting, the platform's actual position continued to drift off-target over successive runs. With the activation of mapping features, the trends in displacement error were similar to those in

the repeatability errors. The 0.16 m/s test again demonstrated the best performance, with the smallest mean displacement error (1.59 mm) and standard deviation (0.91 mm), presented in Table 3.4. The 0.08 m/s test showed a mean displacement error of 2.32 mm and a standard deviation of 1.41 mm, values that were comparable to those observed in the strafing tests. The encoder test, as seen in Figure 3.9, indicated that the error compounded with each run; therefore, the mean and SD were not calculated, as this analysis was not deemed appropriate.

*Table 3.4. Tabulated Strafing Displacement Errors*

| **Displacement Error** Strafing **Tests (mm)** | | | | |
|---|---|---|---|---|
| Runs | Encoder 0.08 m/s | Map 0.08 m/s | Map 0.16 m/s | Map 0.24 m/s |
| 1 | 3.00 | 1.28 | 3.05 | 1.94 |
| 2 | 5.19 | 1.05 | 1.39 | 2.44 |
| 3 | 8.51 | 1.57 | 1.96 | 0.97 |
| 4 | 11.60 | 1.99 | 1.37 | 1.42 |
| 5 | 13.45 | 5.70 | 0.62 | 1.94 |
| 6 | 16.63 | 3.82 | 0.44 | 22.41 |
| 7 | 19.95 | 0.95 | 1.94 | 2.14 |
| 8 | 23.34 | 2.96 | 3.04 | 3.51 |
| 9 | 25.75 | 1.54 | 0.37 | 3.60 |
| 10 | 30.03 | 2.32 | 1.73 | 3.17 |
| **Mean** | **-** | **2.32** | **1.59** | **4.35** |
| **SD** | **-** | **1.41** | **0.91** | **6.07** |

However, the 0.24 m/s test exhibited an outlier, with a displacement error of 22.41 mm recorded in one run. Interestingly, this outlier was followed by a significantly reduced error of 2.14 mm in the subsequent run. This anomaly may suggest that the KMR did not report its position as accurately during that specific run, although overall reporting improved relative to the encoder-based tests. By the 7th run, the platform was able to return to its target position within a margin of < 3 mm, indicating that the system is capable of recovering from such outliers. Excluding this outlier, the mean displacement error for the 0.24 m/s test would have been 2.35 mm, with a standard deviation of 0.86, aligning more closely with the other mapped tests.

Similar trends were observed in the rotational tests, where a nearly linear increase in displacement error was evident for encoder-based tests, shown in Figure 3.10.

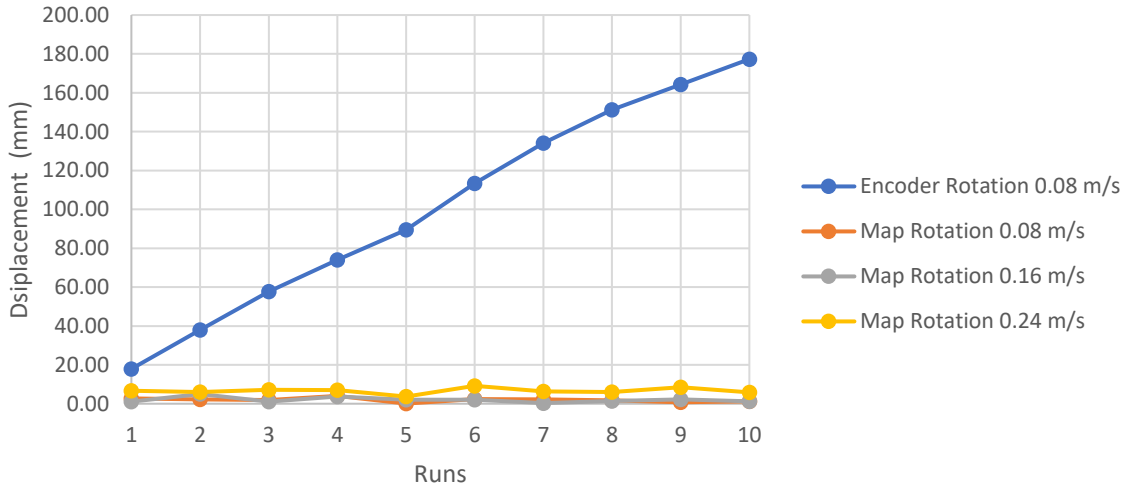


*Figure 3.10. Rotational displacement errors*

The displacement errors for the rotational tests were considerably larger than those observed in the strafing tests. The tabulated results, Table 3.5, showed the initial

displacement error for strafing was 3.00 mm, whereas for the rotational tests, it was 17.91 mm. The final displacement errors for strafing and rotational tests were 30.03 mm and 177.31 mm, respectively. Although the repeatability errors for rotational tests remained under 3.5 mm, the displacement errors were significant, suggesting that encoder-based systems may not be suitable for applications requiring high precision, especially in complex movements. As in Table 3.4, the mean and standard deviation were not calculated for the encoder tests due to the compounded error.

*Table 3.5. Tabulated Rotational Displacement Errors*

| **Displacement Error** Rotational **Tests (mm)** | | | | |
|---|---|---|---|---|
| Runs | Encoder 0.08 m/s | Map 0.08 m/s | Map 0.16 m/s | Map 0.24 m/s |
| 1 | 17.91 | 2.79 | 1.03 | 6.75 |
| 2 | 38.00 | 2.24 | 4.97 | 5.98 |
| 3 | 57.66 | 1.87 | 1.04 | 7.16 |
| 4 | 73.96 | 4.02 | 3.73 | 7.07 |
| 5 | 89.49 | 0.07 | 2.12 | 3.68 |
| 6 | 113.31 | 2.37 | 1.99 | 9.19 |
| 7 | 134.13 | 2.23 | 0.33 | 6.33 |
| 8 | 151.22 | 1.68 | 1.35 | 6.02 |
| 9 | 164.26 | 0.77 | 2.24 | 8.53 |
| 10 | 177.31 | 1.31 | 1.17 | 5.83 |
| **Mean** | **-** | **1.93** | **2.00** | **6.65** |
| **SD** | **-** | **1.04** | **1.33** | **1.44** |

Mapping-enabled tests showed considerable improvement in both repeatability and displacement errors, with the 0.08 m/s and 0.16 m/s tests yielding mean displacement errors of 1.93 mm and 2.00 mm, respectively. However, for the fastest speed of 0.24 m/s, the mean displacement error increased to 6.65 mm, with a standard deviation of 1.44 mm.

For rotational movements, lower speeds (up to 0.16 m/s) demonstrated the best performance, yielding repeatability and displacement errors below 2 mm. In contrast, using encoders alone for complex movements, while offering repeatability, resulted in large displacement errors, which would not be acceptable for scenarios demanding high accuracy.

## 3.5. Conclusion

The desire to explore greater flexibility in the high-value manufacturing industry by introducing mobile manipulators is a promising opportunity. For a successful introduction of such technologies, procedures, and knowledge must be in place to understand the capabilities and limitations of these mobile manipulator platforms.

To address this gap, a novel experimental procedure was presented in this chapter to quantify and understand the limitations and capabilities of the KUKA KMR iiwa. This was done by assessing the use of the mapping features, understanding the impact of different speeds on the positional accuracy of the KMR and testing the operational capabilities of the Mecanum omnidirectional wheels.

The KUKA KMR iiwa mobile manipulator is quoted to achieve positioning accuracies of up to ±5 mm [54]. However, the results of this work demonstrate that the actual accuracy falls short of the stated values. Notably, it appears that the KMR tends to underestimate its error when using its encoders only compared to the AT901 readings. When using mapping features and laser data, the KMR then overestimates its performance.

The results of the strafing and rotational path tests demonstrated that enabling mapping features significantly enhanced the KMR's performance, particularly in terms of repeatability and displacement errors. While encoder-based systems showed consistent repeatability errors, they were prone to increasing displacement errors over successive runs, suggesting that, although reporting accuracy improved, the platform's actual position drifted over time. In contrast, the mapping features substantially reduced both repeatability and displacement errors, with the greatest improvements observed at lower speeds (0.08 m/s and 0.16 m/s).

Mapping's impact on rotational paths was more nuanced. While the 0.24 m/s test in rotational movements showed increased displacement errors, the overall trend indicated that lower speeds yielded more accurate performance, with displacement and repeatability errors remaining under 2 mm. These results highlighted the importance of speed and path complexity in optimising performance. Encoder-based systems, while capable of repeatable movements, were found to be unsuitable for high-precision applications due to significant displacement errors, especially in more complex rotational movements.

Overall, the integration of mapping features provided a substantial improvement over purely encoder-based systems, marking a significant advancement for applications requiring precise and repeatable positioning—an improvement expected to generalise across other mobile platforms. However, careful consideration of speed and path complexity will be essential to maximise performance, particularly in scenarios demanding high accuracy.

The required accuracy for precise PAUT inspections is 0.5 mm; the onboard manipulator, KUKA LBR iiwa, has been previously investigated and proven to have a repeatability of <0.1 mm [51]. While such precision supports high-sensitivity PAUT applications, it's important to note that accuracy requirements can vary by industry. In this case, the industrial partner requires the detection of defects no smaller than 6 mm in diameter.

With the results presented here, the system could be suitable for certain PAUT tasks involving the detection of larger defects or cracks. However, for PAUT applications demanding higher precision, external metrology assistance would likely be necessary. These findings, while focused on PAUT due to its strict accuracy demands, highlight the broader applicability of mobile manipulation platforms across manufacturing. The demonstrated precision enables potential deployment in handling tasks, such as those found in pharmaceutical [82] and pick-and-place applications, where less stringent requirements can be offset by sensing systems.

In future work, there would be interest in continuing and expanding investigations by evaluating how the integration of additional odometric sensing features and external

references could improve the real-time precision necessary for the KMR platform. Since this work was limited to laboratory space, further studies may also involve testing within larger and more complex environments, which could yield slightly different outcomes and provide results that are more representative of real-world conditions. Moreover, subsequent projects could focus on analysing and characterising the errors associated with moving to a designated position before operating the robotic arm, enabling a deeper understanding of the combined error sources inherent in mobile manipulation.

# Chapter 4

# Intelligent Operator-Independent Flexibility in Robotic Non-Destructive Evaluation

## 4.1. Introduction

In the field of NDE, fixed automated robotic systems are widely used for inspection tasks, particularly in aerospace applications. As discussed in the Chapter 2: Commercial systems, solutions like TWI IntACOM and Tecnatom TAURUS utilise dual industrial robots and water jet–coupled UT to achieve precise and repeatable measurements. These systems, while effective, are constrained by high costs, large footprints, and limited flexibility when inspecting components of varying geometries.

Mineo et al. [119] proposed a dual-robot setup using CAD-based path planning, similar to the IntACOM system. Although this configuration enabled faster inspections compared to immersion tank scanning, it still relied heavily on prior knowledge of the component geometry, which limits adaptability, a challenge noted in the *Limitations and Gaps in Existing Research* section.

Further examples, such as the inspection of composite wing panels using tracked manipulators [92], align with systems like ACCUBOT, which offer high precision but require predefined paths and fixed installations. These setups demand extensive preparation and custom-designed inspection cells, reducing their suitability for dynamic or reconfigurable environments.

As highlighted in Chapter 2 Section 2.3, fixed robotic setups often require components to be placed in exact positions within inspection cells. This restricts adaptability to unexpected obstacles or geometric deviations and makes offline path planning less effective in variable conditions.

To address these limitations, Cobots have emerged as a promising alternative. As described in the Section 2.2 of Chapter 2, Cobots offer enhanced safety, reduced spatial requirements, and the ability to operate alongside humans without the need for enclosures. They are also a major aspect of the Industry 5.0 transformation, that emphasises human-centric industrial systems [120]. Although still in its early stages, there is a growing interest in transitioning towards more collaborative working environments. The use of Cobots makes them suitable for shared work environments, as they achieve results comparable to/exceeding traditional fixed setups while enabling humans and robots to work together safely, thereby reducing the need for separate enclosures or cells for fully autonomous systems [121]. This flexibility is exemplified by concepts like the Evident WBIS system, which proposes mobile collaborative inspection without relying on CAD-based programming.

Chapter 2's *Limitations and Gaps in Existing Research* section underscores the need for fully automated, mobile manipulator systems that do not depend on prior component knowledge. The previous chapter explored the usability of the platform for NDE inspections by quantifying and understanding the limitations and capabilities of mobile manipulators. The concluding remarks indicated that combining additional precision systems to improve the inspection ability with mobility would be beneficial, and this chapter builds upon that work by investigating flexible, operator-independent inspection methods that enhance adaptability and reduce setup complexity.

Given the highlighted shortcomings of the fixed manipulator setups, this chapter introduces a novel adaptable scanning system for robotic NDE, integrating (i) a collaborative robot, (ii) 3D vision for component identification, (iii) a custom automated path planning approach for inspection, and (iv) simultaneous force-position control, delivering the PAUT sensor with precision comparable to fixed robotic systems. The benefit of this system is the reduced requirement for any prior knowledge about the pose or geometry of the inspected sample, contrary to the approach used in the previously covered literature[119]. The main contributions of this chapter are:

1. The development of a flexible robotic PAUT scanning setup which reduces the need for prior part knowledge and part-specific hard-coded information.
2. Integration of a collaborative robotic arm, PAUT sensor for inspection, and a 3D vision system for automated path planning through component identification
3. Testing of the proposed system on a range of composite and metal samples, both with flat and curved surface profiles to scrutinise the systems flexibility

The rest of the chapter is organised as follows: Section 4.2 outlines the materials and methods used, and Section 4.3 introduces the samples inspected. Section 4.4 presents the results, followed by the discussion of the work in Section 4.5. Lastly, Section 4.6 concludes the chapter and outlines future work.

## 4.2. Materials and Methods

### 4.2.1. Experimental Design Procedure

This chapter aims to develop a methodology for the automated and flexible inspection of high value manufacturing components such as the ones of the aerospace industry.

The constructed geometries of the safety-critical primary aircraft structures are often challenging to inspect. These structures are commonly manufactured using materials such as CFRP or metallic alloys, including Aluminium 2024, which is valued for its high strength-to-weight ratio and excellent tensile strength [122].

These materials are chosen for their durability, manufacturability, and ability to withstand the demanding conditions encountered during flight, ensuring the reliability and safety of key structural components. Despite these advantages, such components introduce inspection challenges due to their complex shapes and material properties.

Therefore, this chapter examines the performance of the proposed system on both CFRP and metallic samples. Removing the need for precisely calibrated setups for the inspection of components is one of the main aims of the work presented in this chapter , as it would allow for increased flexibility.  This approach aims to reduce costs and material usage in

industry associated with the construction of precise jigs and fixtures, and to support the automation within high-mix, low-volume production settings.

Component identification and localisation was achieved using a Zivid One+ M 3D camera [123]. The camera employed structured light 3D technology to capture detailed representations of the environment. Structured light 3D technology captures the shape of objects by projecting a series of light patterns (usually grids or stripes) onto the surface and analyses the deformation of these patterns. The distortions in the light patterns are then used to calculate the object's 3D geometry with high precision [124]. The camera spatial resolution across varying working distances is presented in Appendix A – Camera Spatial Resolution [123]. Following the vision system setup, the KUKA LBR iiwa was utilised for its human collaborative nature and the integrated torque sensors that allow for a safe and controlled environment [125]. The LBR iiwa features 7 degrees of freedom, has a reach of 820 mm, a maximum payload capacity of 14 kg, and offers a repeatability of ± 0.1 mm. Finally, the ultrasonic setup completed the overall design procedure, with details provided in Section 4.2.3.

### 4.2.2. Overall System

The full system is broken down into 3 main parts; the full system block diagram is displayed in Figure 4.1. The robotic, ultrasonic setup and computer. The 3D camera and robotics feature as part of the robotic section and interact directly with the personal computer (PC) for the custom developed algorithms required for the inspection.

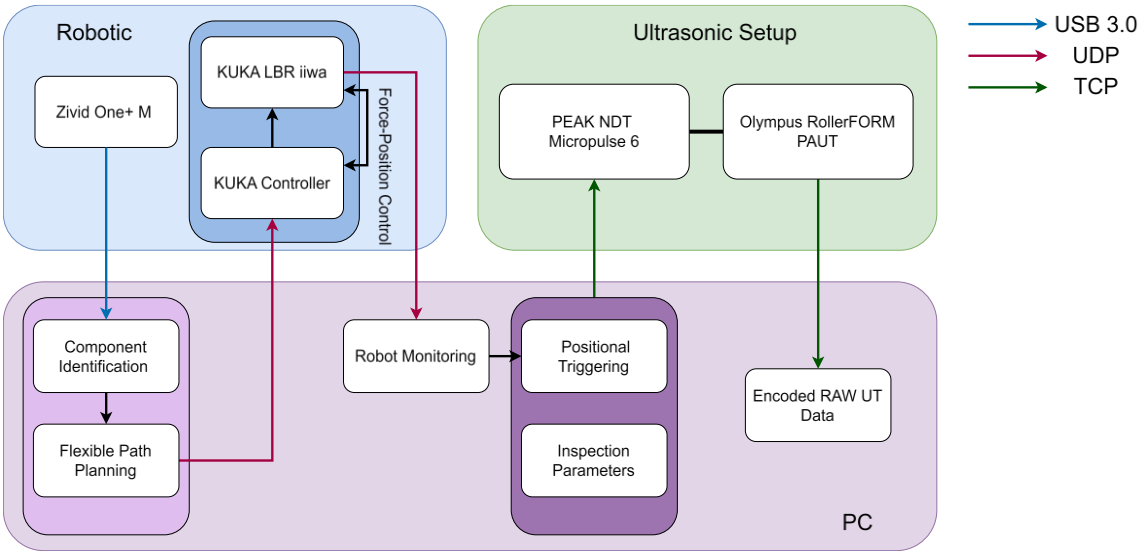


*Figure 4.1. Full System block diagram*

The full system modules, shown in Figure 4.1, are broken down further and explained in Sections 4.2.3 - 4.2.7.

### 4.2.3. Ultrasonic Setup

The ultrasonic setup used utilises an Olympus RollerFORM wheel probe, housing a 64-element linear phased array [126], interfacing with a Peak NDT Ltd. MicroPulse 6 array controller [127]. The phased array probe had a centre frequency of 5 MHz, with an element pitch of 0.8 mm and elevation of 6.4 mm. The ultrasonic controller communicated customised focal laws to the array and received raw ultrasonic data, which was then transmitted to a desktop PC via an Ethernet internet protocol suite, TCP/IP, connection.

For the inspection of the samples, the parameters used have been summarised and presented in Table 4.1.

*Table 4.1. Ultrasonic parameters for sample inspections*

| Material | Scanning Mode | Voltage | Sub-Aperture | Pulse Width | Gain | TVG | Acquisition Rate |
|---|---|---|---|---|---|---|---|
| **Composites** | Linear | 80 V | 4 Elements | 150 ns | 22.5 dB | 1.25 dB/mm | 100 MHz |
| **Metal** | Linear | 80 V | 4 Elements | 150 ns | 40 dB | 0 dB/mm | 100 MHz |

The raw data was stored with 32-bit precision. For the inspection of the metal sample, the setup remained largely the same, with the main difference being a higher fixed gain setting of 40 dB.

The calibration process for the two samples material was performed by adjusting the receiver gain. As the inspection was carried out using 0° linear scans, the beam propagated vertically through the material rather than at an angle. This configuration allowed the backwall to act as a consistent reference reflector, with the gain adjusted until the received signal reached 80% of full-screen height [128].

Unlike metals, which are homogeneous and isotropic, composite materials such as CFRPs are made up of layers of carbon fibre plies impregnated by resin as matrix. These materials are inherently non-uniform and anisotropic, with regions that can be carbon-rich or resin-rich and composed of layers with directional properties. Each of the resin/carbon-rich regions has distinct acoustic impedances, and these variations in acoustic impedance between the carbon and resin-rich areas leads to reflections and scattering of ultrasonic energy at each interface. As the ultrasound wave travels deeper into the material, these impedance mismatches cause progressive loss of signal strength, distortion of the wavefront, and the generation of backscatter noise, all of which reduce the sensitivity to smaller features/defects in the ultrasonic image.

As a result, the signal experiences high attenuation in composites, particularly in resin-rich zones where energy is absorbed more readily. This makes it extremely challenging to maintain a high signal-to-noise ratio (SNR), especially for deeper defects, or flaws located near layered impedance transitions.

Time-Varied Gain (TVG) was used to counteract the loss in signal amplitudes by applying a gain that varies with time, and therefore with depth of penetration, as the ultrasonic pulse travels through the material. TVG is a beneficial technique in ultrasonic testing that compensates for amplitude loss over distance, improving signal strength across varying depths within materials, particularly used in conjunction with inspection of anisotropic and attenuative materials. TVG was set to 1.25 dB/mm to account for attenuative effects of CFRP, allowing for matching the amplitudes from the front and back wall. This linear increase in gain started after the surface echo.

In contrast, the more uniform properties of polycrystalline metallic materials allow ultrasound waves to propagate with relatively lower scattering or absorption as compared to CFRPs. As a result, the signal degradation is less severe, particularly for thin components so the metal sample did not require any TVG.

The inspection of aerostructures is governed by strict regulations and standards. For this reason, inspections are carried out using PAUT, as they allow for beam steering and offer greater durability due to its use of multiple elements. In the event one element fails, the system can continue to operate, unlike a single element-based system. This was therefore the reasoning for the use of a PAUT probe. The choice of the described phased array probe

was based on the inclusion of a PAUT probe within the system and its unique roller-type construction, which made it suitable for robotic deployment.

The probe features a linear UT array centred within a cylindrical roller probe structure which was composed of soft tire as the outer shell and filled with a coupling liquid. This design allows the assembly to roll over the surface of the sample while the ultrasonic array remains stationary and protected in centre. The roller probe is shown in Figure 4.2, where the cross-sectional view of Figure 4.2 a) highlights the internals, and Figure 4.2 b) presents the assembled probe.

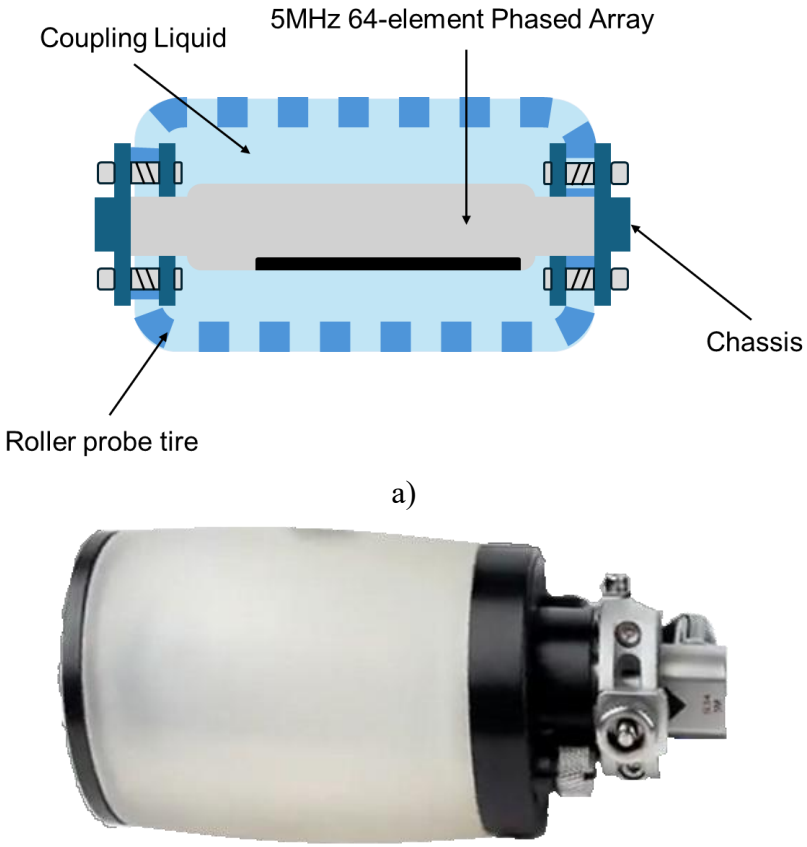


*Figure 4.2. PAUT roller probe, a) Cross-sectional view, b) Assembled Probe*

Although an excellent fit for automation purposes, this setup presents three challenges. First, a coupling medium is required between the roller probe and the inspected sample—in this case, a thin layer of sprayed water. Second, even very slight variations of surface profile/quality will affect the contact quality, and hence the intensity of the UT beam energy transferred into the sample; therefore, the need for constant coupling force applied by the robot to achieve a consistent coupling quality. Third, for optimal ultrasonic inspection and to produce high-quality scans the array must remain perpendicular to the inspection surface, which ensures that the beam is normal to the front and backwall, requiring fine real-time adaptive control over the robot's end effector pose.

The end-effector frame of the robot, along with the forces acting upon it, are presented in Figure 4.3 to more clearly illustrate the reference frames and their influence during the inspection process. Both the probe and the vision system were mounted to the robot end-effector via a custom mount – further detailed in Appendix C – CAD for Experimental , Section C-2.3. Probe and Camera Mount.

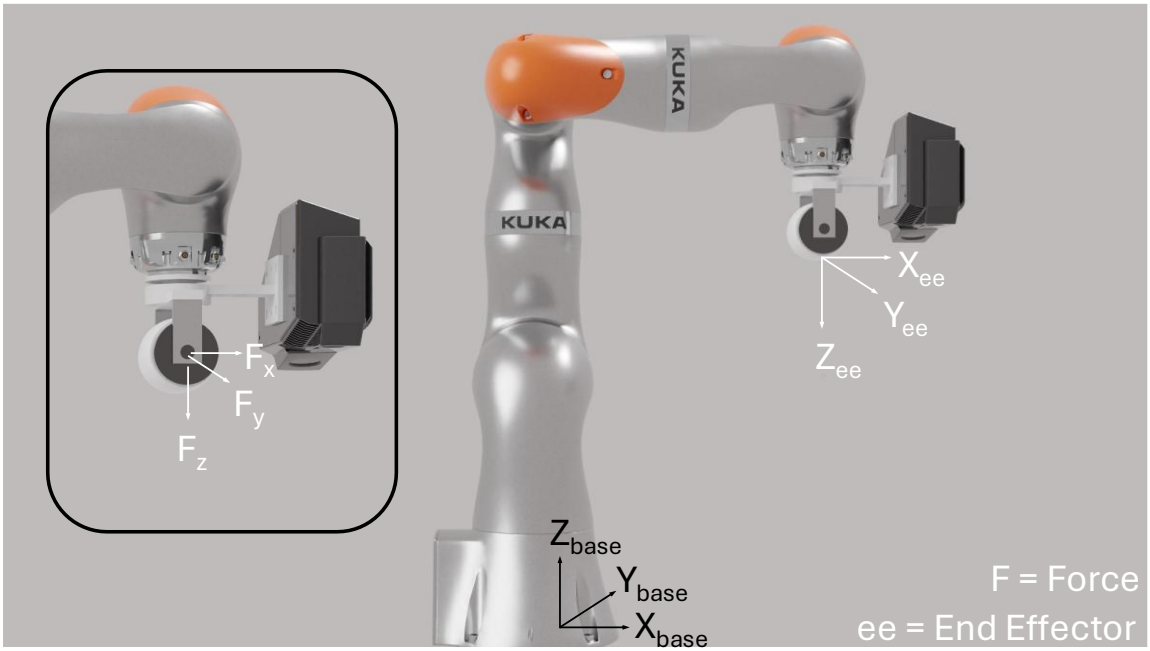


*Figure 4.3. Robotic and end effector frames, with force experienced frame*

While the vertical movement of the array is controlled by estimating the end-effector forces, set to achieve a predetermined contact force, maintaining proper angular alignment of the array to stay normal to the inspection surface is more challenging due to potential rotational misalignments in the Roll and Pitch axes/directions. These are shown in Figure 4.4 a).

A misalignment in the roll would position the array length slightly tilted with respect to the surface which results in inconsistent time-of-flight readings from the front wall and the back wall, due to the varying lengths of the ultrasonic paths for individual array elements. Similarly, a misalignment along the pitch would lead to ultrasonic waves interacting with the material at an angle, causing part of the excited wave energy to be lost as the beam refracts at the interface of the probe/material and fails to return to the array. This would result in poor scan quality with a lower SNR. Misalignment in the pitch is

shown in Figure 4.4 b), for the case with "probe's incorrect pose", showing an exaggerated case of ultrasonic beam propagation direction imposed by errors in probe's pitch deviating from the surface normal.

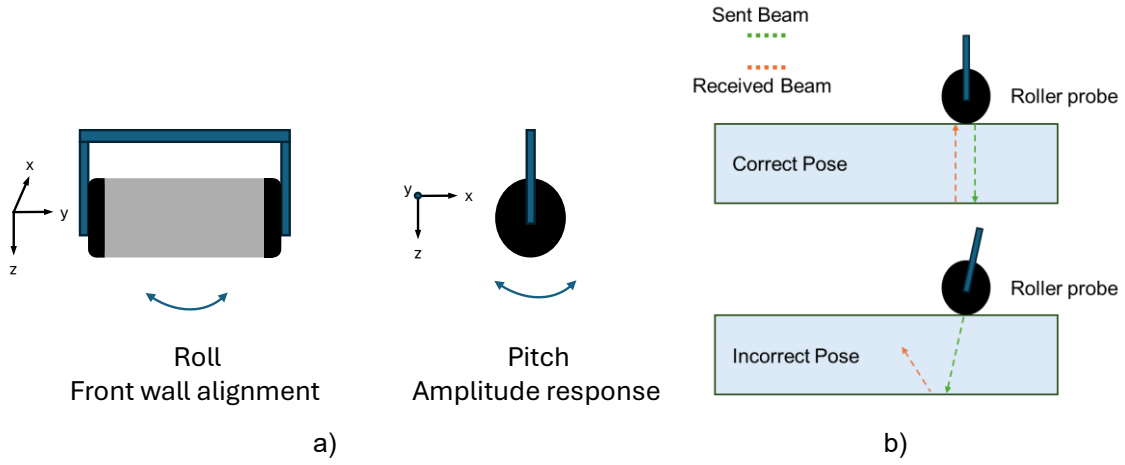


*Figure 4.4. Roller probe manipulation effect on ultrasonic signal, a) Roll and Pitch, b) Pitch misalignment*

The captured ultrasonic data was stored in a three-dimensional array structure (Scan index, Time samples, Probe sub-aperture), then normalised with respect to the largest amplitude, and the time samples (A-scans) were enveloped using a Hilbert transform [129] to extract the instantaneous amplitude response of the signal.

For the remainder of this chapter, the data will be represented either as a B-scan (a cross-sectional view of the inspected sample) derived from the normalised data, or as an amplitude C-scan (a top-down view of the inspected sample, representing the maximum occurring amplitudes within a selected time gate). The C-scan is achieved by a process called gating. This removes the backwall and front wall (surface) of the inspected sample, with the focus then on the amplitudes of the internals. These are best illustrated in Figure 4.5.

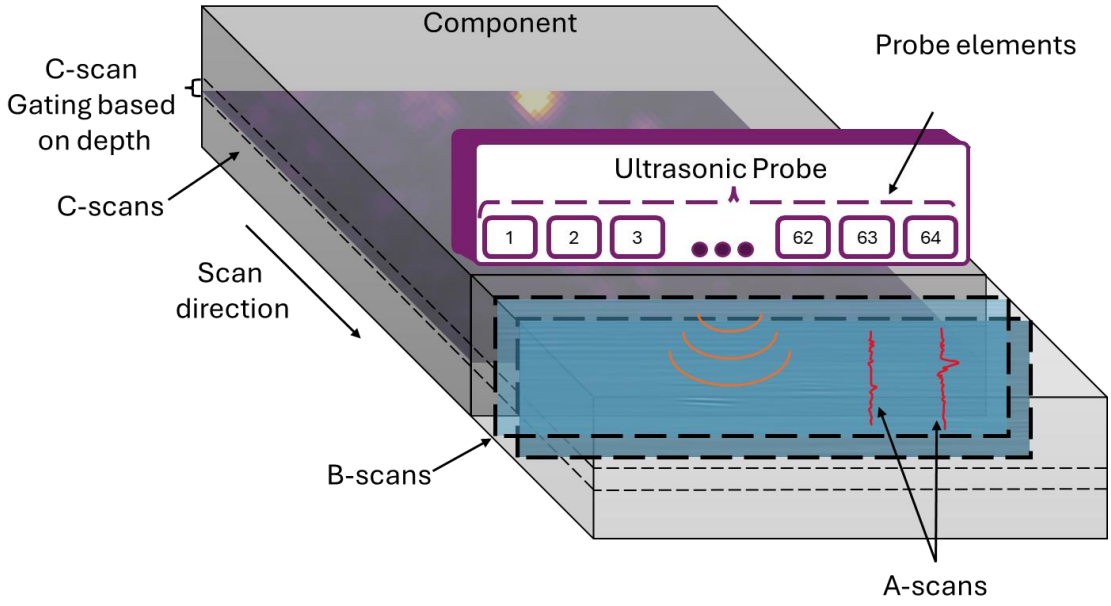


*Figure 4.5. Representation of A-scans, B-scans and C-scans within volume of inspection component*

### 4.2.4. Component Identification

Components are placed within the camera's field of view and the robot's work envelope. The working envelope is illustrated in Appendix A – Camera Spatial Resolution [123]. It is necessary to distinguish the component from the surrounding workspace, to allow for flexible path planning.

To extract the shape of the component from the 3D scan, which captured both the component and the workspace, a process to transform the initial point cloud into usable extracted data was necessary. This process began with point cloud filtering to extract the component's shape, as illustrated in Figure 4.6.

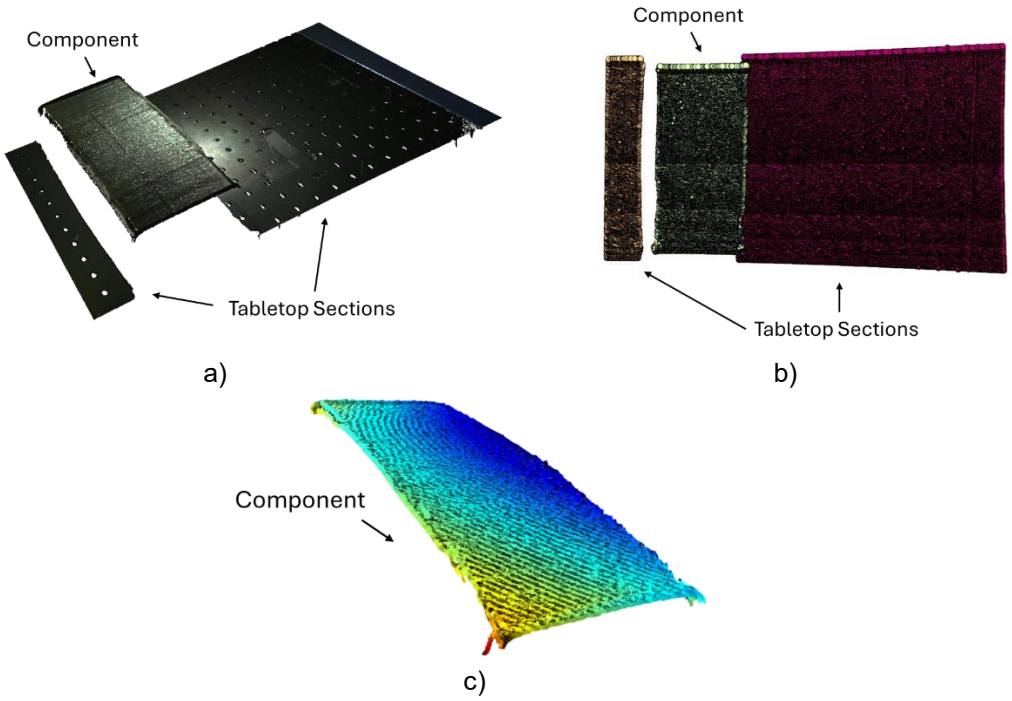


*Figure 4.6. 3D point cloud of complex component extraction, a) Initial captured region including parts of the table and the component. b) Estimated clusters from the capture region. c) Extracted region of interest associated with the component.*

First, the full point cloud was down sampled. The down sampling process, done using Voxel downsampling, uniformly reduced the size of the point cloud, decreasing the overall amount of data required to process, without losing key information such as overall shape, edges and unique features. The process involves dividing the 3D space into voxels, a 3D equivalent of a 2D pixel, and retaining only a single point from each. The initial data contained approximately 2 million points, which was reduced to 200,000 points. Reducing the total processing time from 50 seconds to 2 seconds. This significantly improved computational time, without sacrificing quality. The reduction factor was determined through a trial-and-error approach ensuring the same path planning outputs were achieved

with the fewest possible points, providing the best representation while reducing the computational time required.

The point cloud was then clustered using Density-Based Spatial Clustering of Applications with Noise, DBSCAN [130]. This algorithm facilitated the clustering of data points through density-based concepts of clusters. It is an effective tool for identifying arbitrary shapes while distinguishing them from noise. The cluster density parameter of interest was *eps*, defined as the maximum distance between two points for one to be considered within the neighbourhood of the other. Through trial and error, this value was set to 2.5. The minimum cluster size was set to 10,000 points. The component of interest was subsequently extracted by analysing the relationship between cluster density and positional elevation. The relationship was defined to identify the largest cluster at the highest elevation, with thresholds applied for both the number of points and elevation. This methodology resulted in the successful extraction of the component of interest, as demonstrated in Figure 4.6 c) above.

### 4.2.5. Flexible Path Rasterisation

Path rasterisation refers to the process of planning the trajectory that the robot will follow for the PAUT inspection. Path rasterisation is usually completed manually or uses CAD to teach and create paths that can then be mapped onto identified components. For this chapter the path rasterisation, like the extraction, is fully automated. The process takes in several fixed parameters related to the ultrasonic inspection, which influence the lengths and sizes of the scan paths and can be modified for each capture. The parameters that influence the path rasterisation are:

- Probe Width - Determines how many passes are required to fully cover the component's surface area,
- Probe Length - Dictates the length of the passes within the area,
- Overlap - Used to avoid missing any areas of interest between the passes within the component,
- X and Y offsets - Set the boundaries of inspection

The probe width and length are illustrated in Figure 4.7. The PAUT was of dimensions 110 x 65 x 70 (Width x Length x Height) mm.

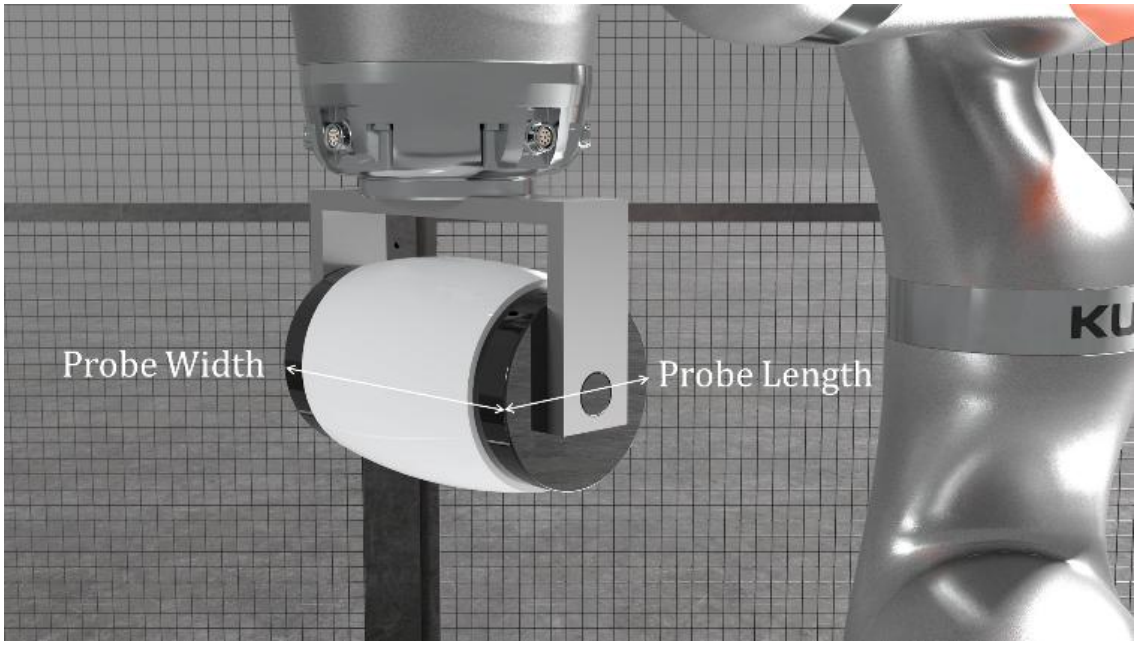


*Figure 4.7. PAUT Probe Width and Length*

The overlap between passes is demonstrated in Figure 4.8, showing the effect of no overlap between passes in an inspection, Figure 4.8 a) and highlighting the effect of the overlap between passes, Figure 4.8 b). At the ultrasonic level, there are multiple

approaches for processing overlapping data. One approach involves completely overwriting the data, though this method forfeits the potential advantages of the overlapping information. Alternatively, the data can be compounded by retaining the maximum values from the overlapping regions, leveraging the strongest signals. Another option is to average the overlapping data, which provides a balanced representation within the overlapping regions.

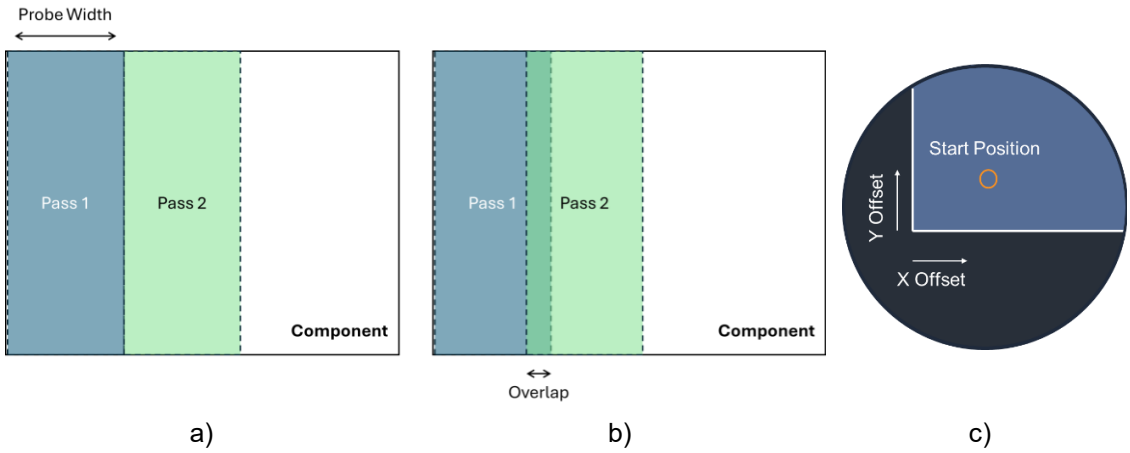


*Figure 4.8. Path parameter influences – a) Path planning without the influence of Overlap, b) Overlap parameter influences for path planning, c) Influence of X and Y offsets for the position of inspections respective to the component*

The overlap in this work was 30 mm. Since the array is not centred within the roller probe, this overlap guarantees the acquisition of complete data during the PAUT inspection process, eliminating any gaps between passes.

Since the X and Y offsets determine the inspection areas, larger offsets create a greater distance between the edges resulting in smaller scan regions, exemplified in Figure 4.8 c). This helped reduce the chances of damaging the probe, as it would not be placed on hard edges or run off the samples. The path automatically adjusted to best fit all the parameters within the constraints of the panel, generating a unique path.

The path planning process is carried out using the flood fill algorithm [131]. The flood fill algorithm is based on the concept of water flowing from a higher elevation to a lower one. The algorithm works by giving each cell in a grid a number that represents its elevation, like a map of hills and valleys. Larger numbers mean higher ground, and smaller numbers mean lower ground. The middle squares are set to zero, which means they're the lowest point—like a dip in the land. This setup lets the algorithm mimic how water would naturally flow downhill from higher areas to lower ones. [132]. The flood fill algorithm solves mazes by simulating water filling the maze from the entrance, with the shortest path to the exit marked by the first drop to reach it. It is effective at finding all possible paths and the optimal one. An example pseudocode of the algorithm is presented in Appendix B – Flood Fill Path Finding Pseudocode.

This method is utilised to adapt to more complex shapes that may not have straight boundaries, and gaps or holes in the parts. The normal of each point within the path is also calculated and extracted. This allows the robot to position and orient itself normal at each point within the path, ensuring that the probe alignment can be optimal.

This algorithm built upon a previous study [133] by incorporating additional defined parameters to more effectively fine-tune the calculated path. While previous research focused on ensuring complete surface coverage for effective PAUT inspection, it did not account for the limitations of probes designed to move in only one dimension. To address this, the path planning was enhanced to allow the probe to retract between passes, ensuring safe movement to the next pass. Careful alignment of the lift-off points with the normals of target points was incorporated to prevent probe drag or damage, while ensuring

sufficient elevation to avoid collision with the target object. Additionally, the algorithm was further refined by integrating the extra parameters described in this section, optimising the path for this specific application. These extra parameters add significant flexibility to the algorithm, allowing it to accommodate a wide variety of probes with different sizes and path constraints.

### 4.2.6. Robotic Transformation

With calculations and path planning conducted using the points relative to the camera's viewpoint, a transformation from camera's viewpoint to robot frame was required. For this reason, Hand-Eye calibration was required to understand the spatial relationship between the camera and the robotic manipulator [134].

Hand-eye calibration computes the transformation matrix that maps the robot's coordinate system ($H_{EE}^{ROB}$) to the camera's coordinate system ($H_{OBJ}^{CAM}$). This transformation allowed the robot to accurately interpret and act on visual information, ensuring that movements align with what the camera perceives. The process required taking multiple views of a reference object, in this case a calibrated checkboard, and then creating a transformation matrix to relate the views to robotic poses [135].

To ensure high-quality calibration, the robot adopted a set of distinct poses while capturing images of the calibration object, utilising all available joints. This variety in poses resulted in different viewing angles, providing diverse perspectives. A variety of poses were necessary to provide independent and diverse data for solving the hand-eye calibration equations. The use of a diverse range of relative transformations ensured a well-

constrained problem, allowing accurate computation of the transformation between the robotic manipulator and the camera.

The transformations in the setup are presented in Figure 4.9, with the final robot to object transformation obtained explained using the equations (4.1) and (4.2). Equation (4.1) gives the transformation for the whole object, whereas equation (4.2) deals with a specific point on the object. *H* represents the transformation matrix, and *p* represents a point. *CAM* represents the 3D camera, *EE* is the end effector, *OBJ* represents the object being inspected and *ROB* is the robot base.

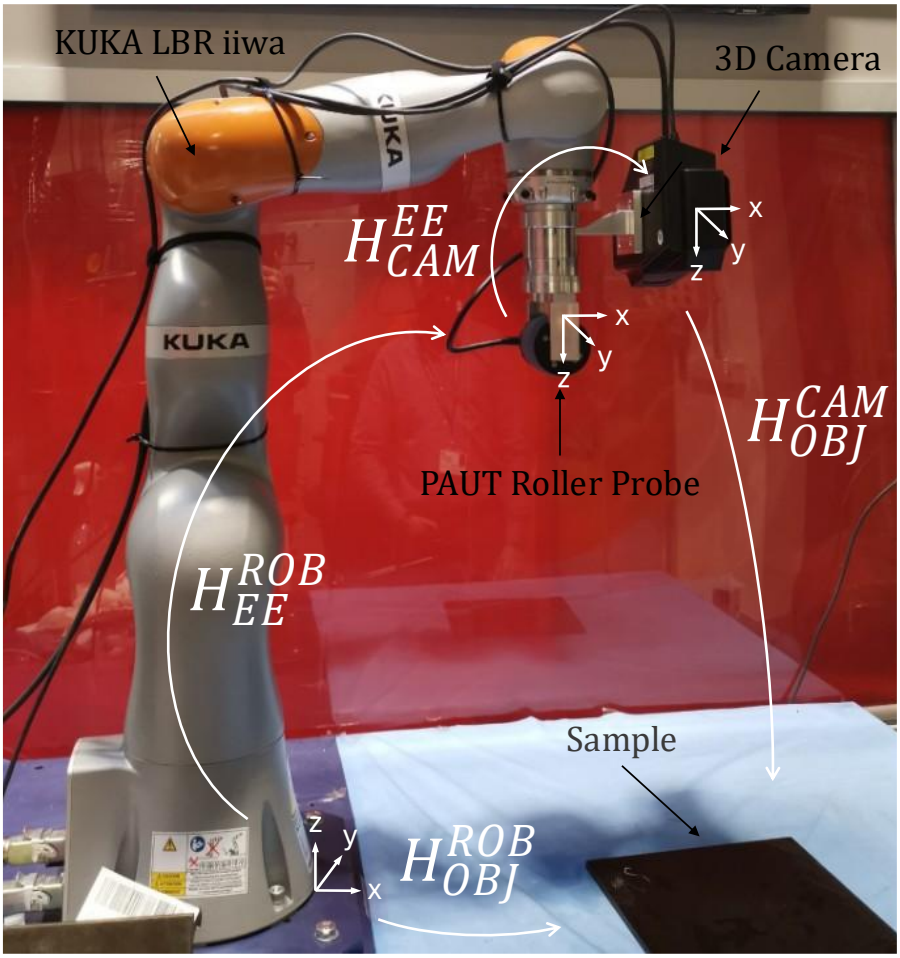


*Figure 4.9. Robotic transformations in setup. (CAM = Camera, EE = End Effector, OBJ = Object and ROB = Robot)*

$$H_{OBJ}^{ROB} = H_{EE}^{ROB} \times H_{CAM}^{EE} \times H_{OBJ}^{CAM} \quad (4.1)$$

$$p^{ROB} = H_{EE}^{ROB} \times H_{CAM}^{EE} \times p^{CAM} \quad (4.2)$$

With these calculations the points for path planning were converted into the robot frame and then applied. The verification of the hand-eye calibration was carried out using a touch test with a spike mount, which is further described in Appendix C – CAD for Experimental , Section C-2.2. Spike Probe.

### 4.2.7. Force-controlled Phased Array UT Inspection.

The manipulator doesn't have an external force-torque sensor but has inbuilt torque sensors in each of its joints. To calculate the force-torque experienced at the end effector the compound forces and torques experienced on each joint were taken into consideration.

It was assumed the total work done in both Cartesian and joint space is conserved. This gives the kinematic relationship between joint space and Cartesian space which is defined as:

$$\tau \cdot d\theta = F \cdot (J \cdot d\theta) \quad (4.3)$$

Where, $J = Jacobian\ Matrix\ (6 \times 7)$ for a 7-DoF Robot. $d\theta$ represents the vector of infinitesimal join displacements. $F$ represents the Cartesian force-torque vector. $\tau$ represents the vector of joint torques. Which can be simplified to:

$$\tau = J^T F \tag{4.4}$$

For 7-DoF, the Jacobian Matrix is $(6 \times 7)$. Therefore, the system is redundant. To handle this, the Moore-Penrose inverse [136] $J^+$can be used to express Cartesian forces in terms of joint torques.

And therefore, it can be solved for *F* as:

$$F = (J^T)^+ \tau \tag{4.5}$$

Where,

$$(J^T)^+ = (JJ^T)^{-1} J \tag{4.6}$$

To achieve precise execution of the path planning positions, it was essential to identify the appropriate scenarios for applying the force-torque control. This enabled the robot to lift off the probe from the surface between passes and transition smoothly to the next location, which was vital for preventing any potential damage to the probe tire that could arise from dragging it along the surface while moving between scan points. To correctly make these decisions, a decision tree was created and is presented in Figure 4.10.

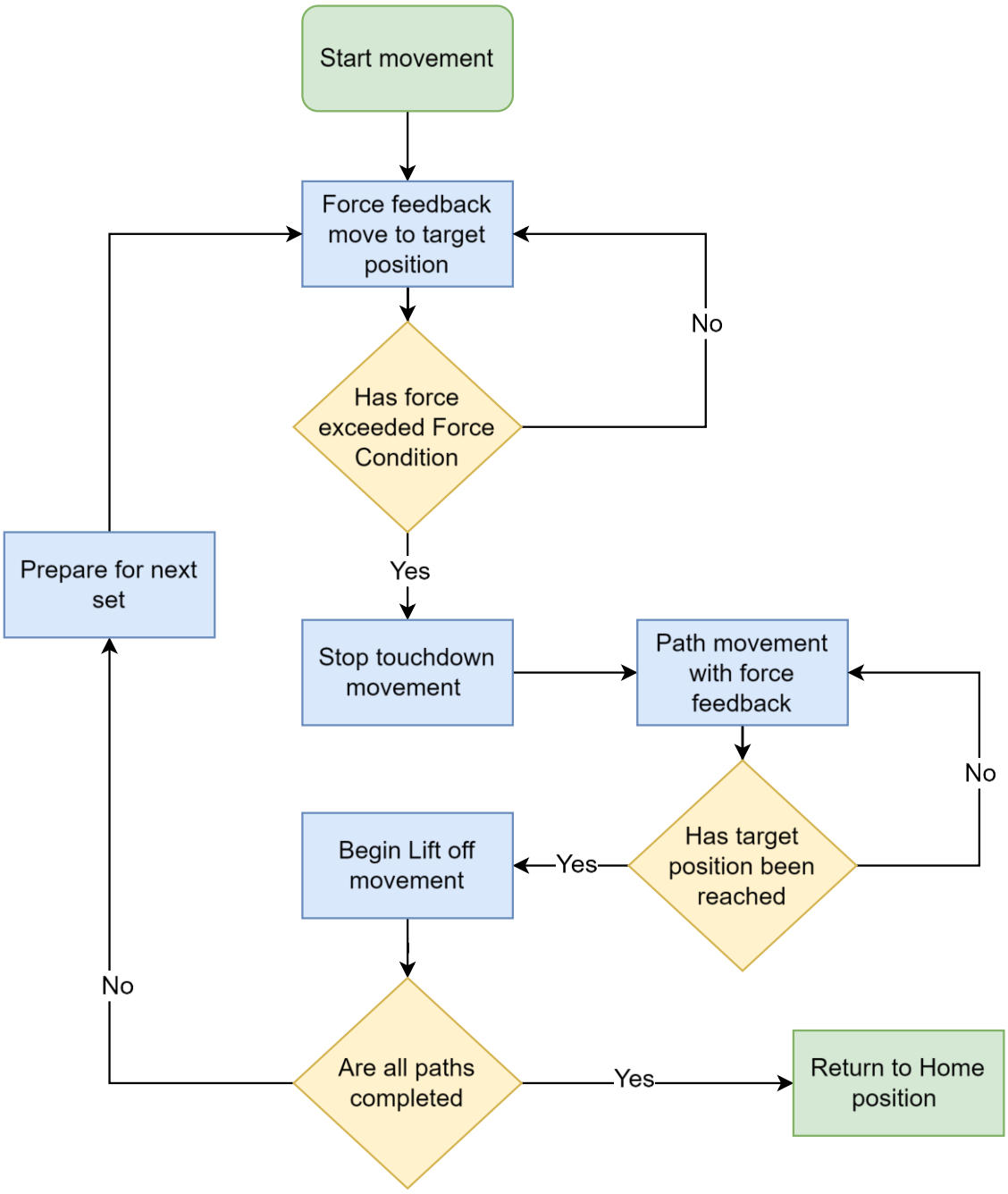


*Figure 4.10. Simultaneous force position control touchdown and path execution decision tree*

Upon arrival at the target location, the touchdown procedure was initiated using force feedback, as presented in the diagram of Figure 4.10. Once the target force, 55 N in this case, was reached, the touchdown movement was concluded and the path movements with the force feedback enabled commenced. The force feedback system was controlled by predefined force conditions, ensuring that the appropriate working force was applied to the panel surface based on the requirements for effective surface contact for ideal UT transmission. When completed, the lift-off procedure was triggered, to either move onto the subsequent target path, repeating the decision tree again, or return to the home position.

With the path planning procedure established, robotic movement was facilitated by a custom communication tool developed using Java and Python. The processed path positions were sent from Python to Java, where they were integrated into the LBR control system. This was necessary due to the LBR controller being programmed using Java. The Java side decoded the positions into commands following the decision tree in Figure 4.10, allowing the robot to realign itself with the panel before proceeding to the target locations.

Data acquisition was performed using position-based encoding, where ultrasonic captures were triggered once a predetermined distance was traversed. These captures occurred only when the robot moved along the component's surface, ensuring that the capturing process was inactive during lift-off transitions.

## 4.3. Inspected Samples

To diversify the application scenarios and demonstrate the effectiveness of the proposed setup, several samples with varying materials and geometries were scanned. These are described below.

### 4.3.1. Sample A

The first sample was a CFRP test coupon, measuring 254.0 x 254.0 x 8.6 mm (width x length x thickness), manufactured by Spirit AeroSystems, UK. It was constructed from woven carbon fibre fabric sheets and Cycom 890 resin, following the BAPS 260 standard. A series of Flat-Bottom Holes (FBHs) were drilled into the sample to simulate acoustic signals similar to delamination, a common defect in composite materials. A total of 15 FBHs were embedded, with diameters of 3.0, 6.0, and 9.0 mm (with ±0.2 mm tolerance) at depths of 1.5, 3.0, 4.5, 6.0, and 7.5 mm (with ±0.3 mm tolerance), measured from the front surface of the sample. The surface profile was flat and smooth, and the sample was inspected both flat on the table and angled using a custom stand. Schematics of the inspected sample are shown in Figure 4.11.

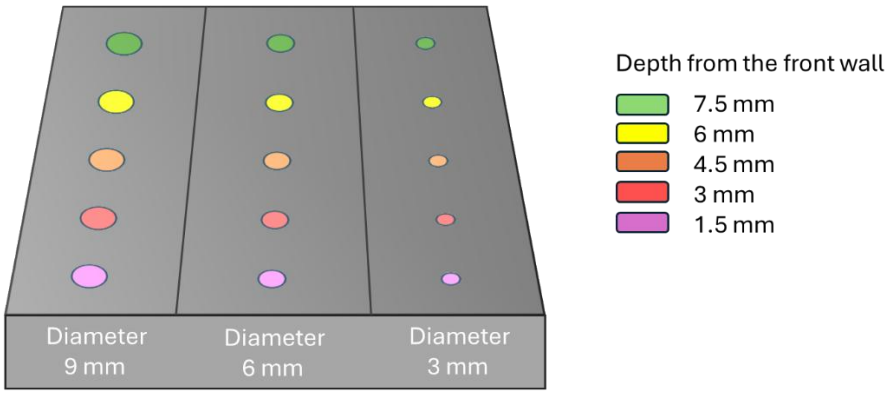


*Figure 4.11. Schematic of Sample A*

### 4.3.2. Sample B

The second sample was curved, machined from an aluminium billet. Computer Numerical Control (CNC) machining was used to fabricate the sample with the dimensions of 100.0 x 300.0 x 20.0 mm (width x length x thickness). The arc of the sample has a radius of 900 mm, with arc length of 300 mm. FBHs were drilled into this sample to simulate defects at varying depths within the sample. 15 total FBHs were drilled normal to the surface all with diameters of 3.0 mm. 5 rows of defects were drilled at depths 5.0, 10.0, 15.0, 10.0 and 5.0 mm from the inspection surface. The depths were mirrored with respect to the centre plane to validate the signal responses from both sides of the inspection. The surface profile of each hole was finished flat and smooth, with the design schematics presented in Figure 4.12.

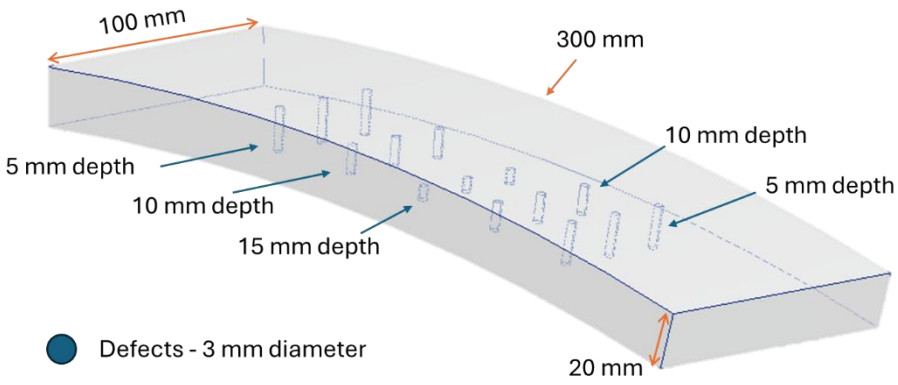


*Figure 4.12. Schematic of Sample B, and the distribution of 3mm in diameter FBHs located at depths ranging from 5 mm to 15 mm*

### 4.3.3. Sample C

The sample was made using 15 layers of XC130 150 g unidirectional prepreg [137]. Prepreg refers to composite fibres that already contain a specific amount of resin. The

fibres were unidirectional, meaning all the fibres in each layer were aligned in the same direction, which provided high strength along that direction. Each individual layer (ply) had a thickness of 0.15 mm.

The sample was enclosed in a sealed vacuum bag, and a vacuum was applied to ensure a consistent fibre volume fraction (the proportion of fibre relative to resin) across the entire thickness of the finished laminate, important for maintaining consistent mechanical properties. The vacuum-bagged sample was then cured in an autoclave; a high-pressure oven used for composite processing. Curing was carried out at a temperature of 100 °C, with the temperature increased at a controlled rate of 2 °C per minute. During this process, a pressure of 0.101 MPa (equivalent to 1 atmosphere or approximately 14.7 psi) was applied and maintained for 2 hours. This pressure and temperature ensured proper consolidation of the layers and improved fibre-resin bonding.

This sample was built to the dimensions of 105.0 x 310.0 x 6.0 mm, (width x length x thickness), radius of 900 mm with the no intentional defects. The sample design is shown in Figure 4.13.

*Figure 4.13. Sample C design*

## 4.4. Results

### 4.4.1. Hand-Eye calibration result

The results of the Hand-eye calibration presented a 4x4 matrix with the angular and positional transformations of the 3D camera relative to the flange of the LBR iiwa robot. The resultant matrix is presented in Equation (4.7), rounded to 3 significant digits. The matrix was utilised to transform all the points and captured information into the robot frame.

$$H_{FLANGE}^{CAM} = \begin{bmatrix} 0.0209 & 0.999 & -0.0156 & -141 \\ -0.985 & 0.0179 & -0.173 & 52.9 \\ -0.172 & 0.0190 & 0.985 & 60.6 \\ 0 & 0 & 0 & 1 \end{bmatrix} \quad (4.7)$$

### 4.4.2. PAUT inspection results

The samples examined in this chapter were selected for specific testing purposes. Sample A, a CFRP sample with known defects, was tested to verify the system's ability to accurately detect these defects, with their varying depths and sizes, within a complex material matrix.

Sample B was used to assess the system's performance on non-planar surfaces, testing the robot pose control responsiveness and accuracy ensuring that critical factors such as probe alignment and coupling were effectively maintained for a complete inspection. Sample C was also employed to evaluate the system's capability in inspecting a non-planar and challenging anisotropic material where slight non-optimal pose control could lead into considerably poorer SNR as compared to the case of Sample B.

#### 4.4.2.1. Sample A

A fixture was constructed to enable the Sample A CFRP panel to be positioned in different poses. The design of the fixture is provided in Appendix C – CAD for Experimental , Section C-3. Fixtures. This meant that the system could be tested at various poses. The fixture's orientation (pitch) was adjusted between -30° and 30° in 10° increments around y axis as shown in Figure 4.14. Noteworthy that the coordinate system used in this figure is matched to the one presented in Figure 4.4.

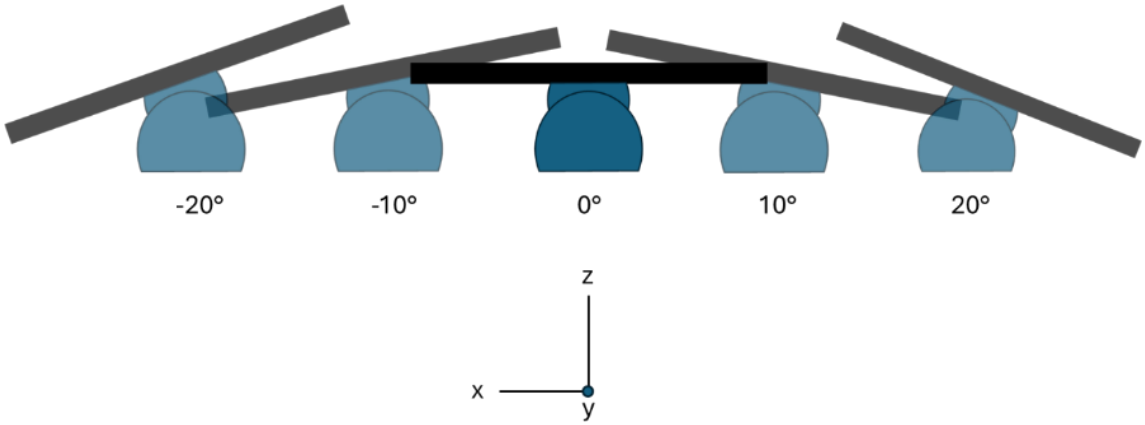


*Figure 4.14. CFRP inspection orientations*

To sustain the quality of acquired data, a coupling force of 55N between the roller probe and the sample was applied using the flexible system presented here, with a scanning speed of 25 mm/s. The C-scans captured at different orientations of Sample A in the inspection volume are shown in Figure 4.15. Due to the nature of the path planning being adaptive and unique for each inspection, some defects were spaced differently.

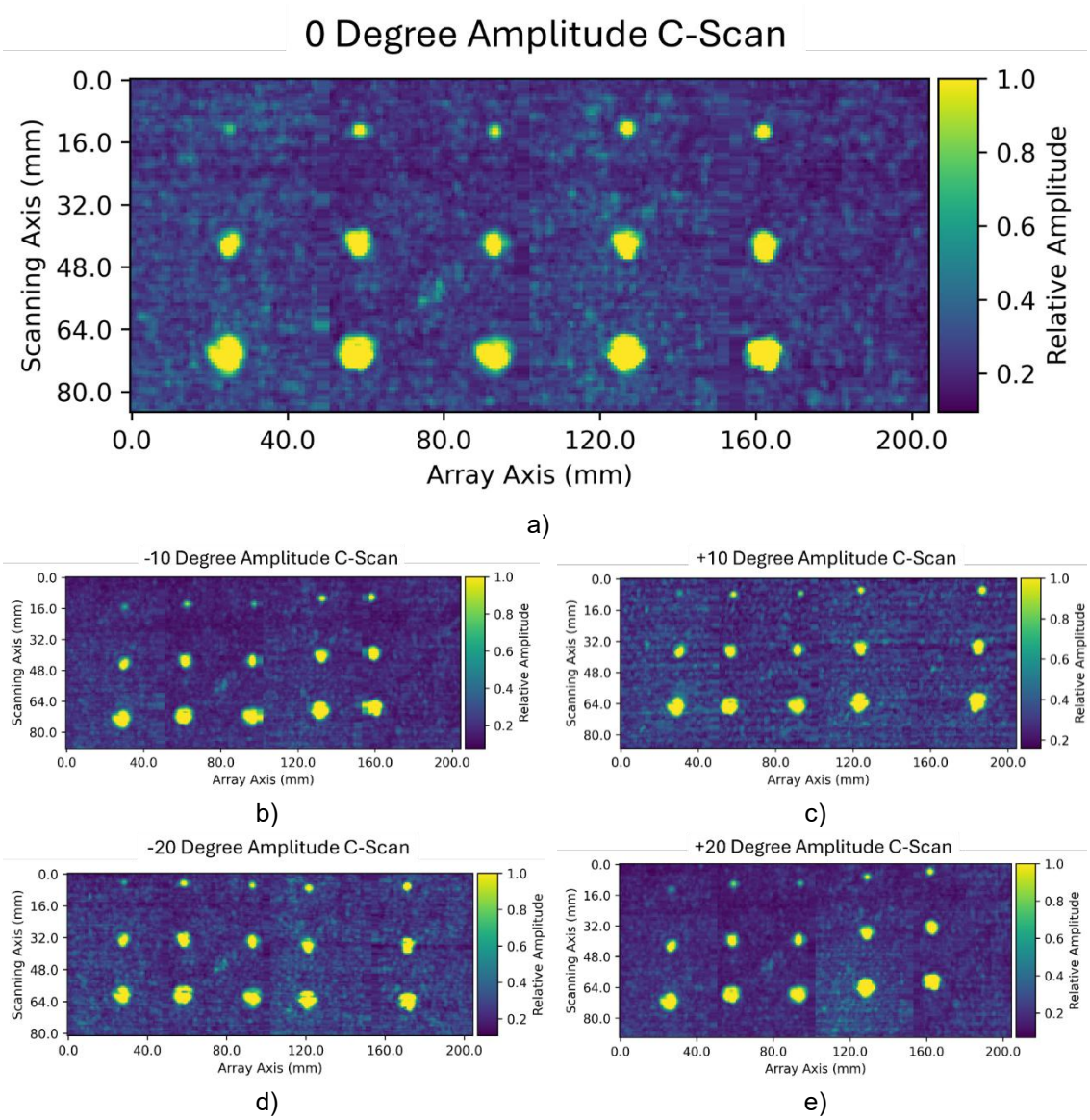


*Figure 4.15. Amplitude C-scan results for the test Sample A varied orientations, a) 0-degree orientation, b) -10-degree orientation, c) +10-degree orientation, d) -20-degree orientation, e) +20-degree orientation.*

The C-scan results with the flexible approach successfully imaged the known defects in their expected locations, showcased in Figure 4.15. To further the results validity there was a need to quantify the results statistically rather than purely visually. The 6 dB drop method is a common industry practice for sizing flaws based on UT signals. This

technique involves identifying the peak amplitude of the reflected signal from the flaw and then determining the position along the component where the amplitude drops by 6 dB. For the analysis of the CFRP panel the 6dB drop method was used.

The detected regions of the 6 dB drop method are shown as blue highlights for the amplitude C-scans in Appendix D – 6 dB drop CFRP plots.

To allow for comparative analysis between the captured scans, Peak Signal-to-Noise-Ratio (PSNR), and defect sizes are reported. PSNR was calculated as a metric to assess the contrast relative to theoretical maximum signal value (i.e., the maximum possible value in a normalised image), using equation (4.8):

$$PSNR_{dB} = 20log_{10}\left(\frac{I_{max}}{\sigma}\right) \tag{4.8}$$

Where $I_{max} = 1.0$ for normalised scans. A high PSNR indicates a strong, clearly detectable signal, which is crucial for accurate flaw detection, sizing, and sentencing when it comes to data analysis. Conversely, low values imply poor contrast, increasing the risk of false positives (detecting a flaw where there is none) or false negative (missing an actual flaw).

The amplitude response was also measured and is split into the different sizes of the defects present in this sample (3, 6, and 9 mm). This has been combined with the PSNR data for the various orientations, presented in Table 4.2.

*Table 4.2. Results of 6dB drop method for defect amplitude and PSNR for CFRP orientations inspection*

| Experiment | 3 mm mean | | 6 mm mean | | 9 mm mean | | PSNR (dB) |
|---|---|---|---|---|---|---|---|
| | Amplitude | SD | Amplitude | SD | Amplitude | SD | |
| **0°** | 0.77 | 0.16 | 0.85 | 0.17 | 0.88 | 0.17 | 17.15 |
| **-10°** | 0.70 | 0.12 | 0.82 | 0.19 | 0.87 | 0.17 | 17.37 |
| **+10°** | 0.73 | 0.14 | 0.84 | 0.17 | 0.87 | 0.17 | 17.92 |
| **+20°** | 0.67 | 0.12 | 0.85 | 0.17 | 0.88 | 0.16 | 17.39 |
| **-20°** | 0.77 | 0.16 | 0.84 | 0.18 | 0.87 | 0.17 | 17.31 |

The data reveals several positive insights regarding the captured information. As expected, the larger defects consistently produce higher and more stable amplitude signals, indicating good sensitivity of the method to defect size. The smallest defects of 3mm diameter also produced a signal response on average of at least 70% of peak signal, indicating that even the harder defects to correctly image and identify are consistently found. Additionally, PSNR values remain high and consistent across all experiments, demonstrating the system's ability to reliably detect strong signal reflections regardless of angle.

The sizing was also analysed for the CFRP inspections. The 6dB method utilised identified all 15 defects in each experiment. The defect sizes were found using a mask of the surface area, which was then converted back to the diameter. The defects in each experimental

result set were found to be slightly oversized consistently with this method. The results of the sizing are presented in Table 3.

*Table 4.3. Results of 6dB drop method for defect sizing – a) Mean absolute difference, b) Percentage difference*

| Real Size | Absolute Difference (mm) | | | | |
|---|---|---|---|---|---|
| | **0°** | **-10°** | **+10°** | **+20°** | **-20°** |
| **Row 1 – 3mm** | +1.12 | +0.59 | +0.83 | +0.69 | +1.27 |
| **Row 2 – 6mm** | +1.47 | +1.10 | +1.26 | +0.72 | +1.52 |
| **Row 3 – 9mm** | +1.18 | +1.05 | +1.12 | +0.72 | +0.91 |

**a)**

| Real Size | Percentage Difference (%) | | | | |
|---|---|---|---|---|---|
| | **0°** | **-10°** | **+10°** | **+20°** | **-20°** |
| **Row 1 – 3mm** | +37.47 | +19.53 | +27.53 | +42.27 | +23.07 |
| **Row 2 – 6mm** | +24.57 | +18.30 | +20.93 | +25.27 | +12.00 |
| **Row 3 – 9mm** | +13.13 | +11.67 | +12.47 | +10.11 | +8.02 |

**b)**

The results of Table 4.3 show that the lowest errors overall are in the 9mm row, especially at -20° (8.02%), suggesting that larger defects are detected more consistently utilising the

6dB drop method, and the signal from the smaller defects is more vulnerable to improper sizing.

#### 4.4.2.2. Sample B

As done with the CFRP panel, the force used in this inspection was 55 N. To illustrate the effectiveness of the systems capabilities, the inspection was conducted using two different methods.

1. Automated Identification and Inspection with presented system
2. Manually taught and positioned robotic inspection

It should be noted the setup and processing for automated system was less than 1 minute, with 30 seconds for the capture with the 3D camera, and 20 seconds for the processing and path planning. Compared to the manual setup, which required 1 minute for fixturing alone, and a total of 15 minutes for the UT calibration and setup, teaching of points and fixturing for a sample 100.0 x 300.0 mm in dimension. Since this was a new sample, programming the procedure for the robot took a further 25 minutes. This procedure could be even more time consuming with larger real-world components.

The resultant data was max-normalised, meaning all values were divided by the maximum value within the dataset, and subsequently statistically analysed. As done with the CFRP the 6 dB drop was used for the analysis of features within the sample. This presents the ability to compare defect amplitude and PSNR. To understand the performance of the presented system, statistical analysis of defect amplitudes was conducted. The defects were sectioned to apply the 6dB method individually. This identified the regions

corresponding to amplitude levels greater than half of the total signal amplitude. The C-scans for the respective inspection methods, and 6dB method for finding the defects are presented in Figure 4.16. The blue highlights in Figure 4.16 b) and d) show the regions detected as amplitudes above half power and assumed defective regions.

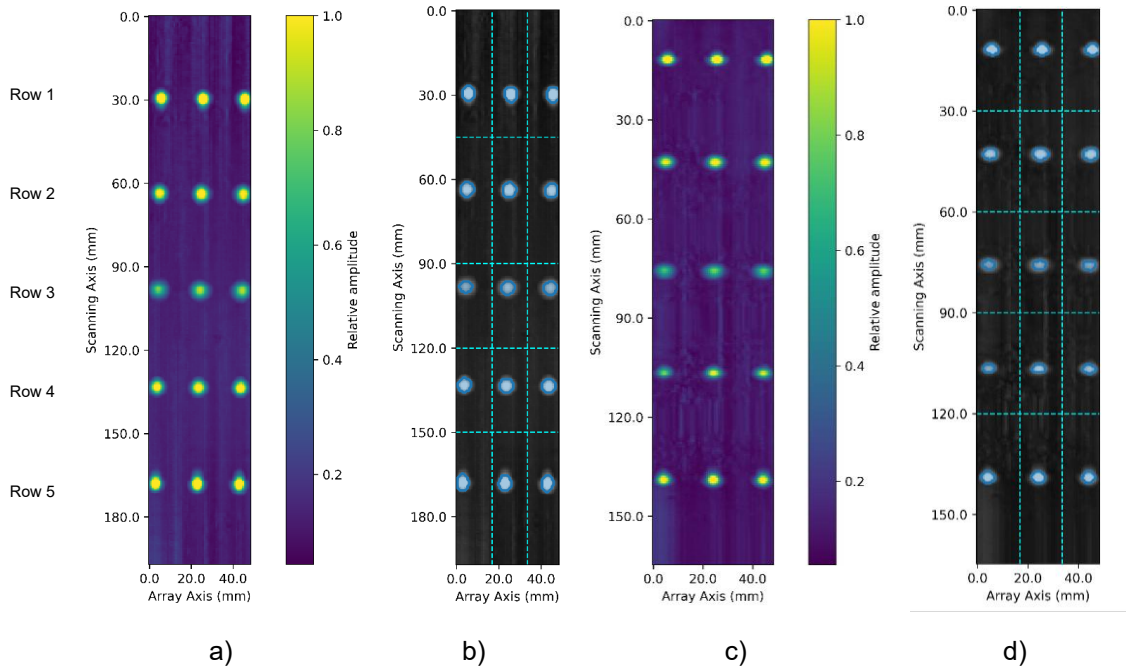


*Figure 4.16. C-scan results for testing the complex aluminium component. a) Inspection using the automated robotic system, b) Amplitude C-scan from the automated system with a 6 dB drop applied, highlighting features in blue, c) Inspection using the manually taught method, d) Amplitude C-scan from the manual method with a 6 dB drop applied, highlighting features in blue.*

The results of the automated system are shown in Figure 4.16 a) and b), as an amplitude C-scan and highlighted regions of 6dB method respectively. Similarly, the manually taught method results are presented in Figure 4.16 c) and d). The results of Figure 4.16 show that the C-scans from both methods capture all defects successfully and all defects can be clearly identified by the 6dB drop method.

The defect amplitudes were then averaged across each row, to present a comparative mean amplitude and SD of defect amplitude. These extracted amplitude results are presented in Figure 4.17, and in Table 4.4 with the standard deviation.

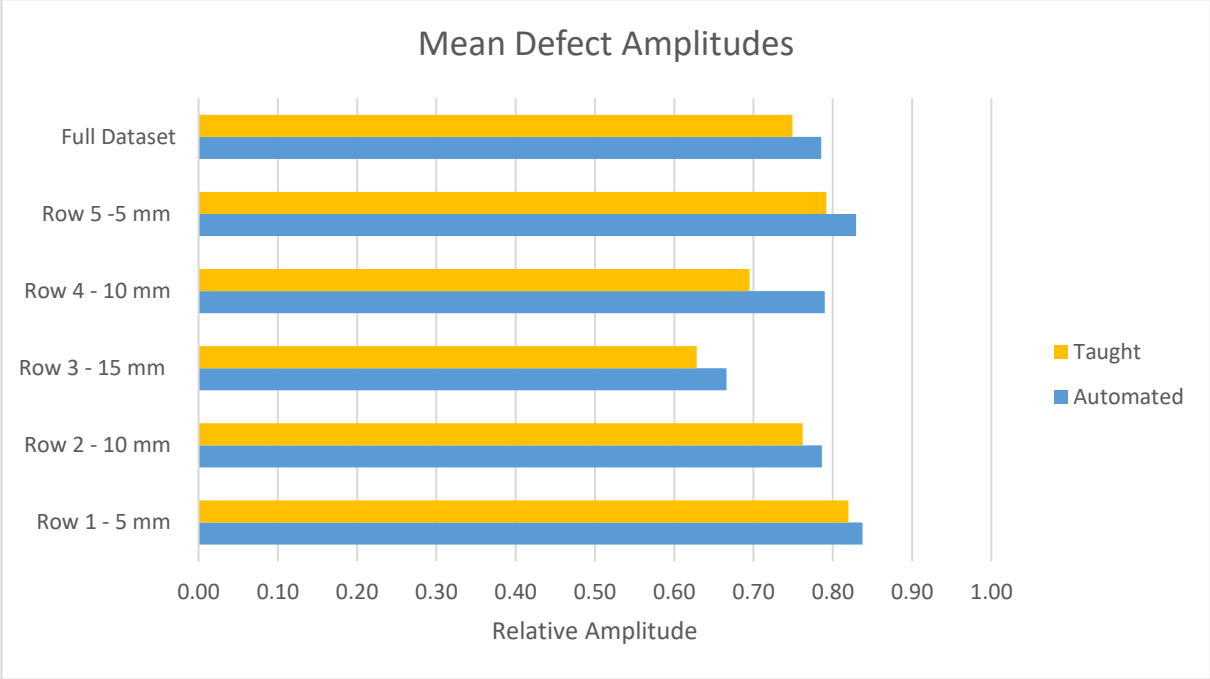


*Figure 4.17. Mean Defect Amplitudes for both inspection methods of complex aluminium sample*

*Table 4.4. Defect Amplitude Standard Deviation for both inspection methods of complex aluminium sample*

| Depth | Automated SD | Taught SD |
|---|---|---|
| **Row 1 - 5 mm** | 0.17 | 0.18 |
| **Row 2 - 10 mm** | 0.17 | 0.17 |
| **Row 3 - 15 mm** | 0.12 | 0.08 |
| **Row 4 - 10 mm** | 0.17 | 0.15 |
| **Row 5 - 5 mm** | 0.18 | 0.18 |

The mean amplitude results of Figure 4.17 showed that the fully automated system consistently achieved higher mean amplitudes than the taught system, with a mean improvement of 4.25% and the largest difference of 9.46% on the 4$^{th}$ row of the scan. The mean amplitude across the full dataset indicated that the automated inspection performed better by 5.34%. Overall, both systems showed comparable variation, as seen in Table 4.4, but the automated system (0.175603) had marginally less spread of performance across the full dataset, having had a slightly lower SD than the Taught system (0.175696), a difference of 0.000093, suggesting slightly better overall consistency.

With the 6dB drop method sizing was also investigated. This sizing method is not fully accurate, as it struggles with smaller defects and is susceptible to uncertainties caused by signal diffraction at defect edges [138] but does provide a comparative result. The calculated size of the features was based on the area found in the 6dB drop, correlating the pixels measured to the area from scan interval and pitch between elements in

millimetres. All features were found to be oversized with this method, for both methods. These results are shown in Table 4.5.

*Table 4.5. Results of 6dB Sizing of complex aluminium sample inspection*

| | Automated | | Taught | |
|---|---|---|---|---|
| **Depth** | Abs Diff (mm) | Diff (%) | Abs Diff (mm) | Diff (%) |
| **Row 1 - 15 mm** | 2.67 | 89.00 | 2.05 | 68.44 |
| **Row 2 - 10 mm** | 2.74 | 91.44 | 2.29 | 76.22 |
| **Row 3 - 5 mm** | 2.33 | 77.78 | 1.42 | 47.33 |
| **Row 4 - 10 mm** | 2.67 | 89.11 | 1.26 | 42.11 |
| **Row 5 - 15 mm** | 2.73 | 90.89 | 2.00 | 66.67 |
| **Mean oversizing** | **2.63** | **87.64** | **1.80** | **60.15** |

The absolute difference of the defects is based on the true size of 3 mm. The results showed that the automated system presented features consistently oversized even compared to the already oversizing manually taught method. This is consistent with the observations for the 3 mm defects in Sample A and may indicate a physical limitation from the ultrasonics and of the algorithm, arising from the small size of the defect. The significant oversizing, and the 6 dB method's difficulty with defects of this size, may also be influenced by improved coupling or optimal probe orientation, potentially resulting in stronger signal amplitudes than anticipated from standard calibration procedures. Consequently, defect sizing using this system may differ from conventional methods, indicating a need for system-specific calibration beyond standard approaches.

Even with the oversizing of the defects, the automated system showed consistently higher amplitudes for all defects compared to the manually taught system. The differences in mean amplitude between mirrored 10 mm rows were 0.04, and 0.03 for the 15 mm rows. This indicates that the system was able to accommodate the curvature of the component, maintain correct normal orientation, and accurately detect the defects regardless of the inspection side.

#### 4.4.2.3. Sample C

The final testing was conducted using Sample C, a curved composite component. The sample was constructed with the intention of being defect free, however upon inspection with the presented system an anomaly was detected. To validate and establish a ground truth an inspection using Computed Tomography (CT) was conducted. From the CT inspection, an indication was also found. The CT output is shown in Figure 4.18, which includes enlarged front and top views, focusing on the area of suspected delamination.

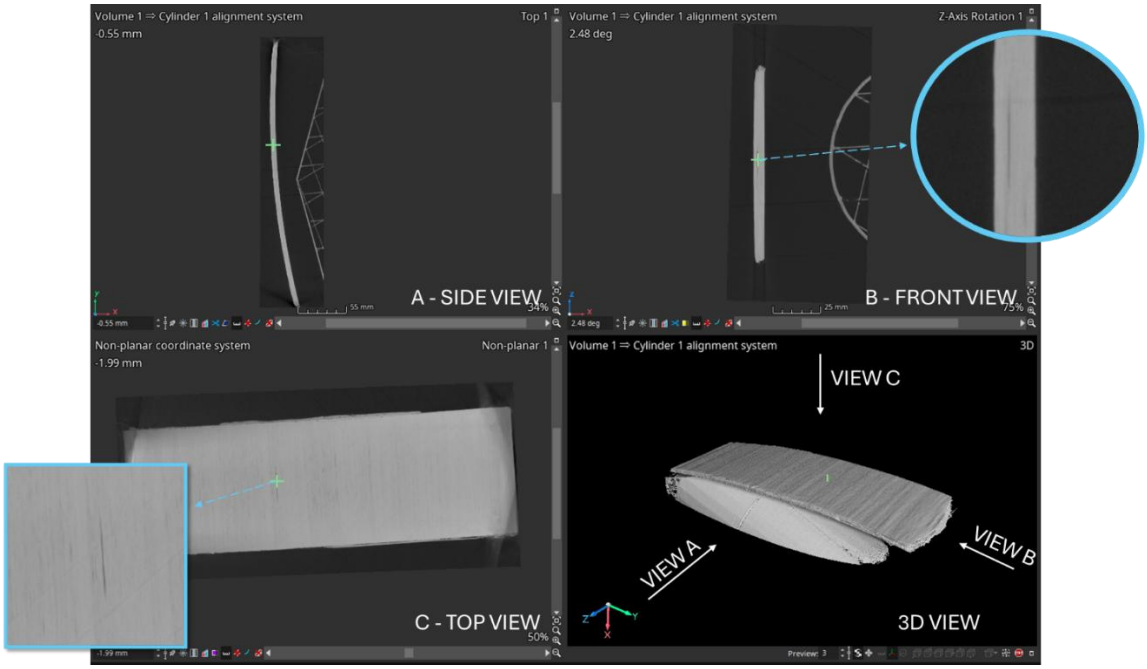


*Figure 4.18. CT scan - Highlighting possible delamination defect with multiple views– a) Side View, b) Front View c) Top View – Sliced*

The 3D view from Figure 4.18 shows the direction from which each of the perspectives originated for improved clarity. The object under the sample in the various views was used for holding the sample in place during inspection. The enlarged captures showcase the detected anomaly with the green marker in each view showing the location of the anomaly on the sample. The anomaly had the appearance of a darker line, indicating a change in density, which was most likely a delamination in this context, as it followed the direction of the ply layup.

The UT result from the presented system found the anomaly lining up with the position of the anomaly detected using the ground truth CT inspection. This was found by a notable reduction in the back wall signal indicating the presence of a possible anomaly, highlighted (orange rectangle) in Figure 4.19.

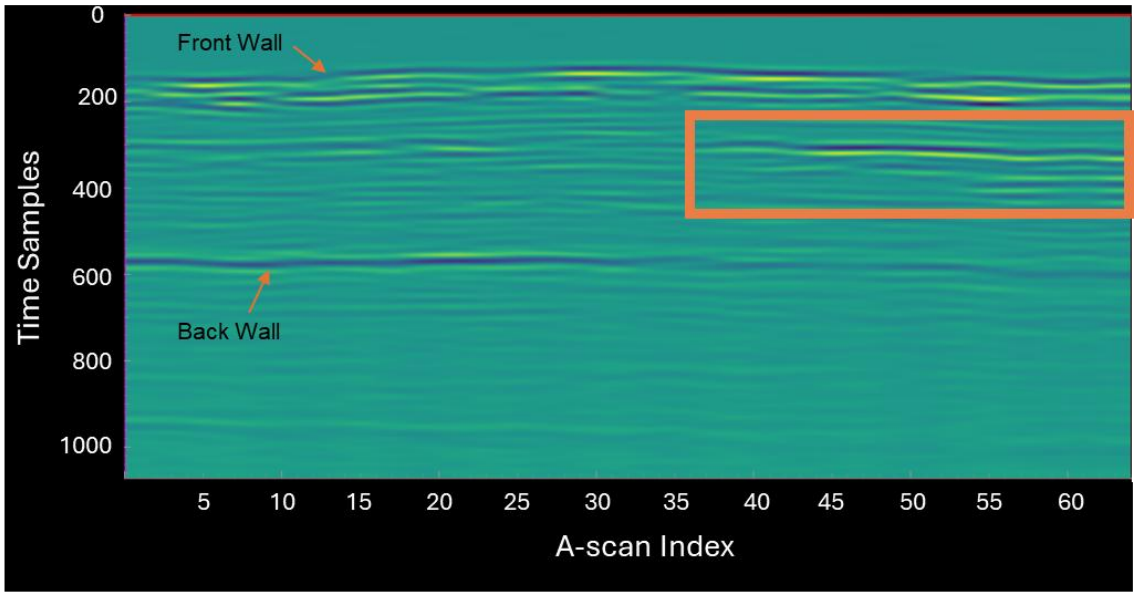


*Figure 4.19. Curved Composite B-Scan - Highlighting anomaly*

The loss of backwall shown in Figure 4.19 due to the anomaly occurs because acoustic energy is scattered, absorbed, or reflected when encountering an anomaly. This thereby limits the amount of energy that can propagate to the back wall of the sample, resulting in a weaker signal.

From the front wall, on the CT scan, the distance to the abnormality was measured at approximately 2.05 mm. From the UT B-scan, using peak-to-peak measurements, the number of time samples was extracted then equation (4.9) was used to calculate the distance of the defect from the front wall.

$$2d = vt$$

$$2d = v\frac{time\ samples}{sampling\ freq} \tag{4.9}$$

$$d = \frac{v \times time\ samples}{2 \times sampling\ freq}$$

Using an assumed speed of 2900 m/s for the speed of sound in CFRP, and the sampling frequency of 100 MHz, the distance was calculated to be 2.03 mm. Since the true speed of sound in CFRP changes depending on the internal lay and structure of the components, the resulting discrepancy between the CT and UT measurements is considered minimal.

## 4.5. Discussion

The inspection results across varying CFRP fibre orientations highlighted the scanning system's consistency and reliability in detecting embedded defects, independent of the fibre layup. The system demonstrated a stable response to defects of various sizes, with higher mean amplitudes consistently recorded for larger defects—particularly the 9 mm cases, where mean amplitudes ranged from 0.87 to 0.88. This trend confirmed the system's sensitivity to defect size and its ability to deliver repeatable performance across all tested orientations.

Even for the smallest defects (3 mm), which are typically more challenging to detect, the system maintained strong signal responses, consistently exceeding 70% of the peak

amplitude. This level of performance illustrated the system's capability to reliably capture fine features, reinforcing its suitability for inspections.

High PSNR values were maintained across all tests, ranging from 17.15 dB to 17.92 dB. Overall, the system exhibited strong and consistent performance irrespective of fibre orientation.

The 6 dB drop method was employed as a means of post-scan validation for defect sizing and presence. While it consistently identified all 15 defects across each experiment, it demonstrated a tendency to slightly oversize features, an expected behaviour of this method due to its amplitude thresholding, highlighted in previous research [139]. Table 4.3 supported this observation, with more accurate sizing recorded for larger defects, particularly the 9 mm flaw at -20° orientation, where the absolute error was limited to 0.91 mm. These sizing results reinforced the reliability of the system's detections, while also providing valuable comparative insight into defect dimensions.

Figure 4.17 illustrated the mean amplitude responses across each defect row of the complex aluminium sample, comparing the fully automated and manually taught ultrasonic inspection systems. The automated system consistently produced higher defect amplitudes across all rows, with improvements ranging from 1.79% to 9.46%, most notably in Row 4 (10 mm depth). This suggested enhanced alignment and coupling by the automated system on complex or curved surfaces. Improvements in Rows 3 and 5 further demonstrated its effectiveness across varying defect depths.

Performance across equivalent depth regions revealed strong amplitude consistency in the automated system, while the manually taught method exhibited amplitude variability, particularly in repeated 10 mm depth rows. This indicated potential sensitivity to manual path variability and surface interaction inconsistencies.

Despite greater amplitude performance, the automated system recorded a lower PSNR value of 17.1 dB compared to the 18.96 dB of the manually taught. Although the improved coupling increased the overall amplitude of the returned signals, it also may have transmitted more background reflections and grain noise, contributing to the reduction in contrast of the highest peaks relative to the noise floor.

Nevertheless, both systems maintained high SNR levels. Acceptance criteria are established in industry to grade and assess flaws identified during inspections. Such criteria are defined both by standards organisations and by individual companies, each of which may have their own specifications, for example, Spirit Aerosystems, but in this work, we did not have access to proprietary company standards. Based on ISO 11666 [140], which defines acceptance levels for defects, flaws with amplitudes greater than –4 dB relative to the calibrated reference (approximately 63% of the maximum amplitude) are considered significant. If the defects detected in this chapter were assessed according to these ISO criteria, they would all have been classified as defects.

The findings confirmed the automated system's strong defect detection capabilities through the consistently higher amplitude responses. The automated system resulted in a significant time saving of approximately 97.5%, reducing the setup and processing time from over 40 minutes to just 1 minute.

The final phase of testing involved Sample C, a curved CFRP component, which had been originally manufactured with the intent of being free from internal defects. During UT using the developed inspection system, an unexpected anomaly was identified. This finding was validated using a high-resolution CT scan. The CT scan, shown in Figure 4.18, provided detailed visualisations of the sample. Notably, each view consistently revealed a darker linear feature aligned with the fibre layup direction, indicative of a delamination. One of the most common defect types in composites where interlayer bonding may degrade or fail.

The UT result presented in Figure 4.19 identified a reduction in the backwall echo at the same lateral position as the CT-indicated anomaly, suggesting partial obstruction or attenuation of the ultrasonic signal. Loss of backwall signal typically results from reflection, scattering, or absorption of acoustic energy caused by subsurface defects such as delaminations.

Importantly, the system's ability to maintain normality to the curved surface during scanning played a significant role in accurately capturing the anomaly. Further quantitative validation was performed by measuring the depth of the anomaly. The CT scan indicated that the defect was located approximately 2.05 mm beneath the surface. Using the UT data, the defect depth was calculated at 2.03 mm. The close agreement between the CT and UT measurements showed the systems capability of capturing defects to a high degree. The slight variability has been assumed to be due to the value of the speed of sound, 2900 m/s, used in the calculations, likely different to the actual speed of sound in CFRP which varies depending on the material layup and internal structure.

## 4.6. Conclusion

An adaptable scanning system capable of identifying components whose positioning was not predetermined has been presented and it has been shown that it is possible to conduct automated NDE scans on unfixtured components at arbitrary angles and inclinations.

By combining the capabilities of the 3D vision system with different processing algorithms, areas of interest were extracted. Custom path rasterisation algorithms, utilizing many parameters that influence the PAUT results were then utilised, resulting in a flexible identification and planning system. The combined system presented in Figure 4.1 allowed the inspection process to be successful. The scans obtained successfully detected all of the known defects across various scan orientations of Sample A, the curved metallic Sample B, as well as the naturally occurring defect found in Samples C.

This system has demonstrated scanning on CFRP components in a way that is agnostic to its base orientation, providing comparable C-scans. The system has shown its flexibility, with the capability of scanning geometries with different materials and complexity. The implementation of such a system can further the collaboration between human operators and robots, enabled by the flexibility in component placement and the use of human-collaborative robots.

This chapter has succeeded in investigating the suitability of flexible human collaborative systems for PAUT inspections and the integration of an adaptable scanning system capable of identifying and scanning high-value manufacturing components regardless of orientation and with no prior knowledge. The automated system also was found to be

considerably more efficient than manually taught methods, reducing setup and processing time to under one minute, for a comparable inspection procedure. The 97.5%-time reduction presented in this chapter can translate into hundreds of hours saved annually when scaled across routine PAUT operations.

The proposed future work includes further testing of coupling methods and introducing additional components to better evaluate the system's success rate.

Future research could also focus on developing an algorithm to ensure that part placement lies within the optimal working envelope of the robotic manipulator. Certain movements, such as driving the manipulator inward or operating near its base, can be challenging. Therefore, the design of operational regions that prevent the robotic arm from entering singularities or generating unsolvable path plans would be a valuable improvement.

One current limitation of the system was that only test coupons were used, which are inherently small due to the constraints of the robotic manipulator. In future work, access to larger, real-world components would be advantageous. Looking ahead, this adaptability could be expanded to inspect specific segments within larger components, such as wing panels. By carefully rasterising sections of the component, the process can be expected to proceed seamlessly across the entire target area, ensuring thorough and effective examination.

Additionally, further refinement of the calibration procedures and improved correlation between the ultrasonic system and the robotic platform would help to enhance path planning strategies and inspection outcomes.

# Chapter 5

# A Fully Autonomous Mobile NDE Inspection System with Environment and Component-Aware Intelligence for Enhanced Ultrasonic Evaluation

## 5.1. Introduction

As introduced in Chapter 3 and Chapter 4, there exists an opportunity forming from industrial demand to introduce greater flexibility into the NDE pipeline. Building on the work explored through the quantification of mobile manipulator platforms and the inspection of components without prior knowledge, there is great potential in the combination of these works to deliver a process-to-part solution.

Current inspections conducted using robotic manipulators to streamline data acquisition and reduce human dependency [56], [141], are capable of highly repeatable and time-efficient inspections [142]. These systems are limited to fixed setups, such as gantries or

track-mounted arms. While such solutions offer high precision and some flexibility from track based systems, as demonstrated in works like Garnier et al. [143] and Mineo et al. [119], they do also come with significant limitations. These include substantial cost, large physical footprints, and limited adaptability to components of varying shape, size, or placement. Moreover, they require meticulous pre-inspection programming and assume exact prior knowledge of component geometry [92].

In contrast, as introduced in Chapter 3 collaborative mobile robots represent a new solution in automated NDE, offering both mobility and safety. These platforms are designed to work safely alongside humans without the need for protective barriers, significantly reducing the workspace footprints and enabling seamless deployment in dynamic environments [121]. These systems reverse the traditional approach, requiring components to be transported and moved within a factory environment to a stationary inspection system, to the inspection platform, now able to be brought to the part. This shift significantly enhances inspection flexibility, reducing setup times and enabling in-situ evaluation of components or fixed structures without extensive repositioning or fixturing.

The process-to-part solution offers several key advantages in terms of safety, cost, and efficiency. By enabling a flexible inspection system that moves to the components rather than requiring components to be brought to a fixed station, the need for human operators to perform potentially hazardous tasks such as fixturing and transporting large or complex parts is significantly reduced. Cost savings arise from the decreased need for handling, transportation, and custom fixturing. Moreover, this approach improves overall

manufacturing efficiency by minimising downtime and enabling in-situ inspections directly within the production environment.

By combining environmental awareness, autonomous navigation, and adaptive path planning, collaborative mobile NDE platforms can operate in unstructured or semi-structured environments. These capabilities position them as a transformative solution, bridging the gap between robotic precision and real-world variability, and enabling robust inspection workflows across a wider range of industrial applications. This chapter presents a fully autonomous PAUT solution designed to overcome current limitations through contextual intelligence and robotic mobility.

The main contributions of this work are:

- Fully Autonomous Inspection Framework: A decision-tree-based control architecture was developed to manage the entire ultrasonic inspection process, from task planning and alignment to data acquisition and reporting, without user intervention.

- Autonomous Inspection: Combines component-aware PAUT planning for automatic ultrasonic parameter selection, environment-aware logic for adaptive and reliable inspection, real-time ultrasonic-guided robotic control for optimal probe alignment and coupling, and automated data visualisation with interactive C/B-scans and 3D defect mapping, delivering a fully autonomous, end-to-end ultrasonic inspection process.

Together, these contributions present a new standard for autonomous ultrasonic inspection, integrating decision-making, adaptive planning, and real-time control within a mobile robotic manipulator. The rest of the chapter is organised as follows: Section 5.2 presents the system architecture, while Section 5.3 describes the methods developed and implemented. Section 5.4 details the experimental validation and results, followed by the discussion in Section 5.5. Finally, Section 5.6 provides the concluding remarks.

## 5.2. System Architecture

The full system architecture has been broken up into two main categories: the hardware and the software. Each of the system categories are further broken down into their individual modules and explained in the following sections.

### 5.2.1. Hardware

Figure 5.1, shows the overall system with the various hardware components. The main part of the system is the KUKA KMR iiwa mobile platform [54], as previously introduced in Chapters 2 and 3.

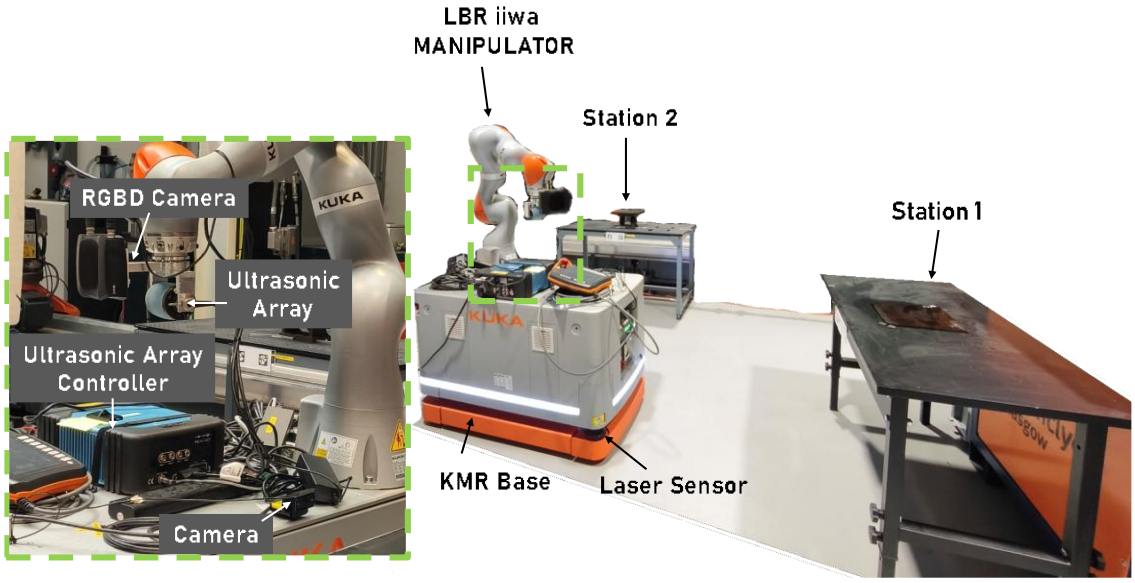


*Figure 5.1. Complete System Setup*

Attached to the top of the platform are the ultrasonic array controller and the camera for the alignment procedure to the inspection stations. The ultrasonic array controller is used for firing and capturing the ultrasonic data from the roller probe attached to the flange of the LBR manipulator. The ultrasonic equipment is the same as described in Chapter 4: *Ultrasonic Setup* with the exception of the RGBD camera, the Zivid 2 M70 [144], a newer, smaller and lighter model that claims higher point precision than its predecessor at 55µm.

### 5.2.2. Software

The software side of the system is more involved and contains elements that are proprietary and others that are custom solutions. The integration and relationships between the various software algorithms are presented in Figure 5.2, providing a clear view of the overall solution.

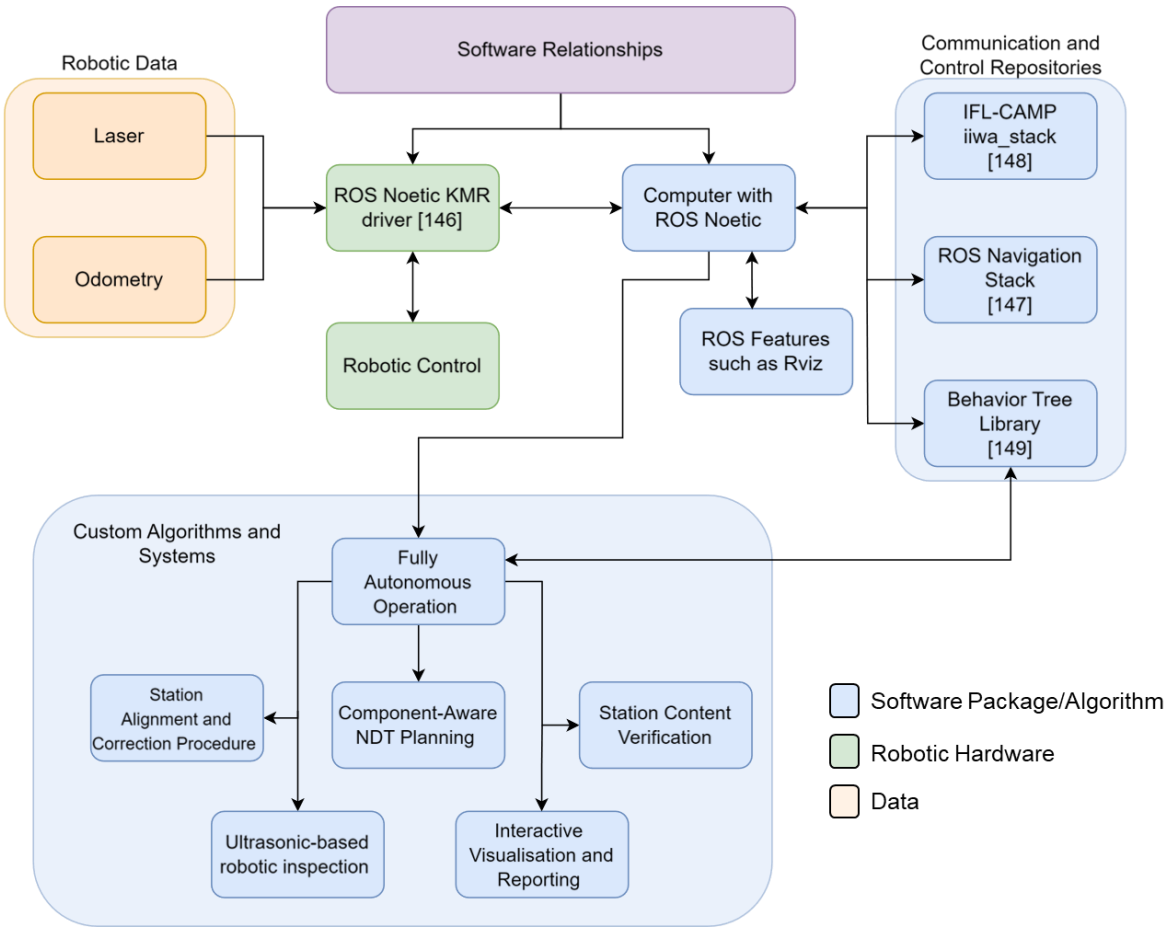


*Figure 5.2. Complete Solution Software Integration and Relationships*

The software was built upon the Robot Operating System (ROS) infrastructure[145], which was dictated by the fact that this work uses a proprietary ROS Noetic [146] driver for the KMR mobile base provided by KUKA, specific to the KMR iiwa platform. For communication and interaction with the robot, the same version was installed on a computer. This driver allowed access to the onboard laser scanners, odometry data, and the ability to control the mobile base.

The integration and communication with the base and manipulator were done using a custom combination of repositories using the ROS Navigation stack [147] and IFL-

CAMP's iiwa_stack [148]. The Behavior Tree Library [149] was used for the coordination of the various aspects and commands that linked the C++ aspects, such as control over the robot and capturing with the RGBD camera. Python was used for the overall control of the whole system, interacting with the C++ based behaviour trees, ultrasonic control, path planning, and final data processing.

The utilisation of the above-mentioned repositories enabled the integration into RViz, a 3D visualiser for ROS, which allowed for the visualisation of the KMR base, LBR iiwa manipulator, the mapping of the environment, live laser data, as well as live tracking of the robot's movements in its environment.

The other algorithms and packages of this work were developed using a mixture of C++ and Python, and are described below:

- **Fully Autonomous Operation** – Based on a custom decision tree to control the complete inspection process, without user intervention.
- **Component-Aware PAUT Planning** – Utilising the user input to best decide the ultrasonic focal laws required for optimal inspection.
- **Alignment and Correction Procedure** – Using a dual tag system and a mechanically fixed camera onboard the platform to align with the target stations.
- **Environment-Aware Inspection Logic** – Utilising various processing algorithms and decision-making to detect components, enabling the cancellation of jobs for false calls.

- **Ultrasonic-based Robotic Inspection** – Controlled with a new algorithm, with real-time ultrasonic feedback for better alignment and inspection, and better control with velocity-based force control operations.
- **Advanced Visualisation and Reporting** – Finishing the completely automated pipeline by presenting the operator with a report of ultrasonic parameters, station, and job information, as well as interactive C-scan and B-scan plots, with a 3D thresholding display of defects.

These systems are further explored and explained in the following Methods section.

## 5.3. Methods

### 5.3.1. Fully Autonomous Operation

The system operates independently from call-up to return, executing the complete inspection process without manual intervention. The decision tree was implemented in Python, incorporating specific components from modules written in both C++ and Python. This approach was adopted because certain modules were either more efficient or only feasible in one of the two languages. It also allowed for the retention of previously developed features, such as ultrasonic connectivity and path planning. The complete operation and decision-making are presented in Figure 5.3.

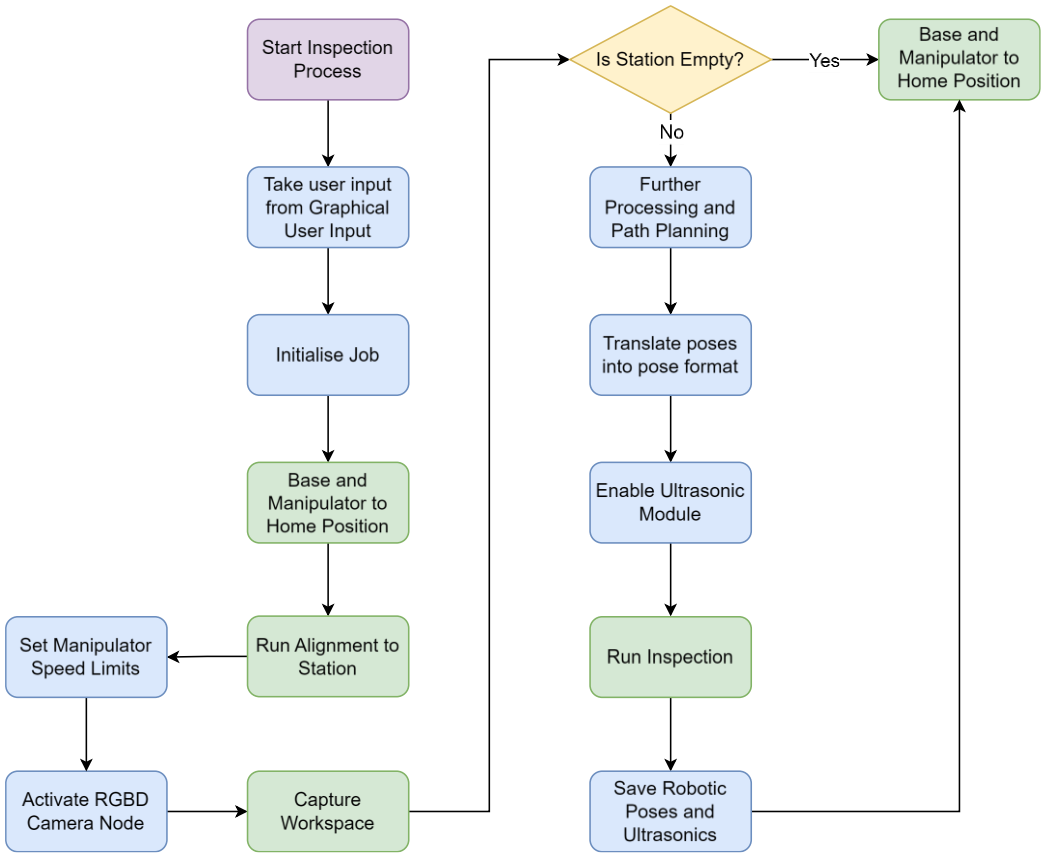


*Figure 5.3. Complete Inspection Operation*

The operation described in Figure 5.3 means that beside the initial user input for the job, no human intervention is required until the next job call. This introduces a freedom to the operator, focusing on more value-added roles, overseeing the inspection and then focusing on the captured PAUT data analysis and interpretation. The autonomous operation also incorporated fallback behaviours, such that in the event of a module or subsystem failure, the robot would return the manipulator and platform to their home positions. The rest of the modules in this operation are explained in the following sub-sections.

### 5.3.2. Component-Aware NDE Planning

The system makes use of a graphical user interface (GUI) to allow the user to prompt an inspection. For this, the GUI takes in 3 parameters: station number, material type, and thickness. The material type was used to decide which of the custom-calibrated and designed ultrasonic focal laws to use. For this work, calibrated focal laws were made for aluminium, CFRP, and steel. The GUI is shown in Figure 5.4.

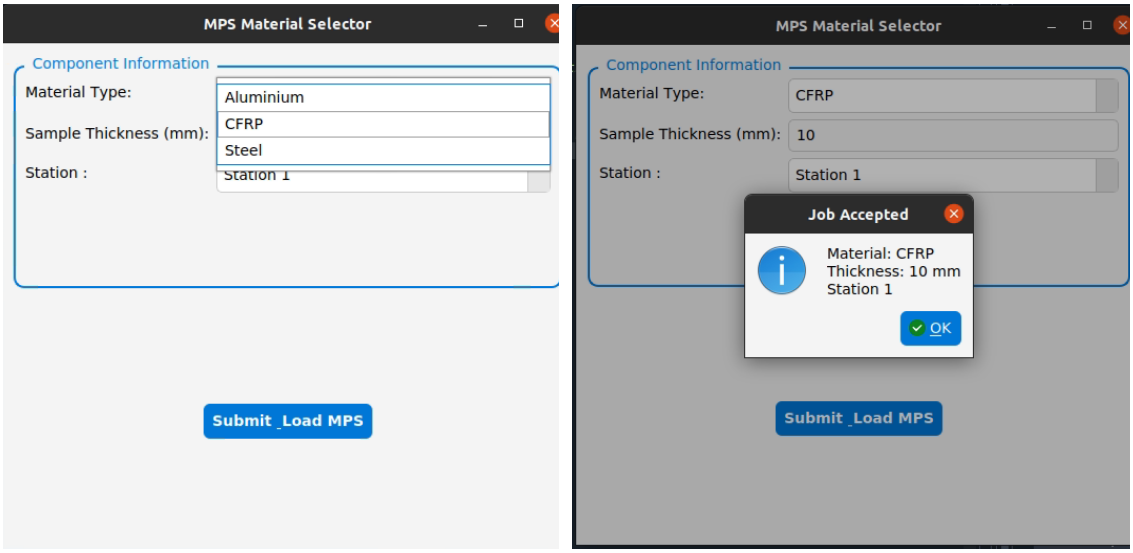


a) b)

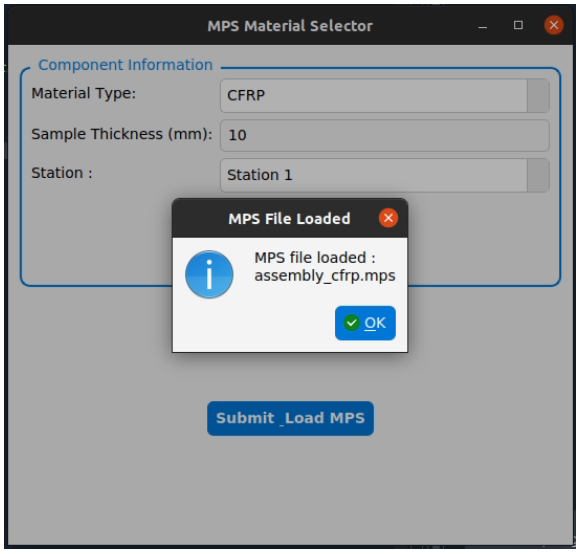


c)

*Figure 5.4. GUI Initialising Job and Ultrasonic Parameters. a) GUI Highlighting selection drop-down for material type, b) Job Submitted with parameters for CFRP, 10 mm thickness at Station 1, c) Displaying which ultrasonic focal laws file has been selected based on the inputs.*

For the custom ultrasonic focal laws, the calibration process for each material was done as described previously in Chapter 4: Ultrasonic Setup.

### 5.3.3. Station Alignment and Correction Procedure

This module aimed to locate and align with target stations within the manufacturing environment, where stations could be repositioned or incorrectly placed. As the environment was subject to frequent changes, reliance on a predefined map was not always the most effective solution for navigation.

To allow the mobile system to find and align itself with the target stations, the use of tags and a camera was a possible low-cost implementation. The problem with cheaper cameras and RGB cameras is that they can suffer from distortion [150]. The major distortions that

affect the usability of a camera for high-accuracy applications are radial distortion and tangential distortion.

The radial distortion causes straight lines to appear curved. Radial distortion becomes larger the farther points are from the centre of the image. Meaning that all the expected straight lines are bulged out. Similarly, tangential distortion occurs because the lens is not aligned perfectly parallel to the imaging plane. Therefore, there may be some areas in the image that look nearer than expected.

To overcome this issue, the RGB camera used was calibrated using OpenCV [151]. The OpenCV camera calibration algorithm made use of a chessboard pattern board to calibrate the camera and extract the camera matrix, intrinsics, extrinsics, and the distortion coefficients. Intrinsic parameters are specific to a camera, including information such as focal length and optical centres. The focal length and optical centres can be used to create a camera matrix to remove the distortion of the specific camera. The camera matrix is unique to a camera, so once calculated, it can be used multiple times on pictures and videos captured by the camera. Extrinsic parameters correspond to rotation and translation vectors, which translate a coordinate of a 3D point to a coordinate system.

The calibration process required a minimum of 10 captures of the chessboard from different orientations and positions. Once sufficient captures were made, the resultant camera parameters were returned, with the calibrated camera now able to capture all the internal corners of the chessboard pattern correctly. The results of the calibration procedure are presented in Table 5.1.

*Table 5.1. Camera calibration results*

| | |
|---|---|
| Camera Matrix<br><br>(Intrinsics) | $\begin{bmatrix} 645.40 & 0. & 312.15 \\ 0. & 645.64 & 233.37 \\ 0. & 0. & 1. \end{bmatrix}$ |
| Distortion Coefficients | $[0.043 \ -0.21 \ -0.0048 \ 0.0013 \ 0.35]$ |
| Reprojection Error | 0.2341 |

Tracking of tags was then possible once the camera parameters had been calculated. To do the tracking, the use of AprilTags was the chosen solution [152]. This was selected as it is a robust visual fiducial implementation that contains an identification (ID) code and is used for orientation and location. AprilTags are designed to be easily recognisable from any angle, under a wide range of lighting conditions, and even when partially covered or blurred, making them highly suitable for use in robotic applications. The two tag designs used in this work are presented in Figure 5.5.

a) b)

*Figure 5.5. AprilTag Designs, a) tag36h11 22, b) tag36h11 50*

Once an AprilTag has been captured, the image is converted to grayscale and lower resolution for faster processing. The algorithm then performs edge and shape detection, identifying high-contrast regions and grouping them into connected components. From these, quadrilateral shapes are isolated, as they represent potential tag candidates. Once a candidate is detected, the algorithm applies perspective correction to account for camera angle and distortion before decoding the black-and-white grid pattern within the tag's interior. This pattern is then translated into a unique numerical ID using error-correcting codes, allowing for reliable identification even in the presence of visual noise or partial occlusion. Finally, using the tag's known physical dimensions and the camera's calibration parameters, the system performs pose estimation to determine the tag's exact pose relative to the camera.

Using a custom configuration of OpenCV for capturing each frame and the AprilTags system for the detection, the distance from the camera to tags was found and measured as z, and the distance laterally was measured as x. The intention to use 2 tags was to allow

for the orientation of the station to be easily extractable, as well as the distance from the station to the robot. As demonstrated in Figure 5.6, the dual tags were used to estimate whether the base was parallel to the station.

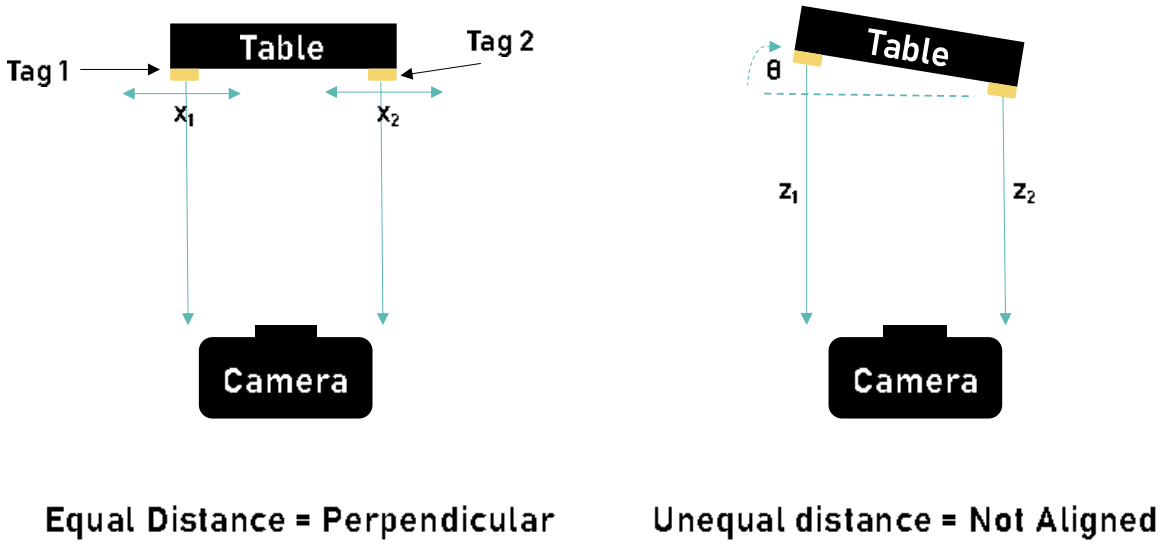


*Figure 5.6. Alignment of the table relative to the camera based on the tag system*

The angle of the robot relative to the table (θ) was the main controlling factor for driving the robot to the station. Using the two tags, the angle of the base relative to the station was established by finding the position of each tag. Subtracting the positions gave the vector between the tags. Using the x and z components, the angle was then found using arctan + 90 to get a value of 180° when the z distances between the robot and the table for both tags were the same. This is demonstrated in Equations (5.1)-(5.2), where $t_1$ represents the position of tag 1 and $t_2$ the position of tag 2.

$$v = t_2 - t_1 \tag{5.1}$$

$$\theta = degrees(arctan2(v_x, v_z)) + 90 \quad (5.2)$$

For the control aspect, tag 1 was made the lead tag for which the target distance would be measured against. Two main aspects within the control procedure mattered. The first being ensuring that the platform stayed parallel to the station on approach until the target distance was met. The second was ensuring that the sight of the tags was not lost until the distance and orientation were correctly met. For this reason, the following Algorithm 5.1 was developed to check if the tags were undetected for three or more frames, and to move in the direction of the tag until it was found again. For tag 1 that meant driving in +X, and -X for tag 2 .The reasoning for three or more frames before moving was to avoid cases in which the camera might not capture a frame properly, which would be interpreted as a missed tag, leading to sudden, unwanted movements. Three or more missed captures would confirm that the tag was indeed no longer in view and then prompt the correct subsequent decision.

```
Procedure UPDATE_TAG_COUNTERS(tags):
    tag1 ← find tag in tags with tag_id = 1
    tag2 ← find tag in tags with tag_id = 2

    if tag1 is not None then
        tag_1_seen_once ← True
        tag_1_counter ← 0
    else if tag_1_seen_once = True then
        tag_1_counter ← tag_1_counter + 1
    end if

    if tag2 is not None then
        tag_2_seen_once ← True
        tag_2_counter ← 0
    else if tag_2_seen_once = True then
        tag_2_counter ← tag_2_counter + 1
    end if

    if tag_2_counter ≥ 3 then
        print("Tag 2 lost — searching in −X direction")
        for i ← 1 to 50 do
            MOVE_BASE(linear_x = −0.005, linear_y = 0, angular_z = 0)
        end for
        return
    end if

    if tag_1_counter ≥ 3 then
        print("Tag 1 lost — searching in +X direction")
        for i ← 1 to 50 do
            MOVE_BASE_ONCE(linear_x = +0.005, linear_y = 0, angular_z = 0)
        end for
        return
    end if

End Procedure
```

*Algorithm 5.1. Decision-making for lost tags during the alignment procedure*

The lost tag detection procedure was the first in the code order to ensure that the main control logic could run without issue. In the cases where both tags were detected, the main control logic function would run, as demonstrated below in Algorithm 5.2.

The first step ensured that the lead tag, tag 1, was correctly identified, after which, if the distance was greater than the target distance of 135 mm from the station, the robot would move towards the station. The value of 135 mm was selected, as it positioned the robot close enough to the station to achieve optimal reach while avoiding activation of the platform's emergency stop from the laser sensors due to being too close to the station. During movement, the parallel alignment procedure was run, ensuring that the robot base was within 1° of the target 180°, which would mean it was parallel to the station. If not, then the base would rotate to make up for the misalignments.

```
Procedure CONTROL_TARGET_TAG(tag1, angle_deg):
    if tag1 is None then
        return
    end if

    (x_mm, z_mm) ← (tag1.pose_t.x × 1000, tag1.pose_t.z × 1000)
    if z_mm > 135 then
        # Approach target
        if angle_deg is defined and |angle_deg − 180| > 1.0 then
            # Rotate to align to 180°
            if angle_deg < 180 then
                rot_speed ← 0.03 if angle_deg < 170 else 0.01
            else
                rot_speed ← −0.03 if angle_deg > 190 else −0.01
            end if
            MOVE_BASE_ONCE(0, 0, rot_speed)

        else
            # Angle aligned → move along −Y axis
            speed ← −0.03 if z_mm > 150 else −0.008
            print("Z = ", z_mm, " mm — aligned, moving −Y")
            MOVE_BASE_ONCE(0, speed, 0)
        end if

    else
        # Target within Z threshold — fine alignment
        print("Target within Z threshold and aligned")

        if z_mm < 130 then
            MOVE_BASE_ONCE(0, +0.008, 0)
        end if

        if x_mm > 55 then
            speed ← −0.0083 if x_mm > 60 else −0.003
            MOVE_BASE_ONCE(speed, 0, 0)
        else if x_mm < 55 then
            speed ← +0.0083 if x_mm < 50 else +0.003
            MOVE_BASE_ONCE(speed, 0, 0)
        else if 54 ≤ x_mm ≤ 56 then
            STOP_BASE()
        end if
    end if
End Procedure
```

*Algorithm 5.2. Main control logic for alignment and base movement.*

If the angle was out by 10°+ on either side, the rotational adjustments were made at 0.03 $rads^{-1}$, otherwise adjustments were run at 0.01 $rads^{-1}$, to ensure finer control when nearer the target angle. Once alignment was within the acceptable range, the base continued its movement towards the station at a speed of 0.03 $ms^{-1}$ when further than 150 mm from the target. When closer than 150 mm, the speed reduced to 0.008 $ms^{-1}$. This continued until the robot reached the target 135 mm distance from the station, which then triggered the last stage of fine control. During the last stage of the procedure, the distance from z was checked to ensure that the base was not closer than the intended 135 mm. Once corrected, the final alignment in x was validated. The check ensured that the x value of the target tag was at 55 mm ± 1 mm, relative to the camera frame. Once within the target distances for both z and x, the tag alignment procedure ended. Figure 5.7 illustrates the camera system with tags on the target station. In this setup, the camera was mechanically calibrated and securely mounted onto the robot base.


*Figure 5.7. KMR iiwa platform with RGB camera and tags on the target station*

### 5.3.3.1. Alignment Validation

To validate the performance of the alignment procedure, the Leica Absolute Laser Tracker AT901 [109] was used to track the movements of the KMR. The tracker capable of 10 µm precision within a 160m$^3$ volume used its three DoF capabilities to track at different heights and angles. The KMR was taught a home position, using its proprietary variation of Simultaneous Localisation and Mapping (SLAM) [115], in the middle of the laboratory workspace. The environment was busy and dynamic with people moving near the workspace. The target station was placed in a fixed position with its corner positions mechanically aligned and measured with the Leica. The setup is shown in Figure 5.8.

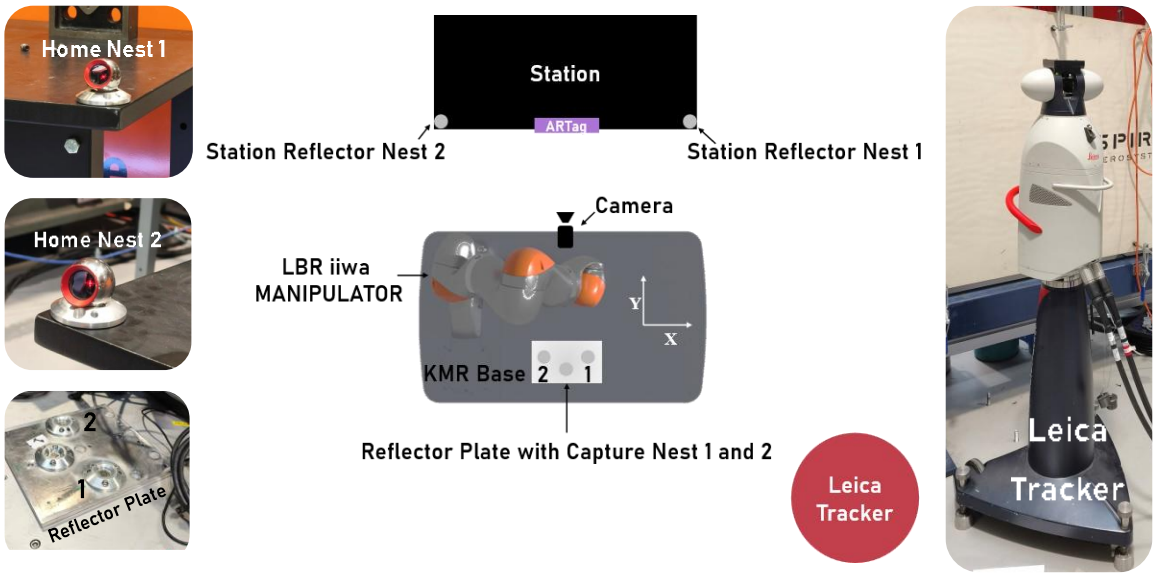


*Figure 5.8. Alignment Validation Experimental Setup*

The reflector plate had three slots for reflector nests, but it was deemed unnecessary to capture all 3 positions when the interest was to find repeatability and the angle of the platform relative to the station, requiring only two position values.

Captures of the home positions were carried out once, at the start of the experiment. The validation was carried out by repeating measurements at the taught home position and again once the alignment procedure was completed. The alignment procedure was run thirty times in accordance with the central limit theorem (CLT) [153]. Learning from the previous experimental work in Chapter 3, a larger dataset was acquired to get a better non-biased view of the data. A larger sample size helped to decrease the standard error and give a more precise estimate of the population mean and spread of data [154].

Each run consisted of 4 captures, capture 1 and 2 on the KMR base, as shown in Figure 5.8, at both the home position and once the alignment procedure was completed. Since all captures were done relative to the Leica tracker, the positions needed to be transformed relative to the station itself to validate performance. Station Nest 1 was used as the origin, and all the respective points were transformed relative to this new origin. Equations (5.3) and (5.4) show the calculation of the angle between the 2 station positions, by applying *arctan2* to the resultant vector between the positions. In Equation (5.3), $S_1$ represents the position of Station 1 and $S_2$ the position of Station 2.

$$v = S_1 - S_2 \tag{5.3}$$

$$\theta = degrees(arctan2(v_y, v_x)) \tag{5.4}$$

Equation (5.5) shows the calculation of the resultant transformation matrix between the two positions used to transform all other points relative to the station itself. Equation (5.6) describes the transformation of the secondary station position, subtracting the origin position and multiplying by the transformation matrix. The last of the transformations is shown Equation (5.7), transforming both the table-aligned positions and home positions in the same way as the second station point. The value of station one then becomes (0,0).

$$R = \begin{bmatrix} \cos(\theta), -\sin(\theta) \\ \sin(\theta), \cos(\theta) \end{bmatrix} \tag{5.5}$$

$$S_2' = (S_2 - S_1) \cdot R \tag{5.6}$$

T represents the table position and H the home position. The equation remains the same for both positions of the table and home.

$$T' = (T - S_1) \cdot R$$

$$H' = (H - S_1) \cdot R \tag{5.7}$$

The angle of the KMR base at both home and aligned was calculated with the relative positions using Equation (5.4). The target angle would be ±180°, meaning that the base would be parallel to the station. The reason for ±180° rather than just +180° is that angles are centred around ±180°, which are adjacent in circular space, illustrated best in Figure 5.9.

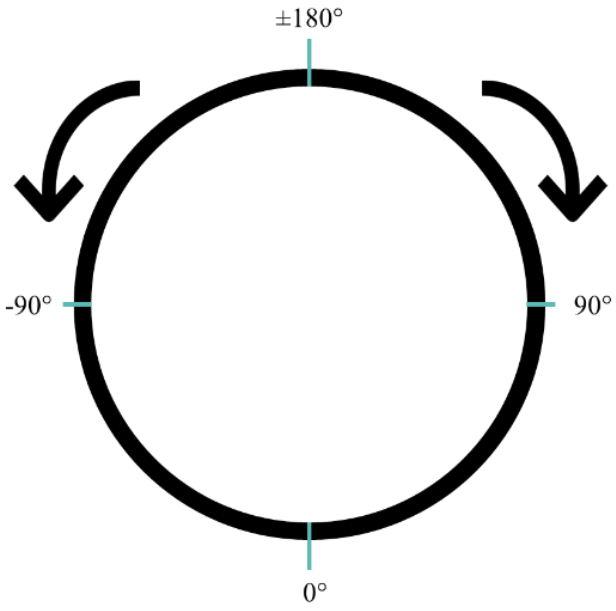


*Figure 5.9. Visual of angles in circular space*

The circular mean was used as it provided a better representation of the average orientation. The normal mean was unsuitable in this context, as it could produce misleading results when angles crossed the ±180° boundary — for example, averaging 170° and -170° would incorrectly yield 0° using a normal mean, whereas the circular mean would correctly give ±180°. For all thirty runs, the mean circular angle in degrees was calculated using Equation (5.8), where $\overline{\theta} = Circular\ Mean$.

$$\overline{\theta} = arctan2\left(\frac{1}{n}\sum \sin(\theta_i), \frac{1}{n}\sum \cos(\theta_i)\right) \tag{5.8}$$

The circular SD is calculated using Equations (5.9) and (5.10). In circular statistics, the circular standard deviation measures how tightly a set of angles is clustered around their

circular mean. Unlike linear data, angles wrap around, so traditional standard deviation, like traditional mean, was not applicable. Equation (5.9) calculates the mean resultant length. *L* ranges from 0 to 1, where 0 implies angles were widely spread (high variability) and a value of 1 means angles were tightly clustered (low variability).

$$\mathrm{L} = \sqrt{\left(\frac{1}{n}\sum \cos(\theta_i)\right)^2 + \left(\frac{1}{n}\sum \sin(\theta_i)\right)^2} \tag{5.9}$$

$$\sigma = \sqrt{-2\ln(L)} \tag{5.10}$$

Equation (5.10) was then used to transform that concentration into a standard deviation in radians, which was then transformed into degrees. The results of the thirty runs have been summarised in Table 5.2.

*Table 5.2. Alignment validation results*

| Metric | Aligned Position Vision-based Alignment | Home Position SLAM-Based Alignment | Percentage Difference (%) |
|---|---|---|---|
| **Mean Circular Angle (°)** | 179.96 | -177.71 | 1.28 |
| **Circular Std Dev (°)** | 0.20 | 0.77 | 285.0 |
| **Capture 1 X Std Dev (mm)** | 3.13 | 13.41 | 328.1 |
| **Capture 1 Y Std Dev (mm)** | 1.11 | 12.24 | 1002.7 |
| **Capture 2 X Std Dev (mm)** | 3.13 | 13.34 | 327.4 |
| **Capture 2 Y Std Dev (mm)** | 0.90 | 13.82 | 1435.6 |

Table 5.2 above shows the standard deviation for both the aligned and home position values. These values show that the alignment algorithm has been capable of repeatedly aligning the base to the table within a small tolerance of <3.2 mm in the x direction and <1.2 mm in the y direction. As mentioned in Chapter 3, the required accuracy for precise PAUT inspections is 0.5 mm, however this process allows for the KMR base to be aligned to the target station even in a noisy environment, after which the station itself would be captured using the 3D camera for the next stage of the inspection compensating for the larger tolerance.

The busy environment did, however, mean that the standard deviation for the SLAM-based home positions suffered in the repeatability, with standard deviations of more than 13 mm in both the x and y directions. The deviation of the circular angle was also almost

three times larger, showing that even with the more inconsistent home positions, the platform could still align itself to the station as required.

Another parameter that was checked was the error, defined as the difference between a value and the ground truth. The first run was assumed to be the initial ground truth to allow for a comparison of the platform's performance. The results presented in Table 5.3 are the mean differences between each run position compared to the ground truth.

*Table 5.3. Mean Errors for Alignment Validation*

| **Mean Error (mm)** | **Aligned Position Vision-based Alignment** | **Home Position SLAM-Based Alignment** | Percentage Difference (%) |
|---|---|---|---|
| **Capture 1 X** | 2.73 | 25.59 | 837.4 |
| **Capture 1 Y** | 2.04 | 3.99 | 95.6 |
| **Capture 2 X** | 2.74 | 25.50 | 830.7 |
| **Capture 2 Y** | 1.45 | 6.06 | 317.2 |

The results of Table 5.3 showed that the Vision-based Alignment had a lower error, as compared to the SLAM-based, indicating a higher positional accuracy. The difference column quantifies how much more error SLAM-based alignment introduced compared to the vision-based method. The larger impact was seen in the X error, where the SLAM method introduced over 800% difference in the error as compared to the Vision-based Alignment. The visual representation of the positions is presented in Figure 5.10.

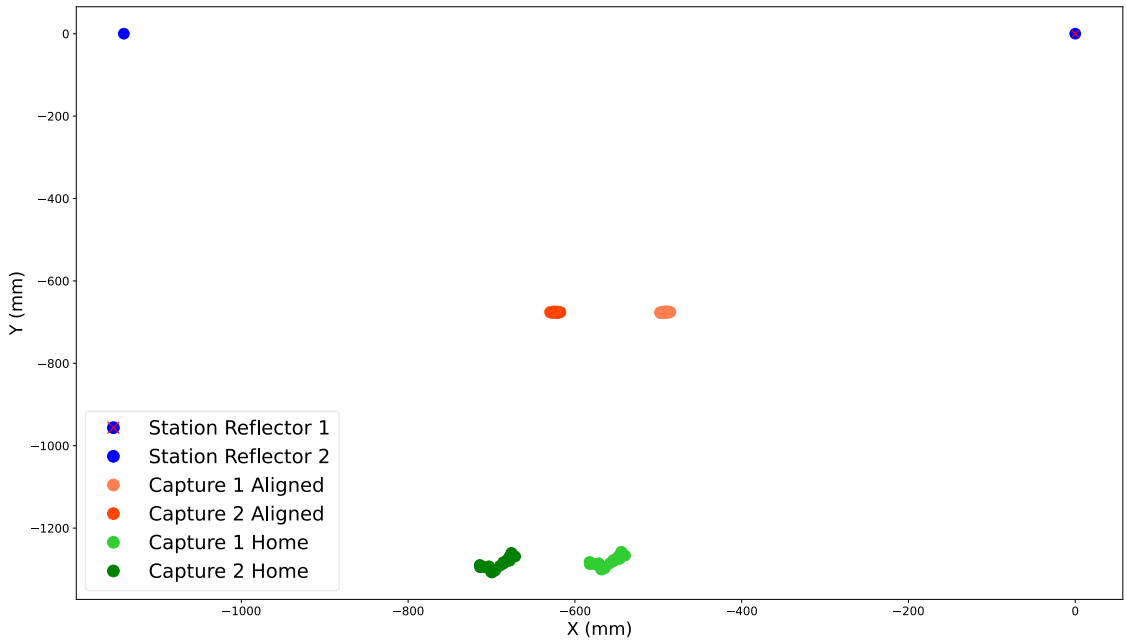


*Figure 5.10. Alignment Validation Positional Results*

The plot of Figure 5.10 shows the compactness of the aligned captures, and the variation visible for the SLAM-based home positions (green), highlighted in the results of Table 5.2 and Table 5.3.

### 5.3.4. Station Content Verification

This module focused on verifying the contents of each station to determine whether a component was present. Empty stations were identified through the analysis and exclusion of in-plane points corresponding to the workstation surface. If the remaining residual points fell below a predefined threshold, the station was classified as empty; otherwise, it was considered to contain a component, allowing the inspection process to continue.

The robot was taught to move to 6 different poses, acquiring RGBD captures to best represent the workspace. The RGBD camera captured the workspace using structured light

to get a point cloud representation of the workspace. The behaviour tree logic for this section is presented as Algorithm 5.3.

```
Procedure ARM_TO_SCAN_SEQUENCE()

    # === Initialization ===
    CALL SET_MANIPULATOR_LIMITS()

    # === Define scan poses ===
    arm_scan_loc1 ← Pose_1
    arm_scan_loc2 ← Pose_2
    arm_scan_loc3 ← Pose_3
    arm_scan_loc4 ← Pose_4
    arm_scan_loc5 ← Pose_5
    arm_scan_loc6 ← Pose_6

    # === Sequential scanning ===
    For each pose in [arm_scan_loc1, arm_scan_loc2, arm_scan_loc3,
                      arm_scan_loc4, arm_scan_loc5, arm_scan_loc6] do

        # Move the arm to the current pose
        CALL MOVE_ARM_JOINT_SPACE(pose)

        # Capture and save image/data at the current position
        CALL CAPTURE_SAVE()

    end for

    # === Final step ===
    CALL ARM_TO_DRIVE_POSITION()

End Procedure
```

*Algorithm 5.3. Workspace capture behaviour tree*

The behaviour tree was programmed to load the six pre-taught poses and execute them in a sequential loop. At each pose, the robot captured the workspace using the RGBD camera, verified that the data was saved, and then proceeded to the next position. Upon completing the sequence, the manipulator returned to its home position. Once the captures were

completed, the next stage was the processing and stitching of the six 3D captures. Using the calculated hand-eye calibration method for the camera to the manipulator, described previously in Chapter 4: Robotic Transformation, and the manipulator pose values, the scans could be merged. From each of the robot poses, a transformation matrix was created, which was then multiplied by the resultant hand-eye calibration matrix [134]. This new matrix was then used to transform all the points within each of their respective scans. The resultant capture is shown in Figure 5.11 a) of the empty station.

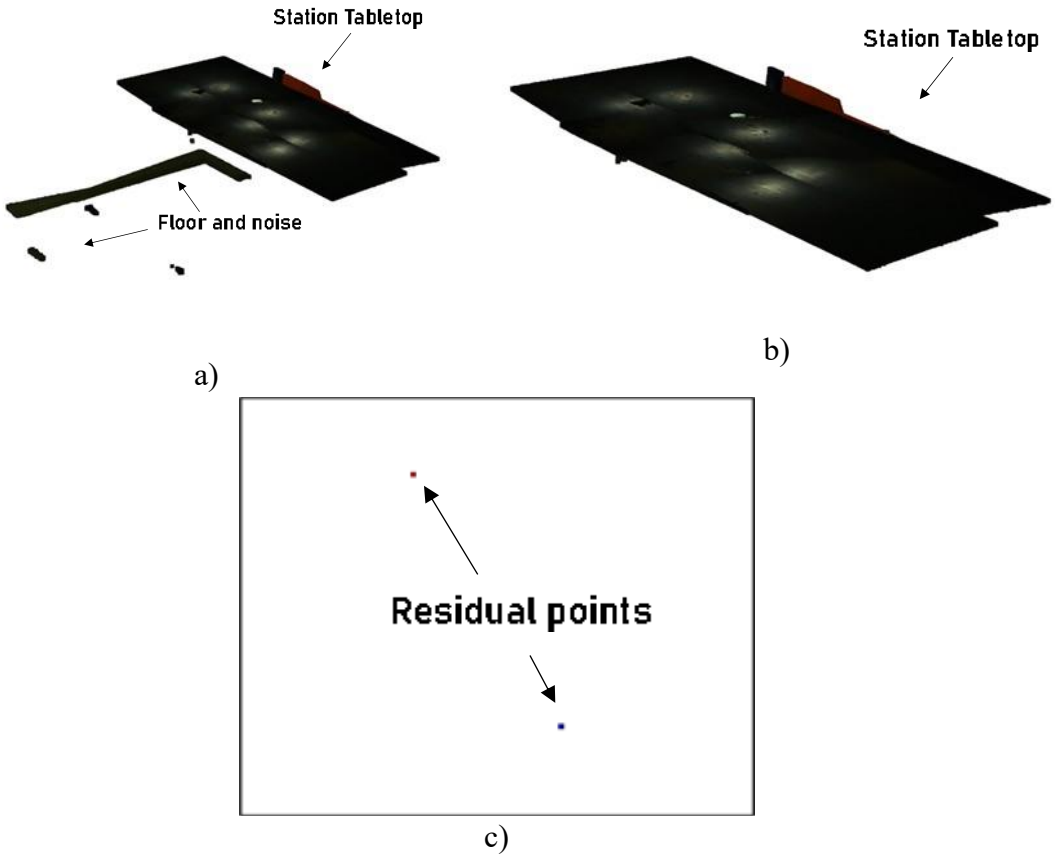


*Figure 5.11. Workspace capture processing for empty station example, a) Full Merged station workspace capture, b) Cleaned station workspace capture, c) Resultant non-station points*

With the complete workspace capture, the next stage of processing was filtering. The first part of filtering was removing any points below the height of the station. This gave the output shown in Figure 5.11 b). The next filtering step was to remove all points that landed on the plane of the station. The plane equation of the station was calculated using a Principal Component Analysis (PCA)[155] method that uses the eigenvectors to calculate the plane.

The plane normal corresponds to the eigenvector with the smallest eigenvalue, as that is the direction with the least variance. The vector values of the normal corresponded to a, b and c of the plane equation shown in Equation (5.11). The value of d was calculated using the negative dot product of the normal vector and a representative point on the plane, which is usually the centroid. These calculations are presented in Equation (5.12), with the final plane equation as Equation (5.13).

$$ax + by + cz + d = 0 \tag{5.11}$$

can be rewritten as

$$n \cdot r + d = 0 \tag{5.12}$$

Where n=(a,b,c) is the normal vector to the plane and r=(x,y,z) is a point on the plane.

$$-0.0097527x + 0.0009430y + 0.9999520z - 23.0945935 = 0 \tag{5.13}$$

With the plane equation, any points that were on or below the plane were removed within a threshold of 3mm to account for slight light reflections from the structural light captures.

At this stage, all points that were further than the length of the station were also removed. What remained after the filtering determined the next stage, and whether the path planning would be triggered or the return to home procedure would be run.

The complete merged scans contained several million points, and even after filtering, the remaining points were over several hundred thousand; therefore, a threshold was set to check whether the remaining points were deemed enough to count as an object or as residual noise.

If the threshold was not triggered, then the next action was to trigger the return to home procedure, in which the base moved back to its SLAM-based taught position and awaited further instructions, returning this decision: **Station Empty, Returning Back.**

The decision to check the station for an object before inspection was to ensure that no false calls could be made that could damage the equipment or waste resources doing an inspection on a non-existent component. In the instance that the threshold for sufficient points was triggered, then the following was returned: **Component Detected. Continuing Inspection.**

This then triggered the next aspect of filtering to ensure only one component was being inspected and all other noise or clusters of points were removed. The resultant component points were then passed to the path planning algorithm originally designed and described in Chapter 4: Flexible Path Rasterisation.

### 5.3.5. Ultrasonic-based robotic inspection

After the path planning returned a list of poses, the inspection was triggered. The inspection was controlled using a custom behaviour tree. The tree began by initialising the required parameters for the inspection. These include reading and splitting the target poses, setting the target force, initialising the connection to the ultrasonic capturing algorithm and moving the manipulator above the first target pose. As introduced in Chapter 4: Ultrasonic Setup, the orientation and position of the manipulator for the UT inspection are critical to ensuring proper coupling and accurate data capture. The simplified behaviour tree is presented in Figure 5.12.

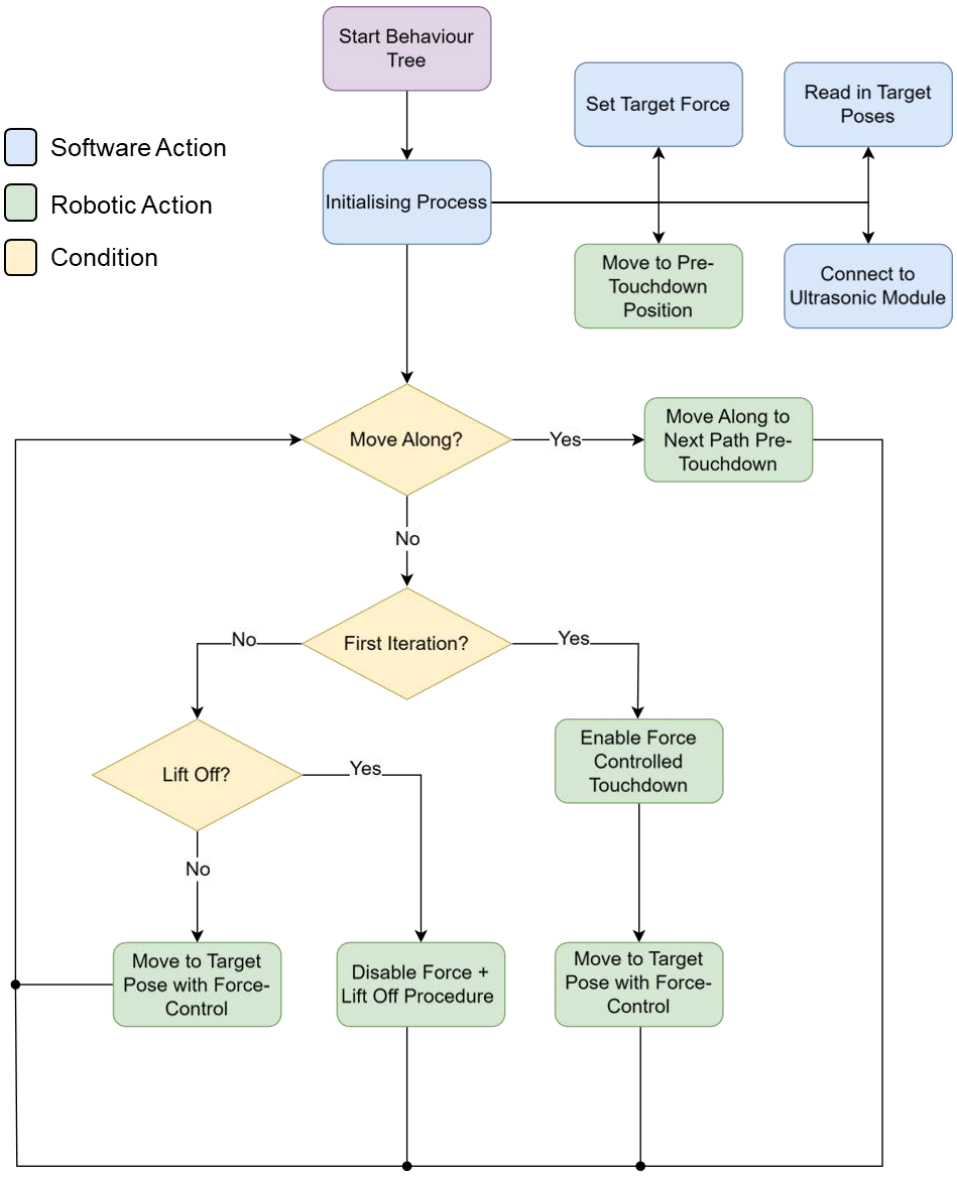


*Figure 5.12. Inspection process simplified behaviour tree*

After initialisation shown in Figure 5.12, the behaviour tree sequentially executed the defined conditions. On the first iteration, the custom force-descent node commanded the robot to approach the component by moving along the Z-axis until a target force was reached, minimising collision risk. Once contact was established, the ultrasonic capture algorithm was activated, and the manipulator followed the pre-estimated raster scan path,

superimposing Z-coordinate adjustments provided by the force module to maintain consistent coupling. Subsequent poses were evaluated for z-axis differences to determine whether a lift-off was required; if so, the ultrasonic capture was disabled, and the move-along command executed Cartesian motion to the next pose. The sequence repeated for all paths, after which the manipulator and base returned to their home positions.

Behaviour trees were used to structure the inspection logic. The tree allowed a hierarchical set of actions to be broken-down into reusable behaviours, making it simpler to maintain inspection approaches.

For safe force-contact management, the tree continuously monitored force, position, and coupling conditions using dedicated safety condition nodes. Threshold violations were detected immediately, and controlled transitions between motions were enforced, reducing the risk of probe or component damage.

Fallback nodes were used to handle faults and enable recovery. If a failure occurred, the system reverted to safe behaviours, such as retracting, re-aligning, or returning to a home position, without halting the inspection sequence. This improved robustness during autonomous operation and long-duration inspections.

#### 5.3.5.1. Ultrasonic-based probe orientation corrections

To improve upon the inspection capabilities presented in Chapter 4: Force-controlled Phased Array UT Inspection., this work employed real-time ultrasonic data to enable the most optimal inspection of the target samples, to adjust the roll of the manipulator (Figure 4.4 a)). From the ultrasonic data, the first procedure involved extracting the front wall of

the sample. A search window was defined from the start of the ultrasonic data, within which the maximum amplitude was identified for each A-scan. This process yielded a Time of Flight (ToF) value, representing the arrival time of the front-wall echo at each A-scan position. The extraction process is illustrated Figure 5.13, with the initial B-scan in Figure 5.13 a). The extraction of the ToF values are highlighted by the red dots along the front wall of Figure 5.13 b), with the best fit line and the extracted angle shown in Figure 5.13 c).

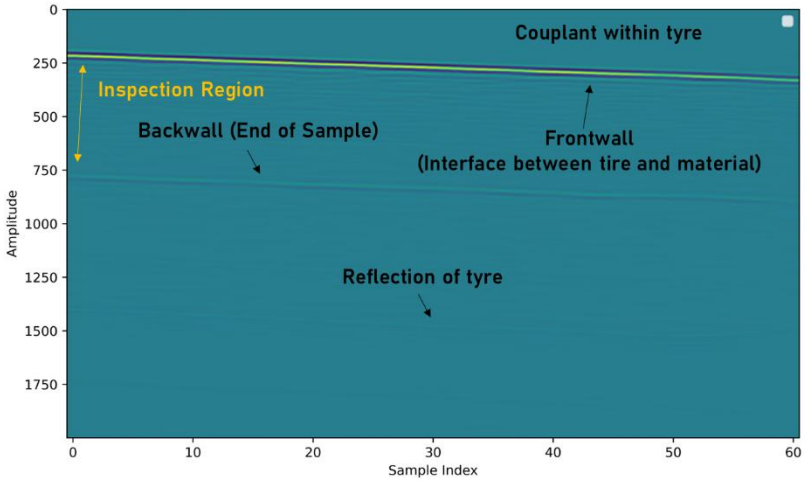


a)

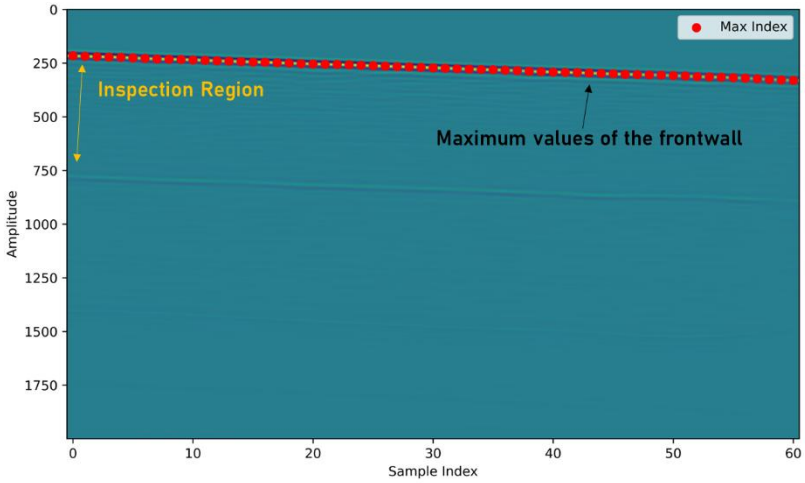


b)

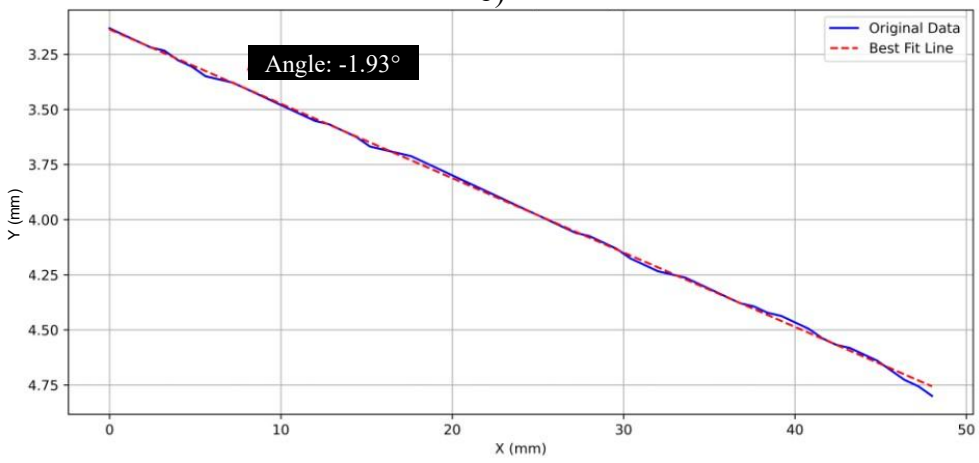


c)

*Figure 5.13. Sample B-scan front wall Angle Evaluation, a) B-Scan, b) B-scan highlighting maximum amplitude values at corresponding ToF positions, c) Extracted ToF positions, with best fit line corresponding to angle of front wall*

Using this array of ToF indices, the data was transformed to allow the extraction of the front wall angle. The x-axis, representing the A-scans, was multiplied by the element pitch of the array, which for this array was 0.8 mm. The ToF values were then transformed using the procedure described in Equation (4.9), returning values in millimetres.

With the values now converted into millimetres, the mathematical operation of a linear regression was performed, using the SciPy library [156]. A straight line was fitted to the extracted points to provide the best representation of the front-wall angle. The line was transformed using the inverse tangent to return the corresponding angle.

A calibration procedure was then run to associate the angle of the front wall with the appropriate rotation about x (roll) for the robot. Correction of the front wall was performed continuously during the inspection, with the maximum angular speed limited to 0.03 $rads^{-1}$. The correction procedure is illustrated in Figure 5.14, showing the progression of front-wall alignment. The initial front wall after touchdown is shown in Figure 5.14 (a), with visible corrections by the fifth B-scan in Figure 5.14 (c), and full alignment achieved by the tenth B-scan in Figure 5.14 (e). The front wall remained aligned at the fourteenth B-scan and maintained this alignment throughout the remainder of the inspection.

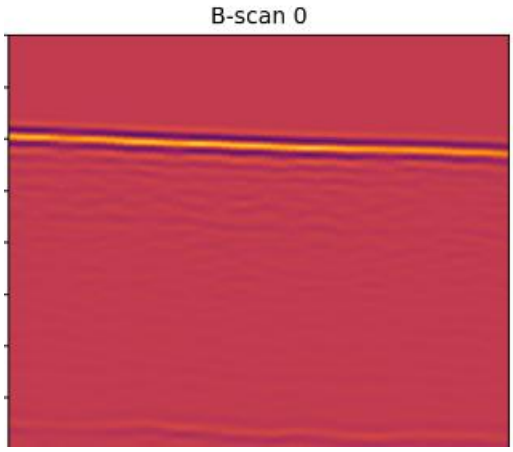


a)

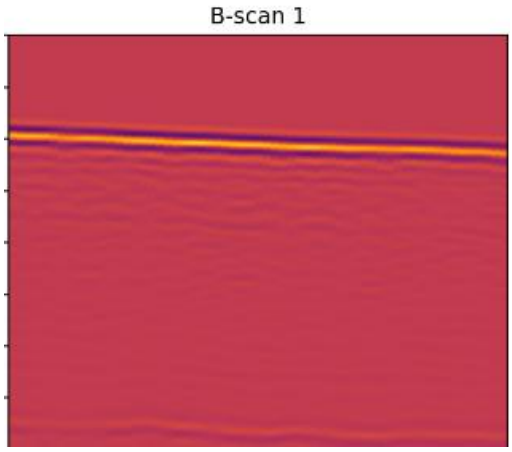


b)

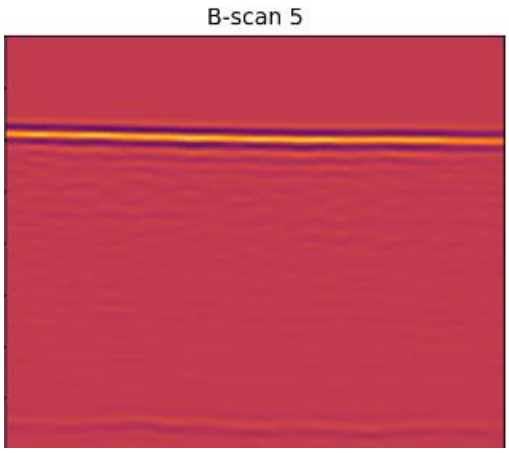


c)

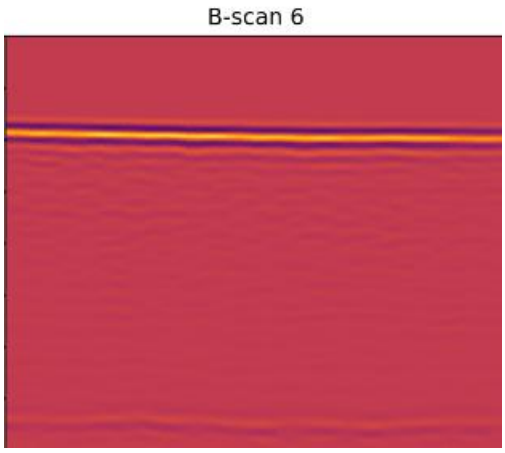


d)

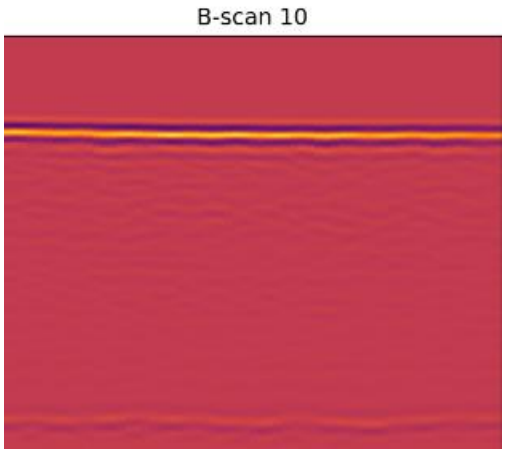


e)

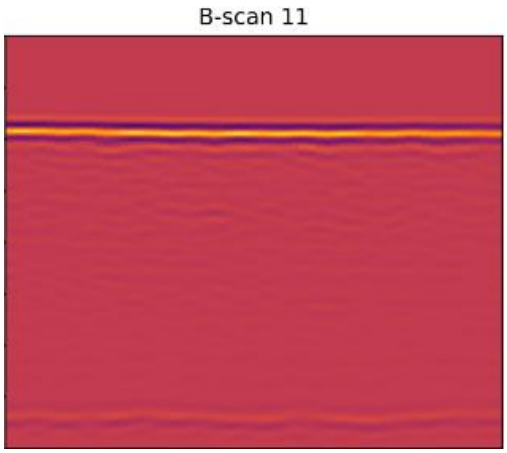


f)

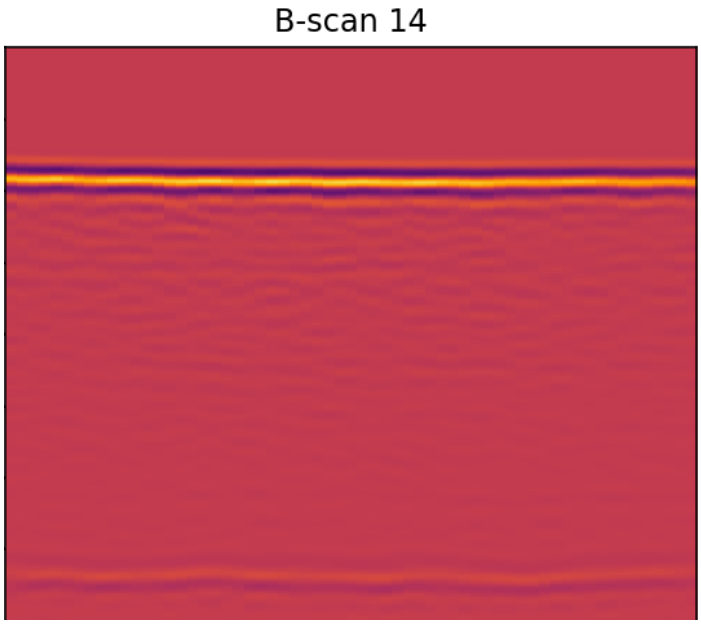


g)

*Figure 5.14. Front wall visual of correction during inspection process, a) Initial B-Scan with most inclination, b) First B-Scan, c) Fifth B-Scan with inclination reduction, d) Sixth B-Scan with similar inclination reduction, e) Tenth B-Scan with aligned front wall, f) Eleventh B-Scan with aligned front wall, g) Fourteenth B-Scan with aligned front wall.*

As shown in Figure 5.14, the alignment was observed to stabilise for a significant incline upon touchdown by the tenth B-scan, corresponding to approximately 8 mm into the scan. The adjustment could be accelerated by increasing the correction speed; however, the chosen speed was considered appropriate, as higher speeds risked causing over-corrections. The alignment procedure was executed with scans acquired at a frequency of 10 Hz.

#### 5.3.5.2. Implementation of Force-based Motions

The force-based control was also refined in this work. Rather than executing commands through a purely force-based Cartesian control, velocity-based commands were employed

to incorporate real-time inputs from the corrections calculated and described in Section 5.3.5.1. The new velocity-based control method read the current Cartesian position and, similarly to the base approach, adjusted the speed according to the distance from the target. When the manipulator was further from the target, higher speeds were used, while the speed was reduced as the end-effector approached the target pose. The inspection speed of the system was capped at 4.5 $mms^{-1}$, which was enforced as a maximum but could be reduced when necessary.

The use of velocity-based control also improved force regulation, maintaining the force within a target threshold of ±1 N. In instances where force readings increased too rapidly, the manipulator triggered a custom emergency stop module. This module allowed the manipulator to move away from the inspection normal, reducing the applied force and preventing the activation of a hardware stop.

During force-based movement, the ultrasonic capturing algorithm operated simultaneously, acquiring a B-scan every 0.8 mm. The algorithm ran only during force-based movements and was disabled once the end of each path was reached. Each ultrasonic capture was additionally encoded with the robotic position at the moment of acquisition, enabling precise correlation between positional and ultrasonic data.

### 5.3.6. Interactive Visualisation and Reporting

Post-inspection, the system generated a report of each inspection, presenting the details of the inspection, station location, time of job, material type, ultrasonic properties used and ultrasonic plots. The report generation was created as a web-based report that allowed the

user to interact with the ultrasonic plots for better visualisation. The full report is displayed in Appendix E – Full Generated Report with its various interactive aspects. The web-based report presents the focal law table that highlights parameters selected for the operation, as well as the station and time of the job call. The interactive ultrasonic plots are shown in Figure 5.15, broken down into the Amplitude C-scan and B-scan (a), and the ToF C-Scan (b).

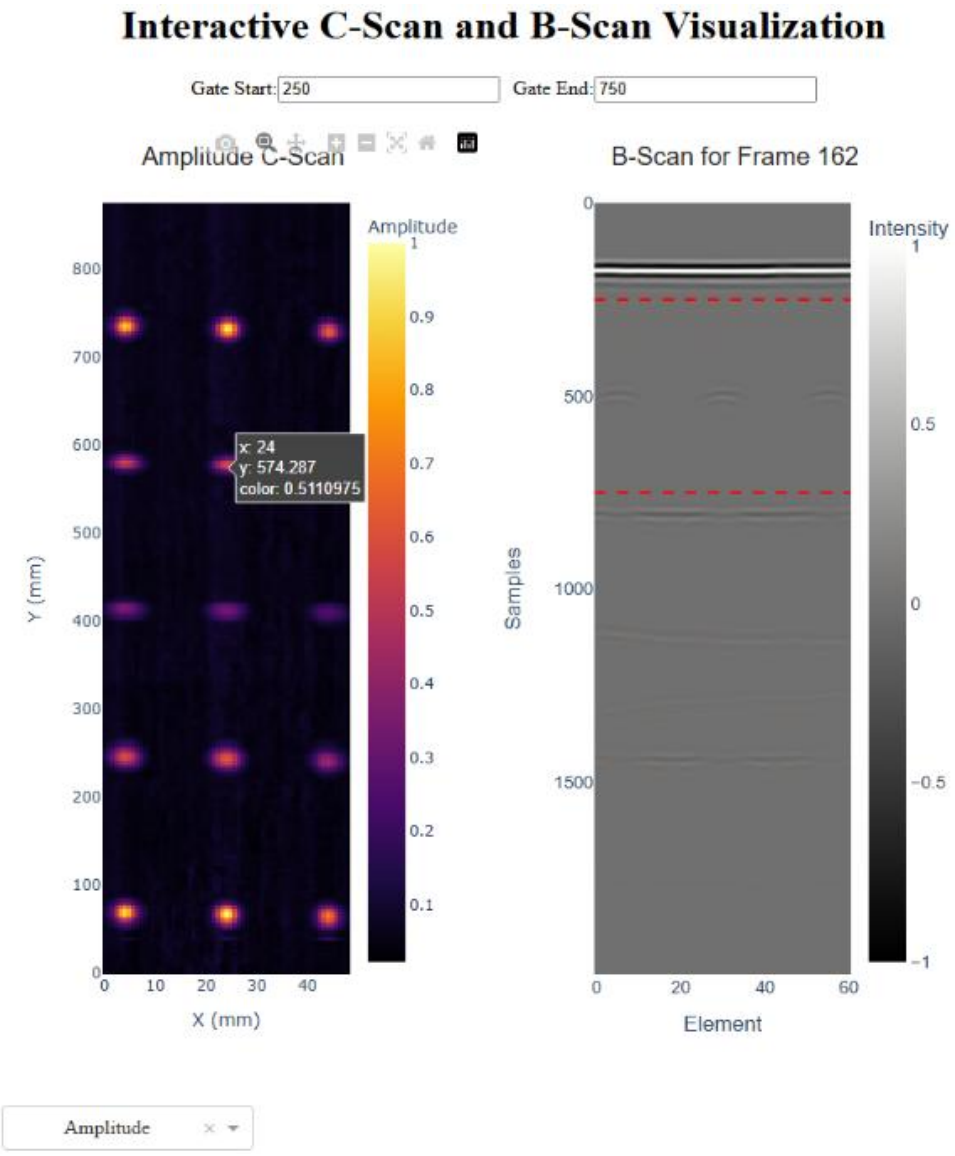


a)

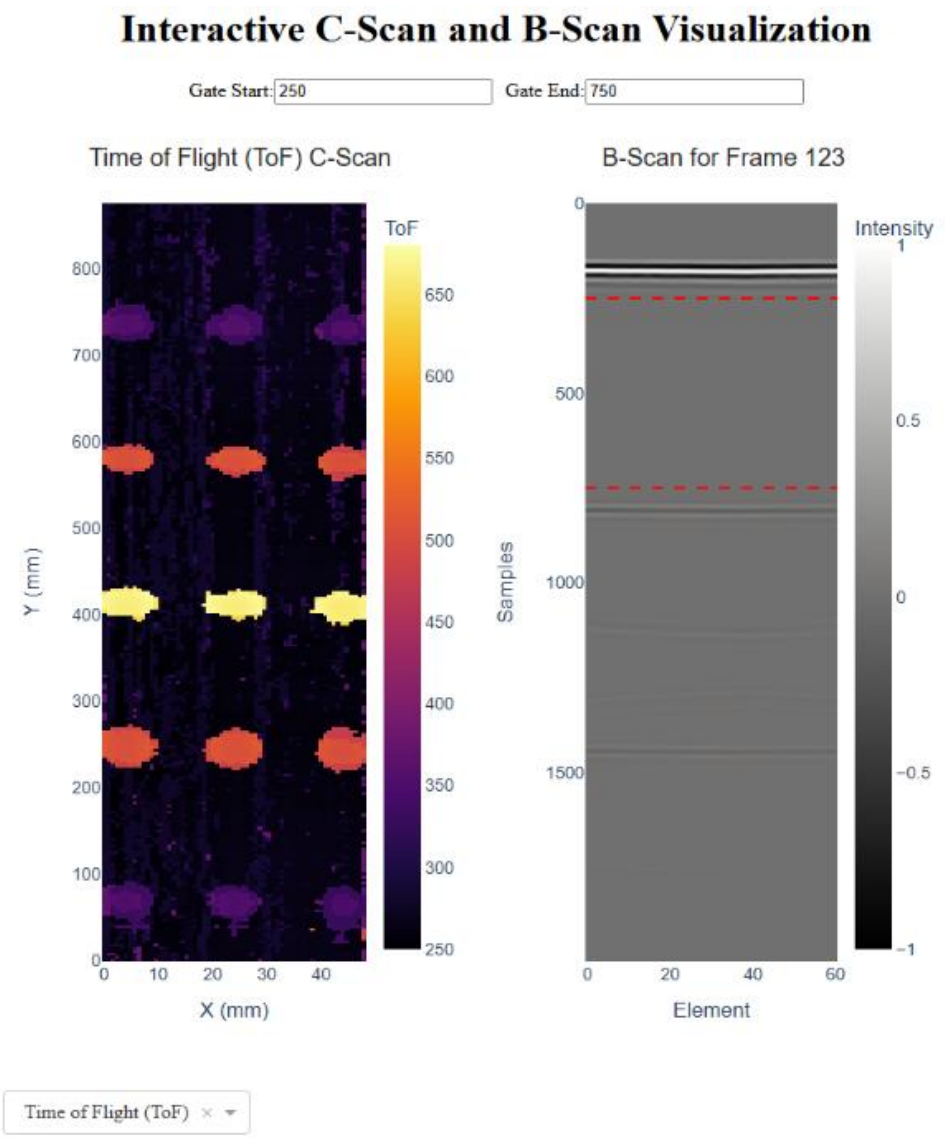


b)

*Figure 5.15. Interactive report generated from results of inspection, a) Report highlighting C-scan cursor adjusting displayed B-scan, b) Report displaying the ToF scan from drop-down menu.*

The report features interactive functionality, allowing the operator to select sections of the C-scans and view the corresponding B-scans. The red lines on the B-scans indicate the gates used for the C-scan, enabling clear identification of the front and back walls and the regions of interest for comprehensive sample inspection. Gating is performed in real time;

any adjustments to the gate values are immediately reflected in the C-scan display. The plots can be exported for use elsewhere once the operator has reviewed and verified the report.

The ToF map, shown in Figure 5.15 b), provides additional information regarding the inspection and offers an alternative perspective for the operator. The ToF map enables the operator to visualise defects differently and to examine the precise timing of signal responses from artefacts within the data. This representation can provide further insight into the depth of specific reflectors, with longer response times indicating artefacts or defects located in deeper regions of the inspected component.

The last part of the report generated is the 3D Defect plot. This process used the same gating parameters as those used for the C-scan and ToF plots, isolating only the regions of interest. The strongest amplitude signals within these regions were retained and subsequently converted from indices to spatial coordinates using the ultrasonic parameters of the material. A better visual of this plot is shown in Figure 5.16.

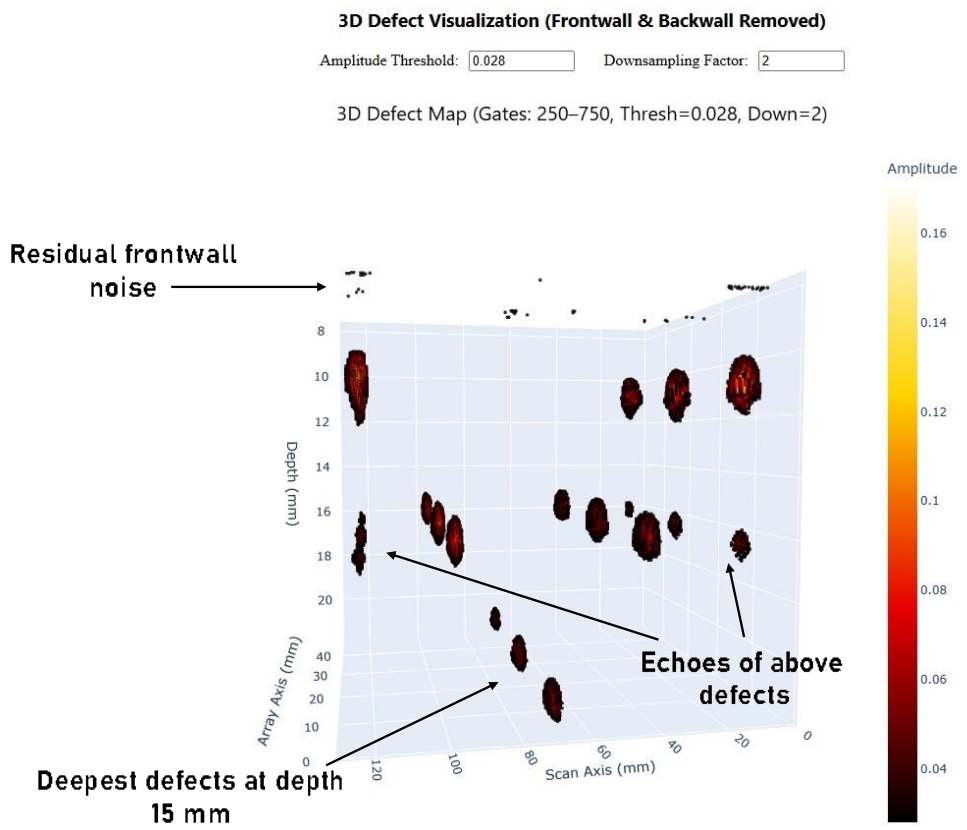


*Figure 5.16. 3D Defect Visual of the inspected sample from the Report Generated*

As indicated in Figure 5.16, an additional row of highlighted defects is visible beneath the initial defects. These secondary reflections correspond to echoes of the primary defects, exhibiting lower energy than the original reflections. The energy reduction explains why such secondary reflections are not observed in subsequent rows.

# 5.4. Experimental Validation and Results

## 5.4.1. Test Setup

Validation was performed on three calibration samples: Sample A and Sample B were the same as those introduced in Chapter 4: Inspected Samples, while the third sample, Sample

D was an additional CFRP component containing 25 defects. Similar to Sample A, Sample D measured 254.0 × 254.0 × 8.6 mm (width × length × thickness) and was manufactured by Spirit AeroSystems, UK according to aerospace industry calibration standards. It was constructed from woven carbon fibre fabric sheets and Cycom 890 resin in accordance with the BAPS 260 standard.

Flat-bottomed holes (FBHs) were introduced into Sample D to the same depths as those in Sample A, with additional defect sizes of 4.0 mm and 7.0 mm, resulting in a total of 25 FBHs. The FBHs maintained the same manufacturing tolerances as the previous samples: ±0.2 mm in diameter and ±0.3 mm in depth. The design of Sample D is illustrated in Figure 5.17.

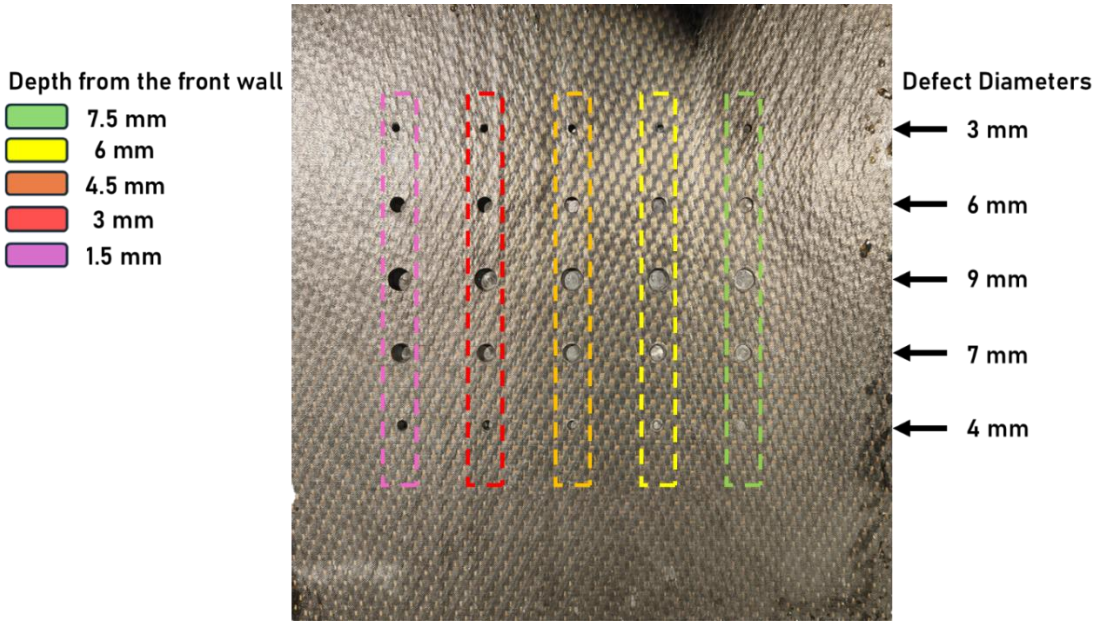


*Figure 5.17. Sample D with FBHs*

The resultant amplitude C-scans of each component are presented in Figure 5.18.

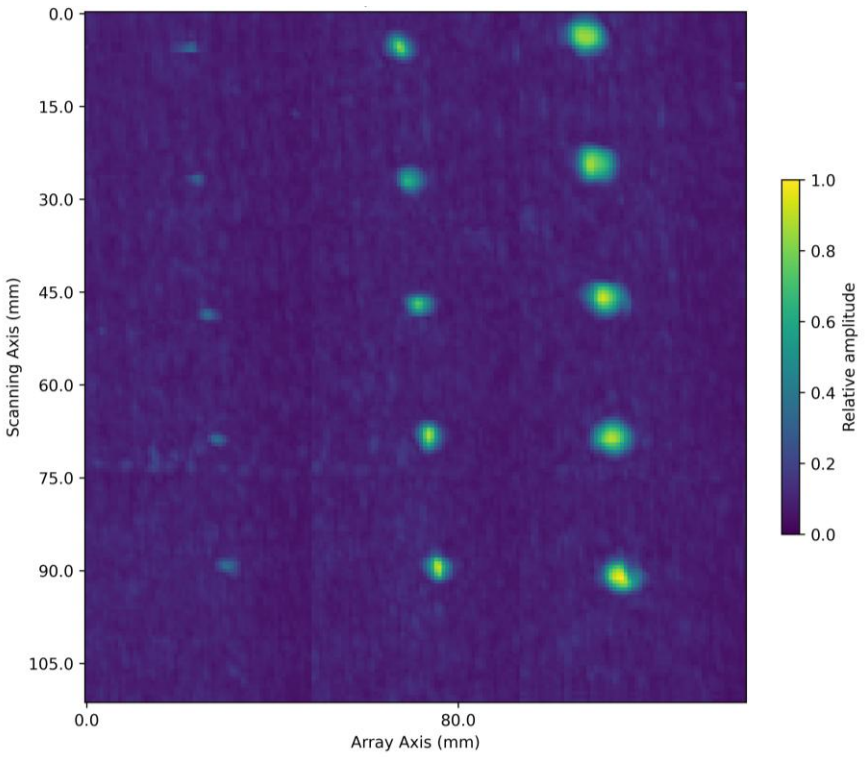
0.0
15.0
30.0
45.0
60.0
75.0
90.0
105.0
Scanning Axis (mm)
0.0
80.0
Array Axis (mm)
1.0
0.8
0.6
0.4
0.2
0.0
Relative amplitude

a)

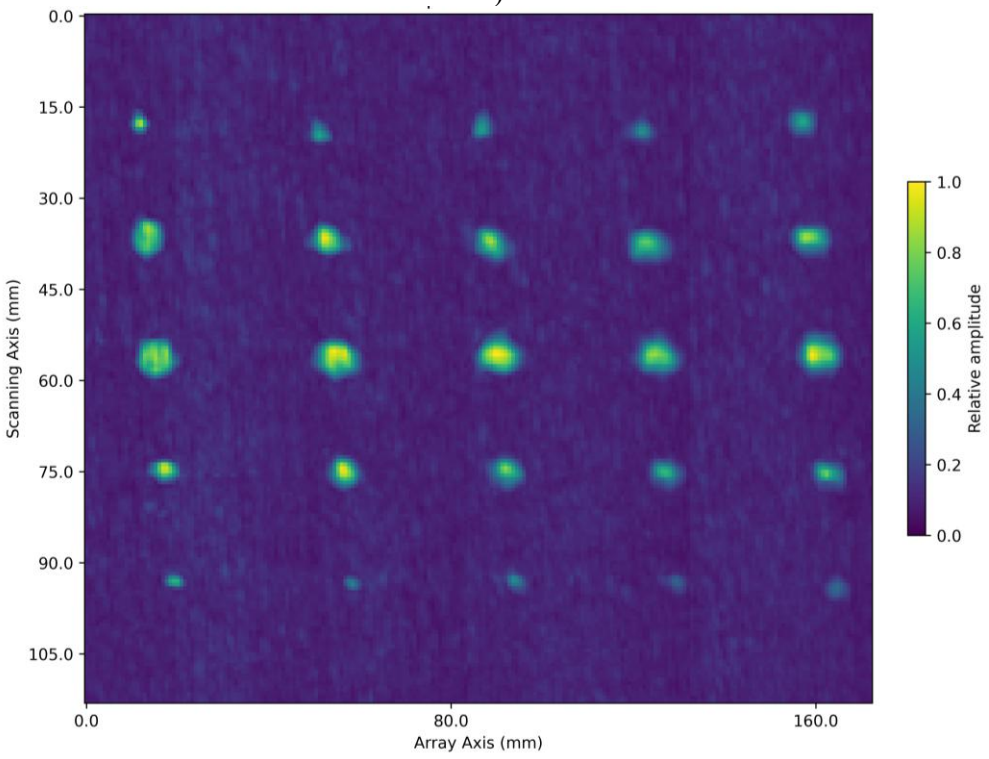
0.0
15.0
30.0
45.0
60.0
75.0
90.0
105.0
Scanning Axis (mm)
0.0
80.0
160.0
Array Axis (mm)
1.0
0.8
0.6
0.4
0.2
0.0
Relative amplitude

b)

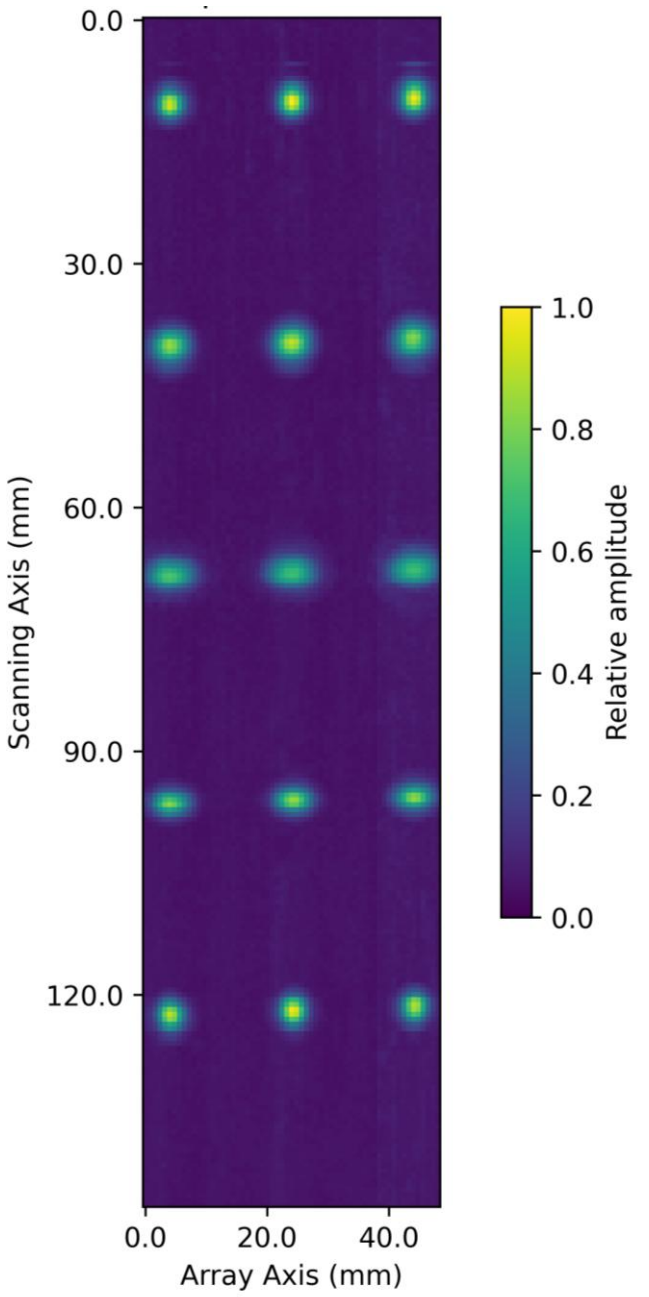


c)

*Figure 5.18. Amplitude C-scans of Inspected Components. a) Sample A – CFRP 15FBHs, b) Sample D – CFRP 25 FBHs, c) Sample B – Aluminium 15 FBHs*

The inspection force was limited to 40 N, compared to the higher forces of up to 55 N used in the previous chapter's inspections. This reduction resulted from changes in the use of ROS and onboard configurations, which restricted access to certain features, including hardware limit tolerances.

All defects were, however, successfully detected across all three samples: 15 in Sample A, 15 in Sample B, and 25 in Sample D. This outcome was encouraging, demonstrating that the inspection system remained fully effective even when operating at a reduced force.

### 5.4.2. Front wall Alignment Validation

As one of the contributions to the improved inspection system involved using the front wall to achieve better alignment, the angles of the front wall measured during inspections were extracted. The mean front-wall angle, standard deviation, and number of measurements for each sample are presented in Table 5.4.

*Table 5.4. Statistical performance of frontwall alignment*

| | Mean Frontwall Angle (°) | STD (°) | Measurements |
|---|---|---|---|
| **Sample A** | -0.009304 | 0.02953 | 2576 |
| **Sample B** | -0.01068 | 0.02037 | 928 |
| **Sample D** | -0.004222 | 0.03502 | 3229 |

The resulting mean front wall angle and standard deviation, presented in Table 5.4 correspond to the angles measured during the inspection after the initial alignment process.

These values indicate that the front wall was maintained close to 0°, with the standard deviation demonstrating less than 0.04° variation in the front wall angle throughout the entire inspection for all samples, even when performed at a reduced force.

## 5.5. Discussion

A major aspect of this work was the introduction of full mobility and driving for inspection scenarios. Positional accuracy and repeatability were validated using a Leica Absolute Laser Tracker, in which the vision-based alignment method significantly outperformed SLAM-based home positioning. Positional standard deviations in the X and Y directions were under 3.2 mm and 1.2 mm, respectively, for vision-based alignment, while SLAM-based alignment showed deviations exceeding 13 mm. Mean error analysis further supported this, with vision-based alignment yielding errors of approximately 2.7 mm and 2.0 mm in X and Y, compared to 25.5 mm and 6.0 mm for SLAM-based positioning.

In terms of alignment parallel to the station, the mean circular angle for vision-based alignment was 179.96°, with a standard deviation of 0.20°, compared to −177.71° and 0.77° for SLAM-based home alignment. Although the angle of the home position was not significant to the work, the higher deviation in results is what shows that the SLAM struggled a bit more than the station-aligned method.

The system's environment-aware logic prevented inspections when no component was present. This was achieved through RGBD camera-based workspace scanning and filtering, which removed undesired point cloud data and validated the presence of a

component before initiating inspection. This feature ensured no accidental damage to equipment by running unnecessary inspections.

Robotic correction and force control were managed through a velocity-based controller, allowing real-time adjustments to maintain the target force. The inspection speed was capped at 4.5 $mms^{-1}$, with emergency stop logic triggered in cases of excessive forces. This ensured safe operation while maintaining high-quality data acquisition. Ultrasonic capturing was synchronised with robotic movement, with B-scans recorded every 0.8 mm and encoded with positional data.

A key improvement in the system was the use of real-time ultrasonic feedback for front-wall alignment correction. The mean front wall angles recorded during inspection were maintained close to zero, with all inspections maintaining angles of less than 0.011°. Sample A had a mean angle of −0.0093° with a SD of 0.0295°, Sample B an angle of −0.0107° with SD of 0.0204°, and Sample D a mean angle of −0.0042° with SD of 0.0350°. These results showed that the system was capable of maintaining consistent probe alignment throughout the inspection process, even on curved geometries.

Across all three test samples, two CFRP and one aluminium, the system correctly detected all of the known defects at their expected locations. Sample A and Sample B each contained 15 FBHs, while Sample D included 25 FBHs of varying sizes. Despite operating at a reduced inspection force of 40N, compared to the previously used 55N in Chapter 4, the system maintained full detection capabilities, indicating robustness in signal acquisition and processing. Since the forces were not the same, a direct comparison of the results statistically was not possible. Increasing the gain in post or during inspection would

not have made any difference to the ability to compare the data, as the reduction in force meant that signal attenuation would be greater. With an increased gain, both the noise and the signal would be increased and would not make for a proper comparison.

Finally, the system generated interactive web-based reports post-inspection. These reports included C-scans, B-scans, time-of-flight plots, and 3D defect visualisations. Operators could interact with scan data, adjust gating parameters in real-time, and export plots for further analysis. This enhanced traceability and provided deeper insights into defect characteristics.

It should be noted that, although the removal of physical enclosures around the robot allows greater freedom of mobility, this can introduce some trade-offs. The lack of physical boundaries can make initialisation of position and localisation more challenging, particularly in dynamic or frequently changing environments.

The absence of enclosures can also introduce additional safety constraints. In the absence of external metrology or monitoring systems to track human operators in the environment, operating speeds should be reduced to maintain safe operation. This can in some instances limit overall task efficiency and places greater emphasis on conservative motion planning and robust safety behaviours.

### 5.5.1. Error Sources and Mitigation

As expected for a system that combines multiple aspects, several error sources may interfere with the performance of the inspection, if not adequately calibrated or mitigated.

These are discussed and ranked based on their potential impact and are visualised in Figure 5.19.

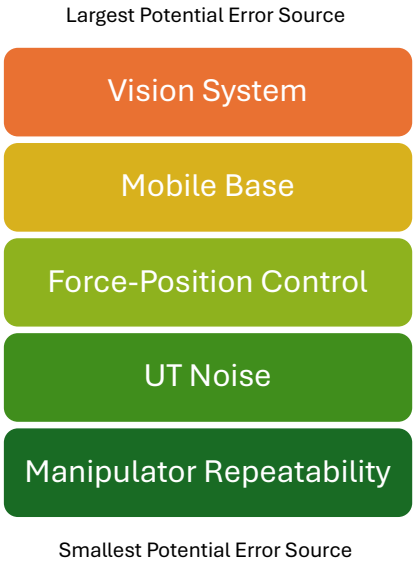


*Figure 5.19. Ranked Possible Error Sources*

The vision system represents the largest possible source of error. Improper calibration of the sensor or hand-eye calibration would directly affect probe placement and orientation, with errors propagating through all subsequent stages of the inspection process.

The mobile base was ranked as the second largest potential source of error. Without reliable localisation, drift in the mobile platform and floor-induced disturbances would introduce large positioning errors, limiting the possibility of repeatable deployments and reducing confidence in probe positioning.

Errors induced by the force-position control would only become evident during the inspection. Poor regulation of contact force could lead to inconsistent coupling, directly affecting ultrasonic signal quality and inspection results.

Ultrasonic noise, specifically noise sources that interfere with or affect the signal, is an error source that would also contribute to inspection variability. These effects would reduce signal quality and lead to less-than-ideal results. Mitigation strategies, such as ensuring isolation of the controller from electrical noise sources and ensuring controlled surface conditions and ambient temperatures, were used to avoid these potential issues.

Manipulator repeatability would be a lesser source of error relative to the others, as industrial manipulators typically maintain good repeatability even without calibration, making it less limiting than absolute positioning errors.

The potential error sources associated with the vision system, mobile base, and force-position control were mitigated through the strategies and deployments discussed throughout this chapter.

## 5.6. Conclusion

This work aimed to investigate the combination of component-aware planning, environment-aware validation, smart robotic alignment, and real-time ultrasonic correction into a collaborative mobile platform that could perform and operate PAUT in unstructured or semi-structured environments. The presented mobile PAUT system offers a scalable solution for industrial NDE. It successfully bridges the gap between robotic precision and real-world variability, enabling reliable inspections in dynamic and unstructured environments.

Experimental validation confirmed the system's ability to detect all known defects across multiple samples, maintain precise alignment, and operate under reduced contact force conditions. The alignment to the station showed a future of using mobile robotics for inspections, without the need to fixture, align or calibrate work environments to precise margins. The camera used was an off-the-shelf, inexpensive camera that could be upgraded to a better system and calibrated to achieve even greater accuracy. The major benefit of the presented system was its full autonomy, with the only known parts being the home positions, to align in the right direction, the size of the station, to ensure enough captures of the station and the calibrated ultrasonic laws required for decision making.

The integration of digital twin technology and advanced reporting tools further enhanced the operational transparency, ensuring that an operator can oversee the operations and the robotic motions. The report generation was an addition that could help greatly in industrial settings, with the logging and tracing, having times, stations, and ultrasonic laws for each

inspection. The report also allowed the user to interact with the data right after the inspection, with all the inspection properties in one location.

It should be noted that the application of the ultrasonic-based robotic adjustment method is limited to inspections conducted with linear 0-degree probes. Angular probes cannot utilise this approach, as angled beams and sectorial scans do not produce front wall reflections.

Looking ahead, future work could focus on expanding the system's compatibility with a wider range of stations and components in larger, more complex environments. This includes linking inspection data to predictive frameworks to estimate inspection times and file sizes, as well as enabling coordinated multi-robot deployments for large-scale inspections. Further studies could explore the optimal balance between scanning frequency and correction speed to achieve faster and more accurate alignment. Additionally, future research should investigate the feasibility of adjusting lower-level parameters, such as direct control of laser systems and safety configurations, although this may be constrained by the experimental nature of the robot's driver, which is not currently maintained or further developed by the KUKA team.

# Chapter 6

# Conclusion and Future Work

## 6.1. Conclusion

Current inspection processes in real-world manufacturing environments demand strict calibration procedures and precise fixturing of components. These requirements often make inspection a bottleneck within the production pipeline, compounded by their high costs, large physical footprints, and limited flexibility. As the NDE sector continues to expand rapidly, the emergence of Industry 4.0 and 5.0 concepts is driving the shift toward greater automation, flexibility, and collaborative operation. This evolution presents immense opportunities for innovation in how inspections are conducted.

This thesis has therefore proposed the development of systems that remove the need for precise fixtures and placements, with the use of Cobot and mobile robotic technologies to present systems that are suitable for shared work environments. The presented work has incorporated industrial focuses and feedback to solve real-world industrial challenges.

One current interest across manufacturing sectors has been to understand how mobile manipulator technologies can be utilised and exploited in beyond traditional logistics and pick-and-place applications. The performance of mobile robotic platforms has not yet

been fully quantified in real-world working environments, with no current procedure in place for measuring their repeatability or accuracy. Therefore, one aim of this thesis was to present an experimental procedure to evaluate the mobile manipulators in a measurement science context, which specifically focused on establishing quantifiable performance benchmarks such as repeatability and positional accuracy. The procedure looked at assessing the mapping capabilities and the operational capabilities of the Mecanum omnidirectional wheels, varying the speeds to understand the impact on the positional accuracy. The evaluation was carried out using the KUKA KMR iiwa mobile manipulator, which quotes positioning accuracies of up to ±5 mm [54]. The testing environment, comprising industrial flooring and a semi-cluttered layout, closely resembled real-world assembly conditions, ensuring that the evaluation reflected practical applications. The evaluation of performance of the mobile manipulators was conducted using an absolute laser tracker with precision of 10 µm and measuring capabilities in all three DoF. Results showed that the enabling of mapping technologies significantly enhanced the KMR iiwa's performance for both accuracy and repeatability. Encoder-based movements showed consistent repeatability errors but were prone to increases in displacement errors over successive runs. Improvements of over 90.8 % were made following the activation of mapping features for strafing tests and 45.3 % for the rotational movements, for repeatability errors. More complicated rotational movements did have a threshold in which the errors increased seen with the 0.24 m/s tests error of 90.9%.

While the 0.24 m/s test in rotational movements showed increased displacement errors, the overall trend shown by the lower speeds was performances with displacement and

repeatability errors remaining under 2 mm. These results highlighted the importance of speed and path complexity in optimising performance.

The thesis also sought to address the strict industrial requirements that demand highly precise placement of components during inspection. It further aimed to reduce the reliance on prior part knowledge by developing an adaptable scanning system capable of identifying components which positions were not predetermined. Such systems are particularly beneficial in scenarios where CAD data is unavailable; for instance, during in-service inspections of classified assets, in high-mix, low-volume production, in one-off inspections, or where CAD models deviate from the physical components due to as-built tolerances or wear. The system was designed to conduct automated PAUT on unfixtured components at arbitrary poses.

The developed system combined the capabilities of 3D vision with various processing algorithms to extract areas of interest. A custom path rasterisation algorithm using PAUT sensor parameters such as probe sizes and probe overlap between passes were utilised. The path planning algorithm was designed flexibly allowing for changes of PAUT parameters permitting different probe types and sizes to be utilised. Calibration of the parameters and the processing algorithms enabled flexible identification and inspection planning processes. The inspection scans showed detection of all the known defects across various scan orientations of the CFRP Sample A, the curved metallic Sample B, as well as the naturally occurring defect found in the curved CFRP Sample C. The inspection of Sample A showed consistent detection of all defects at the various orientations between 20 and -20 with SD of 0.038 in the mean relative amplitude of the 3mm defects, 0.012 for

the 6 mm defects and 0.0060 for the 9 mm defects. The results of inspected Sample B presented values within 2dB of the PSNR of the manually taught system, detecting all manufactured defects and presenting reductions in inspection and preparation times of 97%. The inspection of the curved CFRP Sample C, presented a measured depth of the naturally occurring defect at 2.03 mm, with CT validation concurring, finding the defect at 2.05 mm.

The presented system showed its agnostic inspection capabilities for both material, orientation and limited geometric variations, with the added flexibility of not requiring precise fixturing or teaching of components prior to inspection. Being conducted using a Cobot, the implementation of such a system can further the collaboration between human operators and robots and translate into hundreds of hours saved annually if scaled across routine NDE operations.

This thesis also aimed to combine the above aspects into a fully automated human collaborative mobile PAUT system, capable of inspecting various components without the need for operator intervention. The combination of environment-aware validation, smart robotic alignment, and real-time ultrasonic correction into a collaborative mobile platform allowed the system to perform PAUT in semi-structured environments. The mobile PAUT used the learnings of the accuracy study, by employing tags and a mounted vision system to find and align to inspection stations, without the reliance on SLAM or mapped based modules. This approach yielded mean alignments to the station within 0.04° with a SD of 0.20°. Mean errors were found to be within less than 2.75 mm for both the x and y directions, with percentage differences in error between this alignment method and

the typical SLAM for home positions reaching over 830 %. The system presented full detection of the known defects on the three samples inspected and partnered with the robotically integrated data capturing, the report generation presented back structured and interactive ultrasonic plots for the operator.

The major benefit of system presented in this thesis was its full autonomy, with the only known parts being the home positions, to align in the right direction, the station dimensions, to ensure enough captures of the station and the calibrated ultrasonic laws required for decision making. The system successfully showcased the possibility of bridging the gap between robotic precision and real-world variability, enabling reliable inspections in dynamic and unstructured environments, with the added benefits of traceability and logging of inspection data.

The systems described and presented, including autonomy, inspection planning, environment reasoning, ultrasonic processing, and reporting, are platform-independent and would require only minor interface adjustments to run on different equipment. The primary hardware dependencies lie in the robot control and real-time feedback layers, which would need adapting to each new robotic system's API. Cameras and PAUT data structures are generally similar across platforms, meaning that only small plugins or format converters would be needed.

The experimental validation and discussion presented in this thesis evaluated the proposed system against the requirements and success criteria defined in Section 0 of Chapter 1. System performance was assessed in terms of autonomous operation, inspection

repeatability, ultrasonic data quality, and robustness to uncertainties arising from mobile manipulator deployment.

The culmination of work in this thesis has presented the possibility of an industry changing technology, utilising human collaborative mobile manipulators to perform fully automated NDE inspections without the requirement of an operator. This novel work has showcased the possibility of process-to-part NDE inspections addressing the needs of the Aerospace and High-Value manufacturing sectors.

## 6.2. Challenges and Discussion

This thesis presented a range of successful works and discussed their various results. During the process of the works, challenges were encountered and the most notable are discuss further below.

A major challenge related to the hardware was the downtime suffered due to equipment breakdowns. The robotic systems of the KUKA KMR iiwa and LBR iiwa are both highly advanced; however, this also caused some issues in the diagnosis of technical faults. Because of this, the equipment was down or unavailable for long periods, stretching over a year. The monetary costs of these systems are high, reaching over six figures; therefore, during down periods, it was not possible to simply replace or loan other units. During the downtime while working with KUKA, it was determined that the fault in the omnidirectional wheel motor required a complete wheel replacement, as each wheel was integrated with its corresponding motor. Discussions with KUKA revealed that the KMR

iiwa platform is being discontinued, with the Mecanum wheels replaced by castor wheels in newer models due to the complexity and reliability issues previously encountered.

A key technical challenge encountered during this work was the lack of standardisation across the systems used within the proposed NDE solution. Prototyping required the integration of multiple programming languages and software environments, including Java for robot control, later transitioning to ROS-based C++ and Python modules. Measurement logging was handled through LabVIEW, with MATLAB and Python used for data processing, while proprietary software supported ultrasonic controller interfacing. The need to switch between operating systems and platforms complicated system integration. Future work should focus on refining and consolidating these interfaces as the system progresses through higher Technology Readiness Levels (TRLs).

## 6.3. Suggestions for Future Work

To advance the work presented in this thesis there are a few methods currently being investigated and planned. This thesis presented a successful fully automated inspection solution for small scale components. With the current industrial relationship built with Spirit AeroSystems Ltd, there have been discussions and plans initiated around the scaling up of the work, using larger platforms and manipulators to inspect components of sizes in the tens of metres.

The performance quantification studies of mobile manipulators in this work were limited to a single platform. With greater resources, future investigations should include multiple platforms operating within larger environments and under varying floor conditions to

provide a more comprehensive performance assessment. The studies presented in Chapter 4 and Chapter 5 were conducted on tabletop calibration samples containing FBHs, therefore, validation on real industrial components featuring real defects would represent an important next step in advancing this research.

Defect detection performance in PAUT-based inspection is influenced by a combination of ultrasonic and robotic factors. Parameters such as PAUT sensitivity, the selection and deployment of focal laws, probe aperture, and scan repeatability directly affect defect detectability. Near-field effects are less significant in this work due to the roller probe design, for which the dead zone is contained within the tire rather than the component under inspection. While these aspects are discussed and explored within the scope of this thesis, understanding the capabilities of the complete inspection system in a more representative, real-world setting remains valuable future work. In particular, further evaluation could quantify system performance under varying environmental conditions, such as changes in ambient light affecting 3D camera operation or component surface properties influencing ultrasonic coupling. Such studies would also enable the development of a more tailored inspection system, incorporating custom-designed components and tooling, and moving beyond the current off-the-shelf configuration once system limitations are more fully characterised.

Further development is also required for the automated reporting modules. Depth measurements were found to deviate by approximately 2–3 mm from the true values, indicating the need for additional calibration to achieve higher accuracy in defect depth

estimation. Nonetheless, the implemented feature enhanced operator visualisation and overall interpretability of inspection results.

The standardisation of the complete NDE solution is an aspect that would be beneficial to the next generation of users of such systems. Currently there have been movements to standardise robot operations and their systems, such as using ROS. With robot operations moving to ROS-Industrial[157], there may be a following trend that sees other equipment moving to and embracing the ROS framework to ensure ease of integration and transfer of knowledge and works.

With the constantly changing and advancing technologies available on the market, an interesting adaptation has been the use of Augmented Reality (AR) for its use in visualising and interacting with NDE data at the various stages of the inspection stages. Work was started to understand how the use of AR could be partnered with the work presented in this thesis. The ability to interact with data, or forms or GUI means that instantiations of inspections can be carried out with the operator in or near the environment without the need of a computer. The initial trials showed the ability to visualise B-scan data in Realtime, with adaptive plotting. The presented report generation is an example of the types of data and information available that could be displayed on a AR headset such as the Microsoft HoloLens [158].

One aspect that is currently being explored as a direct result of the work presented in this thesis is the process of creating a spin-out, from the development of a fully automated inspection system utilising the LBR iiwa manipulator partnered with automated defect detection. The system is presented in Figure 6.1.

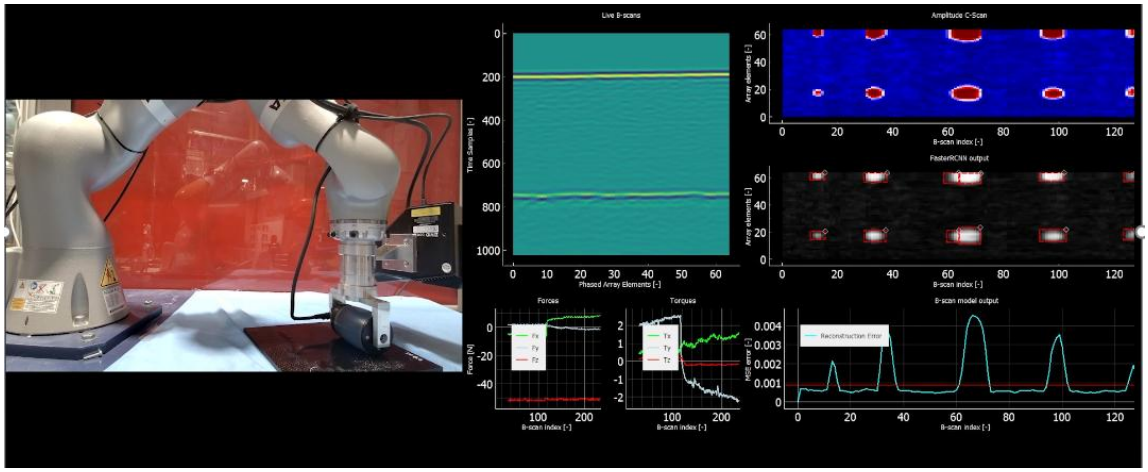


*Figure 6.1. Demonstrator system, showing manipulator during inspection (left) and GUI with live defect detection and model outputs (right)*

This work has been presented to various industrial companies, and at the BINDT Aerospace Conference [159], gaining traction and being supported by the University program to actively pursue the creation of a spin out company. The work presents the capabilities of inspecting components specified by a user from a workspace capture, the custom developed GUI allows for investigating the flagged defective regions during and after inspection. Defects and artefacts are highlighted using multi-modal agreement and the system presents capabilities such as re-inspection, conducted at lower speeds of specific regions for better coverage, based on the information from the robotically encoded ultrasonic captures. This work demonstrates the feasibility and experimental proof-of-concept of such systems and highlights their significant potential to influence current industry practices; however, further development is required to increase technology readiness levels and to achieve the certifications necessary for transition to industrial deployment. One such certification would be a Probability of Detection (POD) qualification, which quantifies inspection reliability. POD measures how well an

inspection procedure detects a given defect based on characteristics, such as size and orientation, and is widely used in aerospace and other safety-critical industries to benchmark inspection capability against acceptance criteria [160]. Conducting these experiments would provide quantitative evidence of the system's performance limits and operational robustness, and would support compliance with regulatory and standardisation requirements for formal qualification.

# References


[1] Z. M. Research, 'Non-Destructive Testing (NDT) Service Market Size, Share, Growth, 2032', Zion Market Research.

[2] A. Kumar and W. Arnold, 'High resolution in non-destructive testing: A review', *Journal of Applied Physics*, vol. 132, no. 10, p. 100901, Sep. 2022, doi: 10.1063/5.0095328.

[3] B. Wang, P. He, Y. Kang, J. Jia, X. Liu, and N. Li, 'Ultrasonic Testing of Carbon Fiber-Reinforced Polymer Composites', *Journal of Sensors*, vol. 2022, pp. 1–20, Jun. 2022, doi: 10.1155/2022/5462237.

[4] K. Huang *et al.*, 'A Through-Transmission Ultrasonic Method for the Detection of Ferrite Tile Defects', *Applied Sciences*, vol. 13, no. 20, Art. no. 20, Jan. 2023, doi: 10.3390/app132011172.

[5] P. D. Wilcox, 'Ultrasonic arrays in NDE: Beyond the B-scan', *AIP Conference Proceedings*, vol. 1511, no. 1, pp. 33–50, Jan. 2013, doi: 10.1063/1.4789029.

[6] R. K. W. Vithanage *et al.*, 'A Phased Array Ultrasound Roller Probe for Automated in-Process/Interpass Inspection of Multipass Welds', *IEEE Trans. Ind. Electron.*, vol. 68, no. 12, pp. 12781–12790, Dec. 2021, doi: 10.1109/TIE.2020.3042112.

[7] R. L. Barron, A. N. Mucciardi, and C. L. Brown, 'System for nondestructive evaluation of material flaw characteristics', US4213183A, Jul. 15, 1980 Accessed: Jul. 15, 2025. [Online]. Available: https://patents.google.com/patent/US4213183A/en

[8] M. Ghobakhloo, 'Industry 4.0, digitization, and opportunities for sustainability', *Journal of Cleaner Production*, vol. 252, p. 119869, Apr. 2020, doi: 10.1016/j.jclepro.2019.119869.

[9] 'Europe Automated Non-Destructive Testing Services Market - Regional Analysis: Focus on Application, Technique, Enabling Technology, and Country - Analysis and Forecast, 2024-2034'. Accessed: Mar. 10, 2025. [Online]. Available: https://bisresearch.com/industry-report/europe-automated-non-destructive-testing-services-market.html

[10] L. Schulenburg, 'NDT 4.0 – A Technology Overview'.

[11] E. Duernberger, C. MacLeod, D. Lines, C. Loukas, and M. Vasilev, 'Adaptive optimisation of multi-aperture ultrasonic phased array imaging for increased inspection speeds of wind turbine blade composite panels', *NDT & E International*, vol. 132, p. 102725, Dec. 2022, doi: 10.1016/j.ndteint.2022.102725.

[12] C. Mineo, 'Automated NDT inspection for large and complex geometries of composite materials', Thesis, 2015.

[13] M. Pantscharowitsch, L. Moser, and B. Kromoser, 'A study of the accuracy of industrial robots and laser-tracking for timber machining across the workspace', *Wood Material Science & Engineering*, vol. 20, no. 1, pp. 75–93, Jan. 2025, doi: 10.1080/17480272.2024.2324437.

[14] N. Cusano, ‘Cobot and Sobot: For a new Ontology of Collaborative and Social Robots’, *Found Sci*, vol. 28, no. 4, pp. 1143–1155, Dec. 2023, doi: 10.1007/s10699-022-09860-2.
[15] ‘ISO 10218-2:2025’, ISO. Accessed: Feb. 09, 2026. [Online]. Available: https://www.iso.org/standard/73934.html
[16] ‘What is Ultrasonic Testing and How Does it Work?’ Accessed: Jul. 15, 2025. [Online]. Available: https://www.twi-global.com/technical-knowledge/faqs/ultrasonic-testing.aspx
[17] M. T. Balmaseda, M. T. Fatehi, S. H. Koozekanani, and A. L. Lee, ‘Ultrasound therapy: a comparative study of different coupling media’, *Arch Phys Med Rehabil*, vol. 67, no. 3, pp. 147–150, Mar. 1986, doi: 10.1016/0003-9993(86)90052-3.
[18] ‘Ultrasound Gel - Surgical Holdings’. Accessed: Aug. 10, 2025. [Online]. Available: https://www.surgicalholdings.co.uk/ultrasound-gel.html
[19] ‘Ultrasonic Transducers: Piezoelectric vs. Magnetostrictive’, Omegasonics. Accessed: Jul. 15, 2025. [Online]. Available: https://www.omegasonics.com/ultrasonic-cleaners/ultrasonic-cleaning-piezoelectric-vs-magnetostrictive-transducers/
[20] H.-G. Knoch and W. Klug, ‘What Is Ultrasound?’, in *Stimulation of Fracture Healing with Ultrasound*, H.-G. Knoch and W. Klug, Eds, Berlin, Heidelberg: Springer, 1991, pp. 40–51. doi: 10.1007/978-3-642-76427-1_5.
[21] ‘EMAT Transducers | Evident Scientific’. Accessed: Jul. 15, 2025. [Online]. Available: https://ims.evidentscientific.com/en/probes/single-and-dual-element/emat-transducers
[22] B. W. Drinkwater and P. D. Wilcox, ‘Ultrasonic arrays for non-destructive evaluation: A review’, *NDT & E International*, vol. 39, no. 7, pp. 525–541, Oct. 2006, doi: 10.1016/j.ndteint.2006.03.006.
[23] L. E. Drain, *Laser Ultrasonics Techniques and Applications*. New York: Routledge, 2019. doi: 10.1201/9780203749098.
[24] J.-R. Lee, H.-J. Shin, C. C. Chia, D. Dhital, D.-J. Yoon, and Y.-H. Huh, ‘Long distance laser ultrasonic propagation imaging system for damage visualization’, *Optics and Lasers in Engineering*, vol. 49, no. 12, pp. 1361–1371, Dec. 2011, doi: 10.1016/j.optlaseng.2011.07.011.
[25] C. Pei, K. Demachi, T. Fukuchi, K. Koyama, and M. Uesaka, ‘Cracks measurement using fiber-phased array laser ultrasound generation’, *Journal of Applied Physics*, vol. 113, no. 16, p. 163101, Apr. 2013, doi: 10.1063/1.4802685.
[26] T. W. Murray, J. B. Deaton, and J. W. Wagner, ‘Experimental evaluation of enhanced generation of ultrasonic waves using an array of laser sources’, *Ultrasonics*, vol. 34, no. 1, pp. 69–77, Mar. 1996, doi: 10.1016/0041-624X(95)00090-P.
[27] J.-P. Monchalin, ‘Laser-Ultrasonics: Principles And Industrial Applications’.
[28] E. Participation, ‘The Control of Artificial Optical Radiation at Work Regulations 2010’. Accessed: Mar. 20, 2025. [Online]. Available: https://www.legislation.gov.uk/uksi/2010/1140

[29] ‘Laser radiation: safety advice’, GOV.UK. Accessed: Mar. 20, 2025. [Online]. Available: https://www.gov.uk/government/publications/laser-radiation-safety-advice/laser-radiation-safety-advice
[30] ‘Ultrasonic Testing: A-scan’. Accessed: Jul. 23, 2025. [Online]. Available: https://www.ndt.net//ndtaz/content.php
[31] ‘B-Scan’. Accessed: Jul. 23, 2025. [Online]. Available: https://www.bindt.org/What-is-NDT/Index-of-acronyms/B/B-Scan/
[32] ‘C-Scan’. Accessed: Jul. 23, 2025. [Online]. Available: https://www.bindt.org/What-is-NDT/Index-of-acronyms/C/C-Scan/
[33] ‘Ultrasonic Testing: C-scan’. Accessed: Jul. 23, 2025. [Online]. Available: https://www.ndt.net//ndtaz/content.php
[34] R. J. Parmee, C. M. Collins, W. I. Milne, and M. T. Cole, ‘X-ray generation using carbon nanotubes’, *Nano Convergence*, vol. 2, no. 1, p. 1, Jan. 2015, doi: 10.1186/s40580-014-0034-2.
[35] T. M. Buzug, ‘Computed Tomography’, in *Springer Handbook of Medical Technology*, R. Kramme, K.-P. Hoffmann, and R. S. Pozos, Eds, Berlin, Heidelberg: Springer Berlin Heidelberg, 2011, pp. 311–342. doi: 10.1007/978-3-540-74658-4_16.
[36] P. J. Withers *et al.*, ‘X-ray computed tomography’, *Nat Rev Methods Primers*, vol. 1, no. 1, pp. 1–21, Feb. 2021, doi: 10.1038/s43586-021-00015-4.
[37] S. F. Cobos, C. J. Norley, S. I. Pollmann, and D. W. Holdsworth, ‘Cost-effective micro-CT system for non-destructive testing of titanium 3D printed medical components’, *PLoS One*, vol. 17, no. 10, p. e0275732, Oct. 2022, doi: 10.1371/journal.pone.0275732.
[38] J. M. De Oliveira, A. C. G. Martins, V. Guimaraes, J. R. B. Oliveira, K. C. D. Macario, and F. A. Genezini, ‘Construction and Test of Low Cost X-Ray Tomography Scanner for Physical-Chemical Analysis and Nondestructive Inspections’, in *AIP Conference Proceedings*, São Sebastião, São Paulo (Brazil): AIP, 2009, pp. 102–105. doi: 10.1063/1.3157786.
[39] J. Zhang, M. Yuan, S.-J. Song, and H.-J. Kim, ‘Precision measurement of coating thickness on ferromagnetic tube using pulsed eddy current technique’, *Int. J. Precis. Eng. Manuf.*, vol. 16, no. 8, pp. 1723–1728, Jul. 2015, doi: 10.1007/s12541-015-0226-7.
[40] ‘Collaborative robotic automation | Cobots from Universal Robots’. Accessed: Feb. 07, 2024. [Online]. Available: https://www.universal-robots.com/, https://www.universal-robots.com/
[41] ‘Industrial Robot Supplier and Manufacturer | ABB Robotics’, Robotics. Accessed: Jul. 22, 2025. [Online]. Available: https://new.abb.com/products/robotics
[42] M. R. Naqvi, A. Sarkar, F. Ameri, L. Elmhadhbi, T. Louge, and M. H. Karray, ‘Ontology-driven integration of advertised and operational capabilities in robots’, *Sci Rep*, vol. 15, no. 1, p. 34326, Oct. 2025, doi: 10.1038/s41598-025-16649-3.
[43] A. Widyacandra, A. R. A. Tahtawi, and M. Martin, ‘Forward and Inverse Kinematics Modeling of 3-DoF AX-12A Robotic Manipulator’, *Jitel (Jurnal Ilmiah Telekomunikasi Elektronika Dan Listrik Tenaga)*, vol. 2, no. 2, pp. 139–150, 2022, doi: 10.35313/jitel.v2.i2.2022.139-150.

[44] Y. Wei, 'The Design and Implementation of Trajectory Planning Based on 4 DOF Industrial Robot', *E3s Web of Conferences*, vol. 522, p. 01035, 2024, doi: 10.1051/e3sconf/202452201035.
[45] L. Zhou, F. Wang, N. Wang, and T. Yuan, 'Application of Industrial Robots in Automated Production Lines Under the Background of Intelligent Manufacturing', *Journal of Physics Conference Series*, vol. 1992, no. 4, p. 042050, 2021, doi: 10.1088/1742-6596/1992/4/042050.
[46] A. Kalatzis, S. Hopko, R. K. Mehta, L. Stanley, and M. P. Wittie, 'Sex Parity in Cognitive Fatigue Model Development for Effective Human-Robot Collaboration', 2022, doi: 10.1109/iros47612.2022.9981097.
[47] E. Karabegović, 'Implementation of Industry 4.0 and Robots in Production Processes of the Metal Industry', *International Journal of Advanced Engineering Research and Science*, vol. 7, no. 12, pp. 169–176, 2020, doi: 10.22161/ijaers.712.26.
[48] O. Madsen *et al.*, 'Integration of Mobile Manipulators in an Industrial Production', *Industrial Robot the International Journal of Robotics Research and Application*, vol. 42, no. 1, pp. 11–18, 2015, doi: 10.1108/ir-09-2014-0390.
[49] M. Rao, L. Lynch, J. Coady, D. Toal, and T. Newe, 'Integration of an MES and AIV Using a LabVIEW Middleware Scheduler Suitable for Use in Industry 4.0 Applications', *Applied Sciences*, vol. 10, no. 20, p. 7054, 2020, doi: 10.3390/app10207054.
[50] S. Haas, T. Ulz, and C. Steger, 'Secured Action Authorization for Industrial Mobile Robots', 2018, doi: 10.1109/icphys.2018.8390810.
[51] 'industrial intelligence 4.0_beyond automation', KUKA AG. Accessed: Jun. 17, 2024. [Online]. Available: https://www.kuka.com/en-gb
[52] N. Adzhar, Y. Yuhani, and M. A. Ahmad, 'A Review on Autonomous Mobile Robot Path Planning Algorithms', *Advances in Science Technology and Engineering Systems Journal*, vol. 5, no. 3, pp. 236–240, 2020, doi: 10.25046/aj050330.
[53] H. Arnarson, B. Solvang, and B. Shu, 'The Application of Open Access Middleware for Cooperation Among Heterogeneous Manufacturing Systems', 2020, doi: 10.1109/sims49386.2020.9121537.
[54] 'KMR iiwa', KUKA AG. Accessed: Dec. 18, 2023. [Online]. Available: https://www.kuka.com/en-gb/products/mobility/mobile-robot-systems/kmr-iiwa
[55] R. Zhao *et al.*, 'Fast Grasping Technique for Differentiated Mobile Phone Frame Based on Visual Guidance', *Machines*, vol. 11, no. 7, p. 689, 2023, doi: 10.3390/machines11070689.
[56] M. Bertovic and I. Virkkunen, 'NDE 4.0: New Paradigm for the NDE Inspection Personnel', in *Handbook of Nondestructive Evaluation 4.0*, N. Meyendorf, N. Ida, R. Singh, and J. Vrana, Eds, Cham: Springer International Publishing, 2021, pp. 1–31. doi: 10.1007/978-3-030-48200-8_9-1.
[57] 'ndt-part1.pdf'. Accessed: Jul. 23, 2025. [Online]. Available: https://uberspec.com/wp-content/uploads/2016/10/ndt-part1.pdf

[58] ‘Materials-KTN-Future-of-NDT-in-UK-economy.pdf’. Accessed: Jul. 23, 2025. [Online]. Available: https://www.bindt.org/downloads/Materials-KTN-Future-of-NDT-in-UK-economy.pdf
[59] ‘The Voice Of Industry. “Safeguarding the future of NDT”’, Lavender International. Accessed: Jul. 23, 2025. [Online]. Available: https://www.lavender-ndt.com/news-and-events/safeguarding-the-future-of-ndt/
[60] ‘IntACOM™ Robotic Inspection’. Accessed: Mar. 25, 2025. [Online]. Available: https://www.twi-global.com/media-and-events/insights/intacom-robotic-inspection
[61] R. Ben Jonathan |. Pierce, Gareth |. Nicholson, Ian |. Cooper, Ian |. Wright, ‘Ultrasonic Inspection with Twin Industrial Robots’. Accessed: Jul. 23, 2025. [Online]. Available: https://www.twi-global.com/technical-knowledge/published-papers/deployment-of-ultrasonic-through-transmission-inspection-using-twin-cooperative-industrial-robots.aspx
[62] ‘NDE Inspection Services | tecnatom.es’. Accessed: Aug. 03, 2025. [Online]. Available: https://www.tecnatom.es/en/nde-inspection-services/
[63] ‘TECNATOM Presents its New Technology that Provides High Productivity During Inspection Activities at Paris Air Show 2015’. Accessed: Aug. 03, 2025. [Online]. Available: https://www.ndt.net//search/docs.php3
[64] ‘Testing Services | tecnatom.es’. Accessed: Aug. 03, 2025. [Online]. Available: https://www.tecnatom.es/en/nde-inspection-services/testing-services/
[65] ‘Welcome to Fill Machine Engineering’. Accessed: Mar. 25, 2025. [Online]. Available: https://www.fill.co.at/en
[66] ‘ACCUBOT NDT SYSTEMS - Probabely the most precise robot from Fill Machine Engineering’. Accessed: Mar. 25, 2025. [Online]. Available: https://www.fill.co.at/en/products/accubot-ndt
[67] ‘6 axis industrial robots TX2-200 | Stäubli’, Staubli. Accessed: Jul. 23, 2025. [Online]. Available: https://www.staubli.com/gb/en/robotics/products/industrial-robots/tx2-200.html
[68] ‘Eddyfi Technologies VersaTrax™ inspection crawlers’. Accessed: Mar. 26, 2025. [Online]. Available: https://www.eddyfi.com/en/product/versatrax-inspection-crawlers
[69] ‘Automated Inspection Systems | Evident Scientific’. Accessed: Mar. 26, 2025. [Online]. Available: https://ims.evidentscientific.com/en/automated-inspection
[70] ‘RCNDE Technology Transfer Workshop 2025’, presented at the RCNDE Technology Transfer Workshop, Apr. 2025.
[71] ‘RB-KAIROS+ Manipulator - Pick & Place Robot | Robotnik®’, Robotnik. Accessed: Jan. 26, 2024. [Online]. Available: https://robotnik.eu/products/mobile-manipulators/rb-kairos/
[72] ‘Enabled Robotics | Mobile Cobots’, Enabled Robotics. Accessed: Jun. 17, 2024. [Online]. Available: https://www.enabled-robotics.com
[73] ‘Husky A300’, Clearpath Robotics. Accessed: Aug. 03, 2025. [Online]. Available: https://clearpathrobotics.com/husky-a300-unmanned-ground-vehicle-robot/
[74] ‘ER-FLEX - Automate repetitive tasks, empower your team’. Accessed: Jun. 17, 2024. [Online]. Available: https://mobile-industrial-robots.com/

[75] Mobile Industrial Robots, *Inspecting the caster wheels on MiR250*, (Dec. 20, 2023). Accessed: Aug. 03, 2025. [Online Video]. Available: https://www.youtube.com/watch?v=B-XZoR7vcZU
[76] Y. Li, H. Lang, and Y. Wang, 'Vision-Based Motion Control for an 8-DOF Robotic Mobile Manipulator', in *2025 IEEE International systems Conference (SysCon)*, Apr. 2025, pp. 1–7. doi: 10.1109/SysCon64521.2025.11014802.
[77] C. Wang *et al.*, 'Learning Mobile Manipulation through Deep Reinforcement Learning', *Sensors*, vol. 20, no. 3, Art. no. 3, Jan. 2020, doi: 10.3390/s20030939.
[78] 'Husky Spec Comparison', Clearpath Robotics. Accessed: Aug. 03, 2025. [Online]. Available: https://clearpathrobotics.com/husky-spec-comparison/
[79] 'ROS 2 Documentation — ROS 2 Documentation: Foxy documentation'. Accessed: Aug. 03, 2025. [Online]. Available: https://docs.ros.org/en/foxy/index.html
[80] 'Mobile Manipulation Platform Husky | MOBILE MANIPULATION PLATFORM HUSKY'. Accessed: Aug. 03, 2025. [Online]. Available: https://www.docs.mybotshop.de/projects/robot_mmp_husky/html/index.html
[81] A. Gfrerrer, 'Geometry and kinematics of the Mecanum wheel', *Computer Aided Geometric Design*, vol. 25, no. 9, pp. 784–791, Dec. 2008, doi: 10.1016/j.cagd.2008.07.008.
[82] B. Burger *et al.*, 'A mobile robotic chemist', *Nature*, vol. 583, no. 7815, pp. 237–241, Jul. 2020, doi: 10.1038/s41586-020-2442-2.
[83] K. Dörfler *et al.*, 'Additive Manufacturing using mobile robots: Opportunities and challenges for building construction', *Cement and Concrete Research*, vol. 158, p. 106772, Aug. 2022, doi: 10.1016/j.cemconres.2022.106772.
[84] D. Lee and K. Han, 'Autonomous Navigation and Positioning of a Real-Time and Automated Mobile Robotic Welding System', *Journal of Construction Engineering and Management*, vol. 151, no. 5, p. 04025033, May 2025, doi: 10.1061/JCEMD4.COENG-16053.
[85] A. K. Ramasubramanian and N. Papakostas, 'Operator - mobile robot collaboration for synchronized part movement', *Procedia CIRP*, vol. 97, pp. 217–223, Jan. 2021, doi: 10.1016/j.procir.2020.05.228.
[86] W. Jackson *et al.*, 'Magnetic Inspection Platform for Teleoperated Remote Inspections of Complex Geometry', in *2022 49th Annual Review of Progress in Quantitative Nondestructive Evaluation*, San Diego, California: American Society of Mechanical Engineers, Jul. 2023, p. V001T09A001. doi: 10.1115/QNDE2022-98358.
[87] J. James, G. Clarke, R. Mathew, B. Mulkeen, and N. Papakostas, 'On Reducing the Localisation Error of Modern Mobile Robotic Platforms', *Procedia CIRP*, vol. 112, pp. 168–173, Jan. 2022, doi: 10.1016/j.procir.2022.09.067.
[88] A. C. Bavelos *et al.*, 'Enabling Flexibility in Manufacturing by Integrating Shopfloor and Process Perception for Mobile Robot Workers', *Applied Sciences*, vol. 11, no. 9, Art. no. 9, Jan. 2021, doi: 10.3390/app11093985.
[89] M. Shneier and R. Bostelman, 'Literature Review of Mobile Robots for Manufacturing', National Institute of Standards and Technology, NIST IR 8022, May 2015. doi: 10.6028/NIST.IR.8022.

[90] M. Ben-Ari and F. Mondada, 'Robots and Their Applications', in *Elements of Robotics*, M. Ben-Ari and F. Mondada, Eds, Cham: Springer International Publishing, 2018, pp. 1–20. doi: 10.1007/978-3-319-62533-1_1.
[91] C. Zheng, Y. Zhang, J. Li, J. Bai, X. Qin, and B. Eynard, 'Survey on Design Approaches for Robotic Manufacturing Systems in SMEs', *Procedia CIRP*, vol. 84, pp. 16–21, Jan. 2019, doi: 10.1016/j.procir.2019.04.183.
[92] C. Mineo *et al.*, 'Fast ultrasonic phased array inspection of complex geometries delivered through robotic manipulators and high speed data acquisition instrumentation', in *2016 IEEE International Ultrasonics Symposium (IUS)*, Sep. 2016, pp. 1–4. doi: 10.1109/ULTSYM.2016.7728746.
[93] F. Rubio, F. Valero, and C. Llopis-Albert, 'A review of mobile robots: Concepts, methods, theoretical framework, and applications', *International Journal of Advanced Robotic Systems*, vol. 16, no. 2, p. 1729881419839596, Mar. 2019, doi: 10.1177/1729881419839596.
[94] C. Coombs, D. Hislop, S. K. Taneva, and S. Barnard, 'The strategic impacts of Intelligent Automation for knowledge and service work: An interdisciplinary review', *The Journal of Strategic Information Systems*, vol. 29, no. 4, p. 101600, Dec. 2020, doi: 10.1016/j.jsis.2020.101600.
[95] J. Arents and M. Greitans, 'Smart Industrial Robot Control Trends, Challenges and Opportunities within Manufacturing', *Applied Sciences*, vol. 12, no. 2, Art. no. 2, Jan. 2022, doi: 10.3390/app12020937.
[96] M. Chui, J. Manyika, M. Miremadi, and K. George, 'Human + machine: A new era of automation in manufacturing'.
[97] 'ISO 24647:2023(en), Non-destructive testing — Robotic ultrasonic test systems — General requirements'. Accessed: Jan. 25, 2024. [Online]. Available: https://www.iso.org/obp/ui/en/#iso:std:iso:24647:ed-1:v1:en
[98] 'ISO 9283:1998(en), Manipulating industrial robots — Performance criteria and related test methods'. Accessed: Jan. 24, 2024. [Online]. Available: https://www.iso.org/obp/ui/#iso:std:iso:9283:ed-2:v1:en
[99] M. Stuede, K. Nuelle, S. Tappe, and T. Ortmaier, 'Door opening and traversal with an industrial cartesian impedance controlled mobile robot', in *2019 International Conference on Robotics and Automation (ICRA)*, May 2019, pp. 966–972. doi: 10.1109/ICRA.2019.8793866.
[100] J. Li, J. Xue, D. Fu, C. Gui, and X. Wang, 'Position Estimation and Error Correction of Mobile Robots Based on UWB and Multisensors', *Journal of Sensors*, vol. 2022, p. e7071466, Mar. 2022, doi: 10.1155/2022/7071466.
[101] 'Evaluation of the Path-Tracking Accuracy of a Three-Wheeled Omnidirectional Mobile Robot Designed as a Personal Assistant - PMC'. Accessed: Oct. 18, 2022. [Online]. Available: https://www.ncbi.nlm.nih.gov/pmc/articles/PMC8587751/
[102] Y. Li *et al.*, 'Kinematic Modeling of a Combined System of Multiple Mecanum-Wheeled Robots with Velocity Compensation', *Sensors (Basel)*, vol. 20, no. 1, p. 75, Dec. 2019, doi: 10.3390/s20010075.
[103] A. Papavasileiou, Michalos ,G., and S. and Makris, 'Quality control in manufacturing – review and challenges on robotic applications', *International*

*Journal of Computer Integrated Manufacturing*, vol. 38, no. 1, pp. 79–115, Jan. 2025, doi: 10.1080/0951192X.2024.2314789.
[104] R. Zimermann *et al.*, 'Collaborative Robotic Wire + Arc Additive Manufacture and Sensor-Enabled In-Process Ultrasonic Non-Destructive Evaluation', *Sensors*, vol. 22, no. 11, Art. no. 11, Jan. 2022, doi: 10.3390/s22114203.
[105] 'Nondestructive Evaluation Physics : Waves'. Accessed: Feb. 12, 2026. [Online]. Available: https://www.nde-ed.org/Physics/Waves/modeconversion.xhtml
[106] B. C. Jiang, J. T. Black, and R. Duraisamy, 'A review of recent developments in robot metrology', *Journal of Manufacturing Systems*, vol. 7, no. 4, pp. 339–357, Jan. 1988, doi: 10.1016/0278-6125(88)90044-1.
[107] *Read 'An Assessment of Selected Research Programs and Goals of the Engineering Laboratory at the National Institute of Standards and Technology: Fiscal Year 2024' at NAP.edu*. doi: 10.17226/27444.
[108] *Code of practice for installation of resilient floor coverings*, 8203:2017, 2017.
[109] 'Leica Geosystems'. Accessed: Jun. 16, 2024. [Online]. Available: https://leica-geosystems.com/
[110] 'Vicon | Award Winning Motion Capture Systems', Vicon. Accessed: Jun. 16, 2024. [Online]. Available: https://www.vicon.com/
[111] R. Summan *et al.*, 'Spatial calibration of large volume photogrammetry based metrology systems', *Measurement*, vol. 68, pp. 189–200, May 2015, doi: 10.1016/j.measurement.2015.02.054.
[112] 'LattePanda - x86 Windows/Linux Single Board Computers', Lattepanda Tech Support Forum. Accessed: Nov. 07, 2025. [Online]. Available: https://www.lattepanda.com/
[113] 'Hexagon Manufacturing Intelligence'. Accessed: Feb. 09, 2026. [Online]. Available: https://shop.hexagonmi.com/na/en_US/USD/Catalog/Laser-Tracker/Reflectors/Red-Ring-Reflector-1-5%22-%28RRR%29-2-Pack/p/576241
[114] 'S300 - Safety laser scanners | SICK'. Accessed: Jun. 17, 2024. [Online]. Available: https://www.sick.com/gb/en/c/g187227
[115] H. Durrant-Whyte and T. Bailey, 'Simultaneous Localisation and Mapping (SLAM): Part I The Essential Algorithms'.
[116] Z. Wu, X. Deng, S. Li, and Y. Li, 'OC-SLAM: Steadily Tracking and Mapping in Dynamic Environments', *Frontiers in Energy Research*, vol. 9, 2021, Accessed: Nov. 02, 2023. [Online]. Available: https://www.frontiersin.org/articles/10.3389/fenrg.2021.803631
[117] 'Standard Test Method for Navigation: Defined Area'. Accessed: Apr. 15, 2024. [Online]. Available: https://www.astm.org/f3244-21.html
[118] 'KUKA Sunrise.OS', KUKA AG. Accessed: Feb. 15, 2024. [Online]. Available: https://www.kuka.com/en-gb/products/robotics-systems/software/system-software/sunriseos
[119] C. Mineo, B. Wright, I. Nicholson, I. Cooper, and S. Pierce, 'PAUT inspection of complex shaped composite materials through 6 DOFs robotic manipulators', Sep. 2014.
[120] J. Leng *et al.*, 'Industry 5.0: Prospect and retrospect', *Journal of Manufacturing Systems*, vol. 65, pp. 279–295, Oct. 2022, doi: 10.1016/j.jmsy.2022.09.017.

[121] J. F. Castillo *et al.*, ‘COBOTS in Industry 4.0: Safe and Efficient Interaction’, in *Collaborative and Humanoid Robots*, IntechOpen, 2021. doi: 10.5772/intechopen.99540.
[122] Z. Huda, N. I. Taib, and T. Zaharinie, ‘Characterization of 2024-T3: An aerospace aluminum alloy’, *Materials Chemistry and Physics*, vol. 113, no. 2, pp. 515–517, Feb. 2009, doi: 10.1016/j.matchemphys.2008.09.050.
[123] Zivid, ‘Medium Zivid One Plus 3D camera’. Accessed: Aug. 08, 2024. [Online]. Available: https://www.zivid.com/zivid-one-plus-medium-3d-camera
[124] J. Geng, ‘Structured-light 3D surface imaging: a tutorial’, *Adv. Opt. Photon., AOP*, vol. 3, no. 2, pp. 128–160, Jun. 2011, doi: 10.1364/AOP.3.000128.
[125] ‘LBR iiwa’, KUKA AG. Accessed: Aug. 05, 2024. [Online]. Available: https://www.kuka.com/en-gb/products/robotics-systems/industrial-robots/lbr-iiwa
[126] ‘RollerFORM: Phased Array Wheel Probe’. Accessed: Aug. 05, 2024. [Online]. Available: https://www.olympus-ims.com/en/rollerform/
[127] ‘MicoPulse 6PA | Phased Array Ultrasonic Technology | Peak NDT’. Accessed: Sep. 24, 2024. [Online]. Available: https://www.peakndt.com/products/micropulse-6pa/
[128] A. S. Birring, ‘Ultrasonic Angle Beam Calibration - Notches and Side Drilled Holes’.
[129] R. Drai, F. Sellidj, M. Khelil, and A. Benchaala, ‘Elaboration of some signal processing algorithms in ultrasonic techniques: application to materials NDT’, *Ultrasonics*, vol. 38, no. 1, pp. 503–507, Mar. 2000, doi: 10.1016/S0041-624X(99)00082-7.
[130] M. Ester, H.-P. Kriegel, J. Sander, and X. Xu, ‘A Density-Based Algorithm for Discovering Clusters in Large Spatial Databases with Noise’.
[131] S. V. Burtsev and Ye. P. Kuzmin, ‘An efficient flood-filling algorithm’, *Computers & Graphics*, vol. 17, no. 5, pp. 549–561, Sep. 1993, doi: 10.1016/0097-8493(93)90006-U.
[132] G. Law, ‘Quantitative Comparison of Flood Fill and Modified Flood Fill Algorithms’, *IJCTE*, pp. 503–508, 2013, doi: 10.7763/IJCTE.2013.V5.738.
[133] A. Poole, M. Sutcliffe, G. Pierce, and A. Gachagan, ‘A Novel Complete-Surface-Finding Algorithm for Online Surface Scanning with Limited View Sensors’, *Sensors*, vol. 21, no. 22, Art. no. 22, Jan. 2021, doi: 10.3390/s21227692.
[134] R. Horaud and F. Dornaika, ‘Hand-Eye Calibration’, *The International Journal of Robotics Research*, vol. 14, no. 3, pp. 195–210, Jun. 1995, doi: 10.1177/027836499501400301.
[135] ‘Hand-Eye Calibration — ZIVID KNOWLEDGE BASE documentation’. Accessed: Nov. 02, 2025. [Online]. Available: https://support.zivid.com/en/latest/academy/applications/hand-eye.html
[136] E. H. Moore, *On the Reciprocal of the General Algebraic Matrix, Bulletin of the American Mathematical Society,№ 26.*, 1920.
[137] ‘XC130 150g Unidirectional Prepreg Carbon Fibre 300mm - Easy Composites’. Accessed: Apr. 22, 2025. [Online]. Available: https://www.easycomposites.co.uk/xc130-150g-unidirectional-prepreg-carbon-fibre

[138] ‘(PDF) Diffraction and shadowing errors in -6 dB defect sizing of delaminations in composites’, *ResearchGate*, Aug. 2025, Accessed: Nov. 03, 2025. [Online]. Available: https://www.researchgate.net/publication/289802940_Diffraction_and_shadowing_errors_in_-6_dB_defect_sizing_of_delaminations_in_composites
[139] ‘A study of machine learning object detection performance for phased array ultrasonic testing of carbon fibre reinforced plastics - ScienceDirect’. Accessed: Jun. 16, 2025. [Online]. Available: https://www.sciencedirect.com/science/article/pii/S0963869524000598?via%3Dihub
[140] ‘ISO 11666:2018’, ISO. Accessed: Nov. 03, 2025. [Online]. Available: https://www.iso.org/standard/69610.html
[141] S. Cantero-Chinchilla, P. D. Wilcox, and A. J. Croxford, ‘Deep learning in automated ultrasonic NDE -- developments, axioms and opportunities’, *NDT & E International*, vol. 131, p. 102703, Oct. 2022, doi: 10.1016/j.ndteint.2022.102703.
[142] P. Kopardekar, A. Mital, and S. Anand, ‘Manual, Hybrid and Automated Inspection Literature and Current Research Current Research’, *Integrated Manufacturing Systems*, vol. 4, no. 1, pp. 18–29, Jan. 1993, doi: 10.1108/09576069310023838.
[143] D. Garnier, D. Garnier, P. Louviot, and A. Tachattahte, ‘Robotised UT Transmission NDT of Composite Complex Shaped Parts’.
[144] ‘Zivid 2 M70’. Accessed: Oct. 21, 2025. [Online]. Available: https://www.zivid.com/zivid-2-m70
[145] ‘ROS: Home’. Accessed: Oct. 21, 2025. [Online]. Available: https://www.ros.org/
[146] ‘noetic - ROS Wiki’. Accessed: Nov. 09, 2025. [Online]. Available: https://wiki.ros.org/noetic
[147] *ros-planning/navigation*. (Oct. 21, 2025). C++. ROS Planning. Accessed: Oct. 21, 2025. [Online]. Available: https://github.com/ros-planning/navigation
[148] ‘GitHub - IFL-CAMP/iiwa_stack: ROS integration for the KUKA LBR IIWA R800/R820 (7/14 Kg).’ Accessed: Oct. 21, 2025. [Online]. Available: https://github.com/IFL-CAMP/iiwa_stack
[149] *BehaviorTree/BehaviorTree.CPP*. (Oct. 21, 2025). C++. BehaviorTree. Accessed: Oct. 21, 2025. [Online]. Available: https://github.com/BehaviorTree/BehaviorTree.CPP
[150] Z. Tang, R. Grompone von Gioi, P. Monasse, and J.-M. Morel, ‘A Precision Analysis of Camera Distortion Models’, *IEEE Transactions on Image Processing*, vol. 26, no. 6, pp. 2694–2704, Jun. 2017, doi: 10.1109/TIP.2017.2686001.
[151] ‘About’, OpenCV. Accessed: Oct. 10, 2025. [Online]. Available: https://opencv.org/about/
[152] E. Olson, ‘AprilTag: A robust and flexible visual fiducial system’, in *2011 IEEE International Conference on Robotics and Automation*, May 2011, pp. 3400–3407. doi: 10.1109/ICRA.2011.5979561.
[153] S. G. Kwak and J. H. Kim, ‘Central limit theorem: the cornerstone of modern statistics’, *Korean J Anesthesiol*, vol. 70, no. 2, pp. 144–156, Apr. 2017, doi: 10.4097/kjae.2017.70.2.144.

[154] S. Turney, ‘Central Limit Theorem | Formula, Definition & Examples’, Scribbr. Accessed: Oct. 13, 2025. [Online]. Available: https://www.scribbr.co.uk/stats/central-limit-theorem-explained/
[155] A. Maćkiewicz and W. Ratajczak, ‘Principal components analysis (PCA)’, *Computers & Geosciences*, vol. 19, no. 3, pp. 303–342, Mar. 1993, doi: 10.1016/0098-3004(93)90090-R.
[156] ‘linregress — SciPy v1.16.2 Manual’. Accessed: Oct. 17, 2025. [Online]. Available: https://docs.scipy.org/doc/scipy/reference/generated/scipy.stats.linregress.html
[157] A. H. C. T. C. C. B. H. D. F. P. Publications *et al.*, ‘ROS-Industrial’, ROS-Industrial. Accessed: Nov. 12, 2025. [Online]. Available: https://rosindustrial.org
[158] joyjaz, ‘Microsoft HoloLens’. Accessed: Oct. 30, 2025. [Online]. Available: https://learn.microsoft.com/en-us/hololens/
[159] ‘Aerospace Event 2024’. Accessed: Nov. 13, 2025. [Online]. Available: https://www.bindt.org/events-and-awards/PastEventsandWebinars/aerospace-event-2024/?insite_mode=2&insite_tryflushcache=8024
[160] ‘Probability of Detection - NDT, flaw detection | TWI’. Accessed: Feb. 12, 2026. [Online]. Available: https://www.twi-global.com/what-we-do/services-and-support/asset-management/non-destructive-testing/probability-of-detection.aspx

# Appendix A – Camera Spatial Resolution [123]

Figure 3 - Zivid One+ M FOV

All values in degrees or mm.

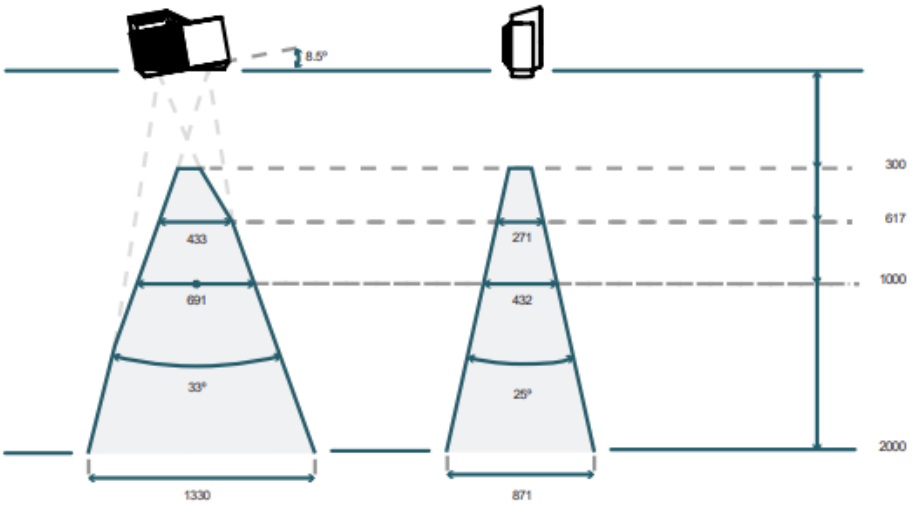


FIGURE 4 - ZIVID ONE+ M SPATIAL RESOLUTION VS. DISTANCE

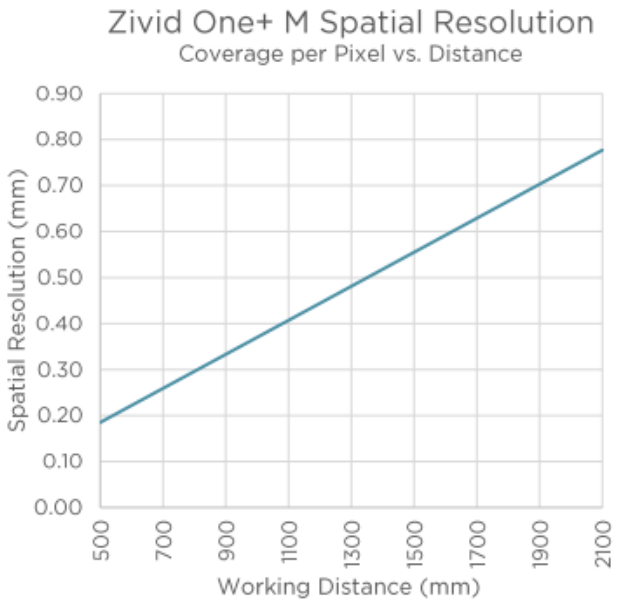

# Appendix B – Flood Fill Path Finding Pseudocode

**Algorithm: Flood Fill Path Finding Pseudocode**

Input: Grid[rows][cols] (2D array of elevation values), start (entrance), end (exit)
Output: Shortest path from start to end

**1.** Initialize:
   a. Create a Queue for cells to process: Queue = []
   b. Create a Visited grid to track visited cells: Visited[rows][cols] = False
   c. Distance[start.row][start.col] = 0
   d. Mark start as Visited: Visited[start.row][start.col] = True
   e. Add Start to Queue: Enqueue(Queue, Start)

**2.** Define Elevation Grid:
   a. For each cell (r, c) in Grid:
      i. Calculate elevation value based on distance from the center or given data.
      ii. Store the elevation value in Grid[r][c].

**3.** While Queue is not empty:
   a. Current = Dequeue(Queue)
   b. If Current == End:
      Break (Shortest path found)
   c. For each Neighbor in Current's 4-connected neighbors (up, down, left, right):
      i. If Neighbor is within bounds and not Visited:
         ii. If elevation[Neighbor] allows traversal:
            - Mark Neighbor as Visited.
            - Set Distance[Neighbor] = Distance[Current] + 1.
            - Enqueue(Queue, Neighbor).

**4.** Traceback Path:
   a. Start from End and backtrack using Distance values to construct the shortest path.

**5.** Output the shortest path and all traversed paths.

**End Algorithm**

# Appendix C – CAD for Experimental Applications

## C-1. Introduction

Computer-Aided Design (CAD) refers to the use of computer systems to aid in the design and creation of components. While commonly applied to the modelling of physical parts, CAD is also used extensively in engineering for conceptual design and development processes. Throughout this work, CAD played a significant role in the design and fabrication of samples, fixtures, and supporting structures. This section outlines the CAD models developed and utilised across the various projects presented in this thesis.

## C-2. Mounts

### C-2.1. Flexible Adapter Plate

Several mounts and fixtures for the robots were already available and routinely used within the working environment; however, these lacked a standardised mounting procedure or design. To address this, a flexible adapter plate was developed to interface with both the existing fixtures and the KUKA LBR iiwa robot's flange. The design of this adapter plate is shown in Appendix Figure C. 1. Fabricated from aluminium, the adapter enabled the secure attachment of the assembly described in Section C-2.3. Probe and Camera Mount.

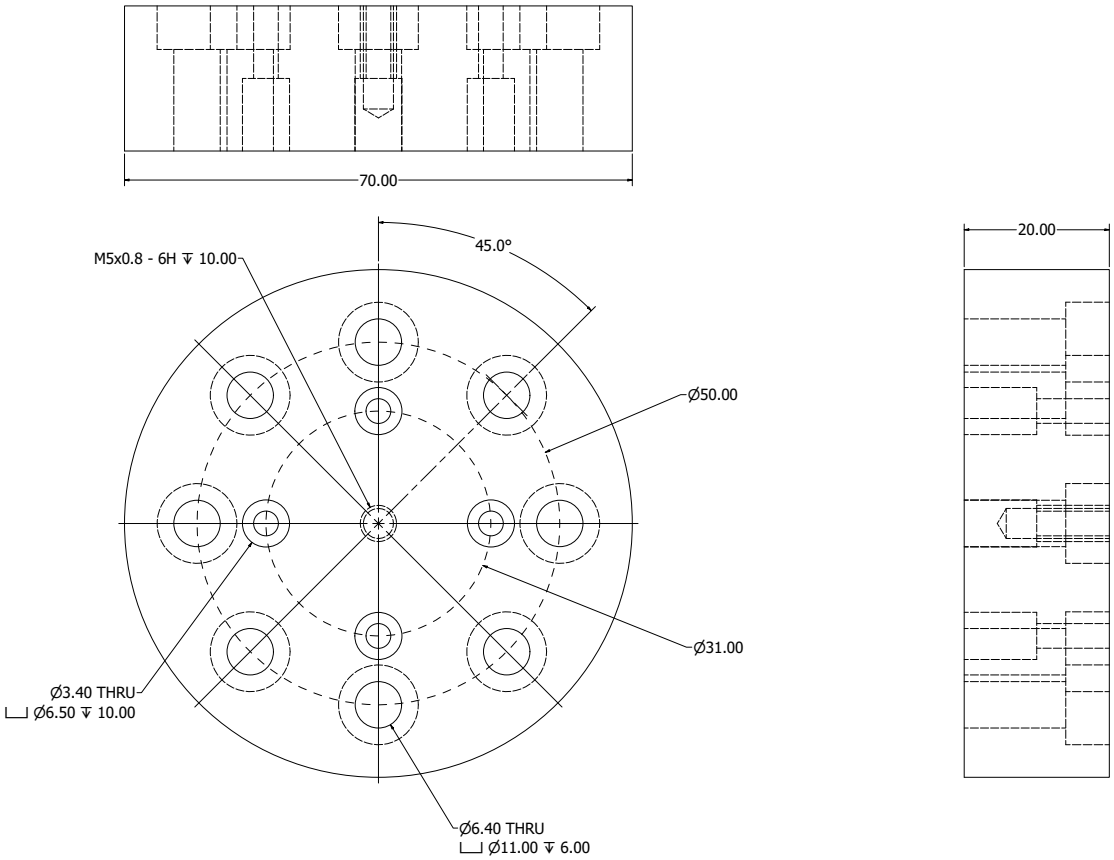


*Appendix Figure C. 1. Flexible adapter plate – Featuring various views (units in mm)*

## C-2.2. Spike Probe

Validation of the camera's hand-eye calibration was required; therefore, a spike probe was designed and fabricated for this purpose. The probe was used to make contact with a secondary spike mounted on the table surface, to check for any positional offset resulting from calibration errors. The design of the spike probe, shown in Appendix Figure C. 2, was produced using 3D printing.

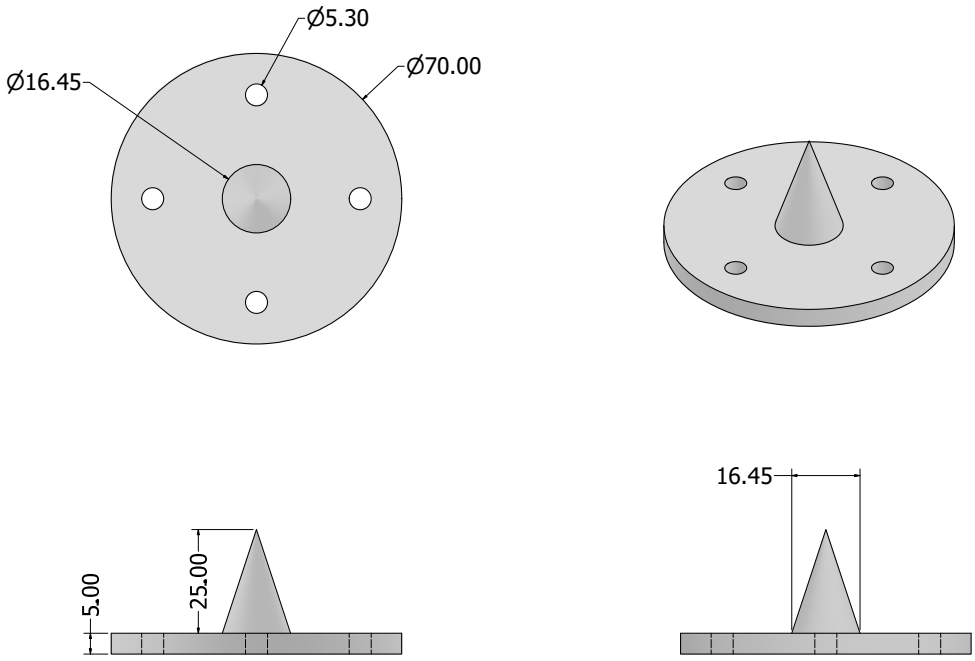


*Appendix Figure C. 2. 3D printed spike probe. – Featuring various views (units in mm)*

## C-2.3. Probe and Camera Mount

To integrate the 3D camera and ultrasonic probe, a dedicated mounting design was developed, as shown in Appendix Figure C. 3. The complete assembly is illustrated in Appendix Figure C. 3 a), with an exploded view detailing the individual components in Appendix Figure C. 3 b). This design facilitated interfacing between the robotic flange, the 3D camera, and the ultrasonic roller probe. The prototype was initially tested using 3D printing and subsequently finalised in aluminium for improved durability and stability. A detailed breakdown of each component is provided in Section C-5. Breakdown of Probe Assembly.

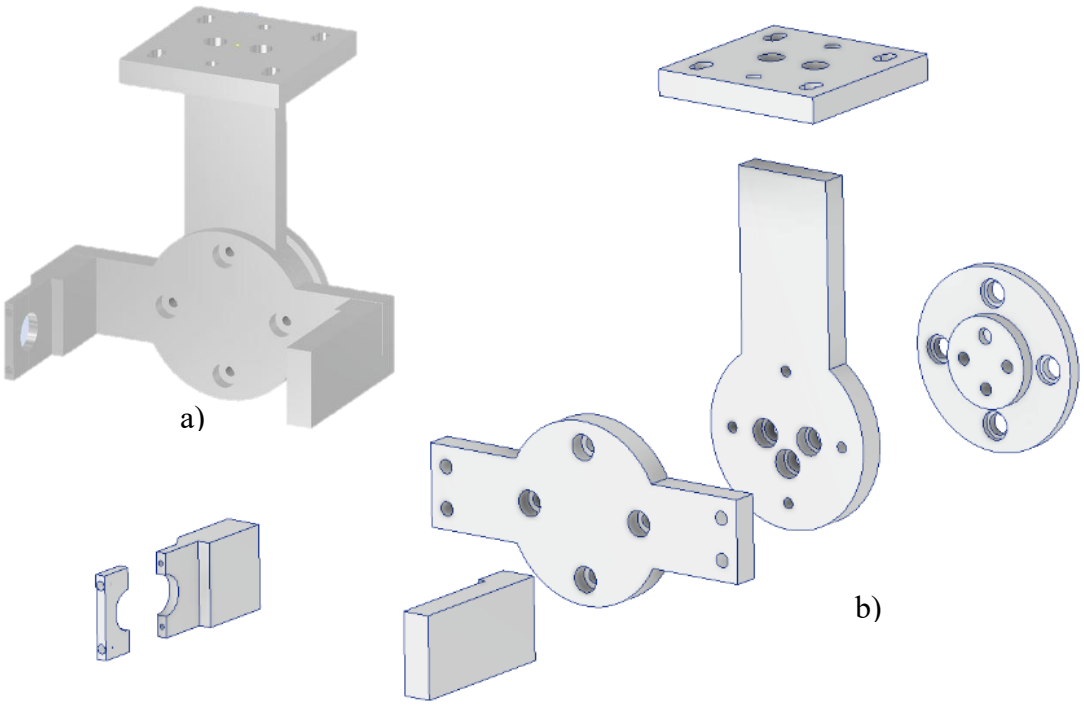


*Appendix Figure C. 3. Complete probe and camera fixture. a) Assembled fixturing, b) Expanded view of fixturing components*

## C-3. Fixtures

For the experimental validation of the flexible robotic system in Chapter 4, it was necessary to test the system's ability to deal with varying poses for inspecting samples. Using Sample A (described in Chapter 4), a fixture was developed that allowed the sample to be mounted at adjustable angles. An adjustable angle plate served as the base, onto which custom adapter plates were designed and 3D printed to enable secure attachment of the sample. The design of the fixture and completed assembly are shown in Appendix Figure C. 4 a) and b), respectively.

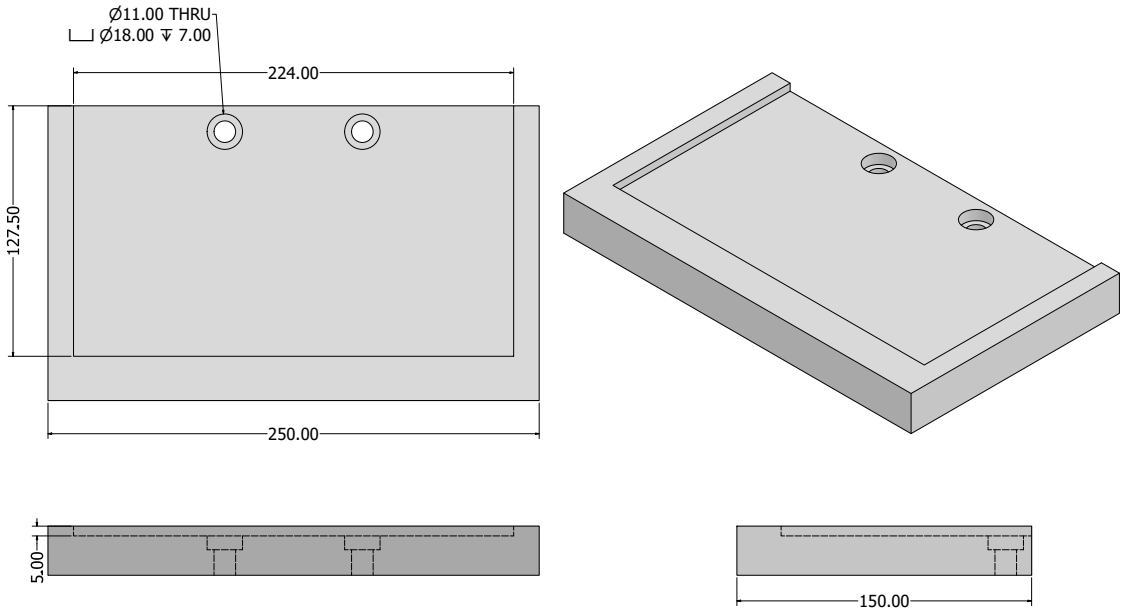


a)

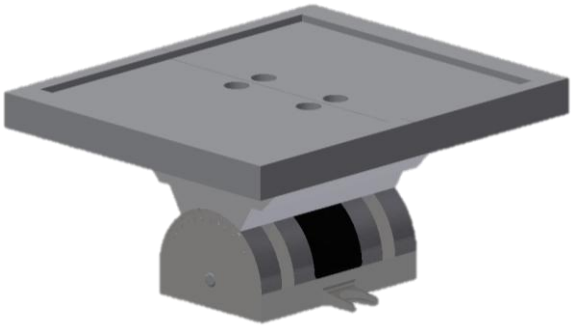

b)

*Appendix Figure C. 4. Adjustable angular fixture. a) 3D printed fixture drawings – Featuring various views (units in mm), b) Complete adjustable angular fixture design*

# C-4. Samples

## C-4.1. Curved Aluminium Sample

The sample designed and created using CAD was a curved aluminium sample. This sample was designed with a curvature and is presented in Appendix Figure C. 5.

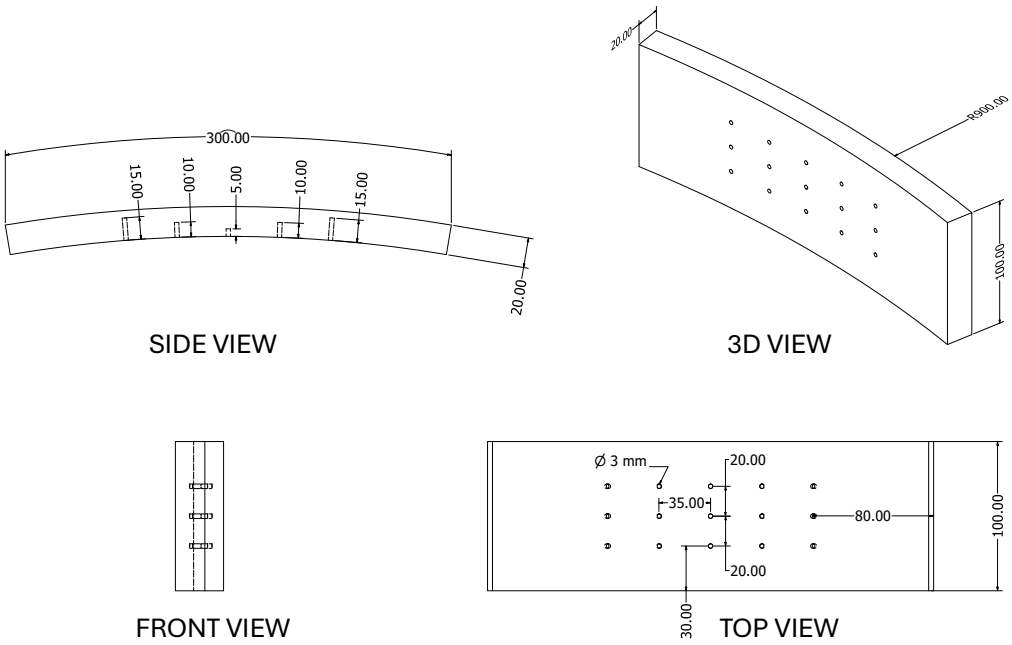


*Appendix Figure C. 5. Aluminium curved sample design drawings. – Featuring various views (units in mm)*

The sample was designed with an arc length of 300 mm, a width of 100 mm, and a thickness of 20 mm. The selected length provided sufficient space to incorporate manufactured defects while maintaining defect-free regions at both ends. The width of 100 mm was chosen to accommodate the ultrasonic roller probe, ensuring that the probe's side wheels remained fully supported on the sample during inspection. The thickness of

20 mm allowed for the various defect depths, while ensuring that the sample remained strong enough to not flex during inspection.

# C-5. Breakdown of Probe Assembly

Individual Drawings of the Assembly presented in Section C-2.3. Probe and Camera Mount.

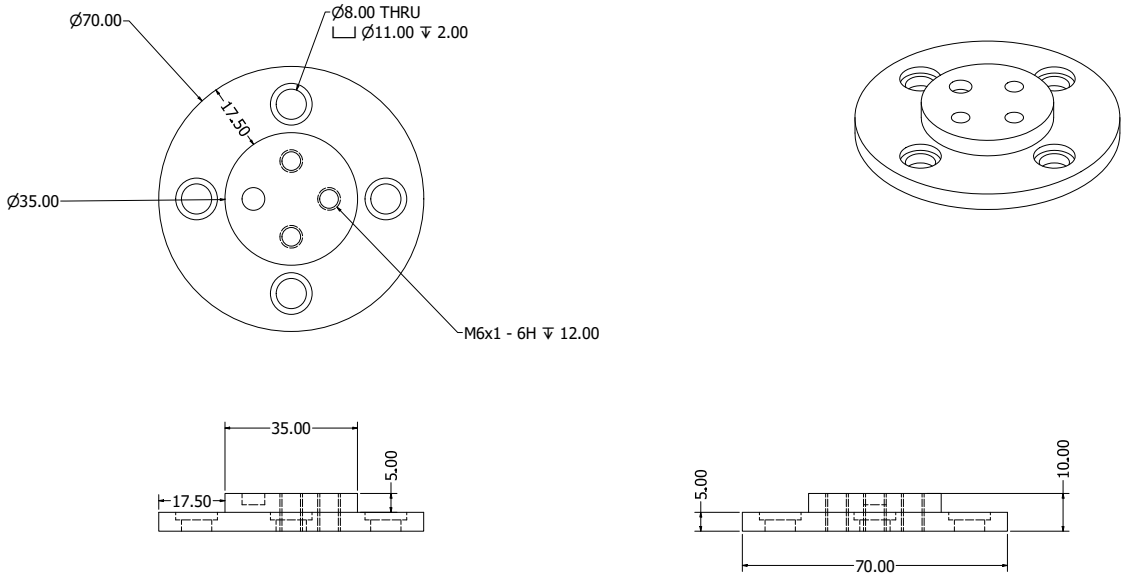


*Appendix Figure C. 6. Adapter Plate – LBR*

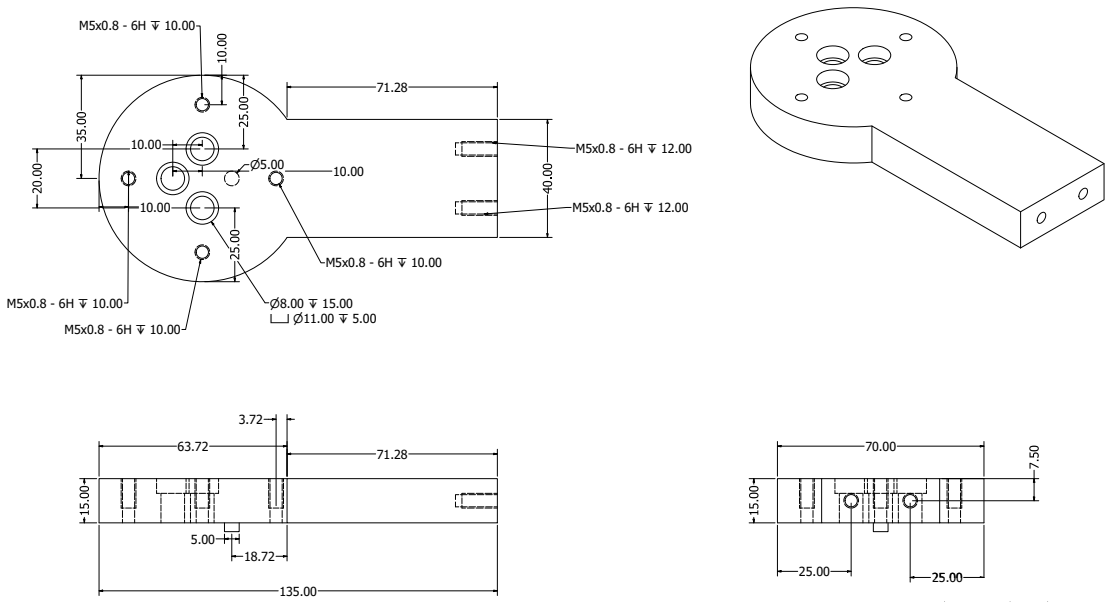


*Appendix Figure C. 7. Adapter Plate - Camera*

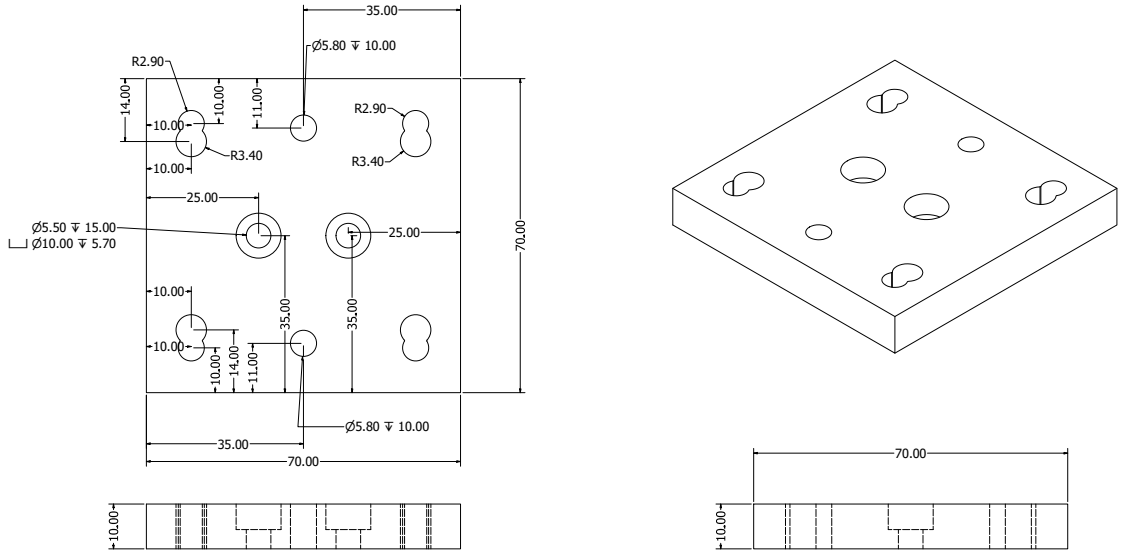


*Appendix Figure C. 8. Camera Mounting Plate*

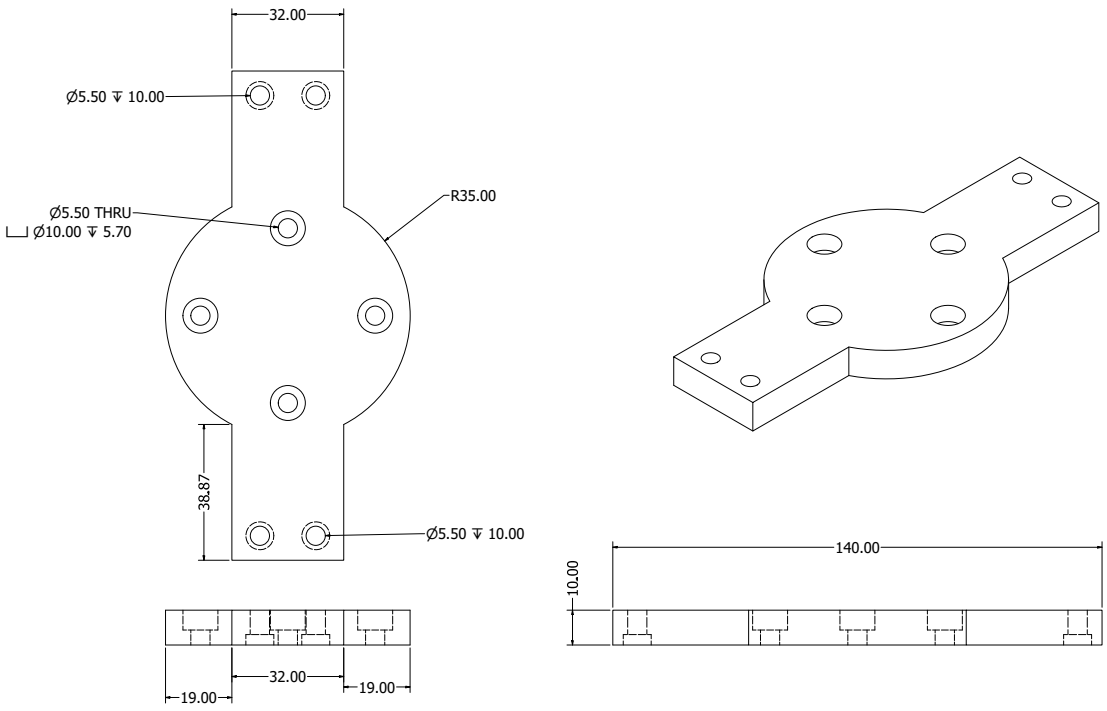


*Appendix Figure C. 9. Roller Probe Mount*

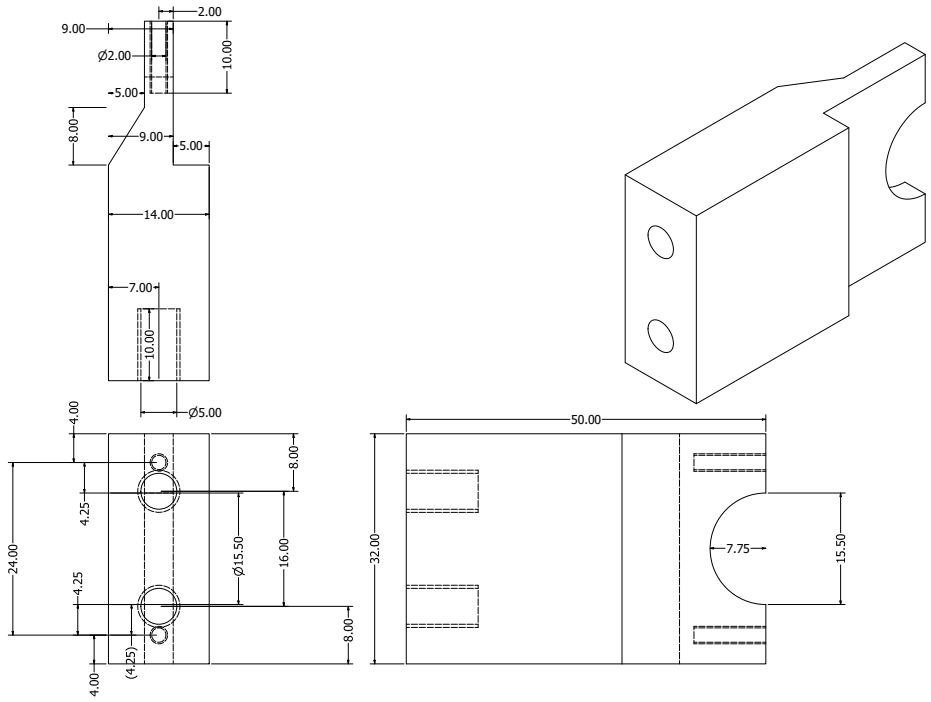


*Appendix Figure C. 10. Input Side Column*

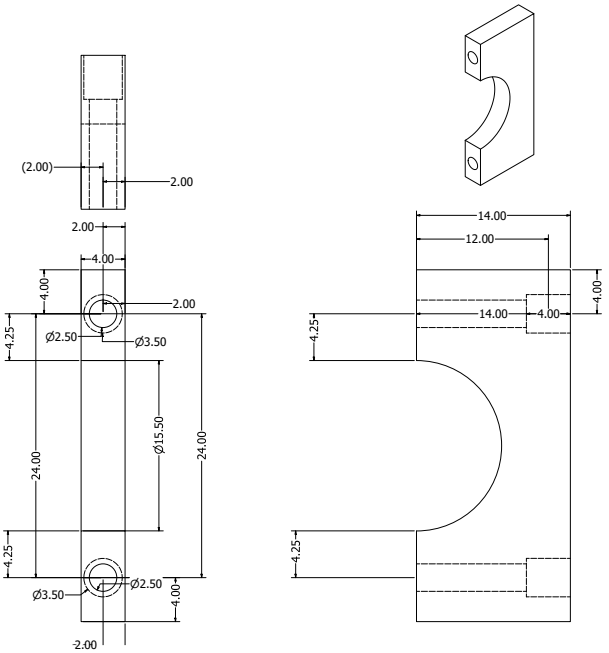


*Appendix Figure C. 11. Input Side Cap*

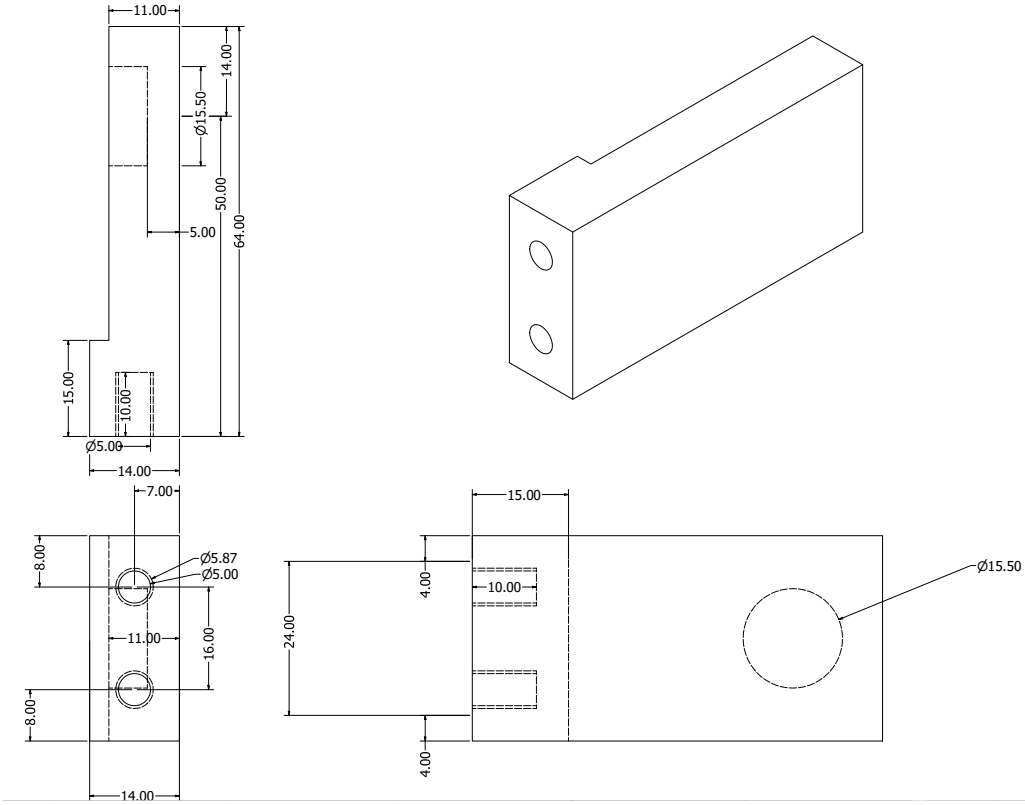


*Appendix Figure C. 12. Far Side Column*

# Appendix D – 6 dB drop CFRP plots

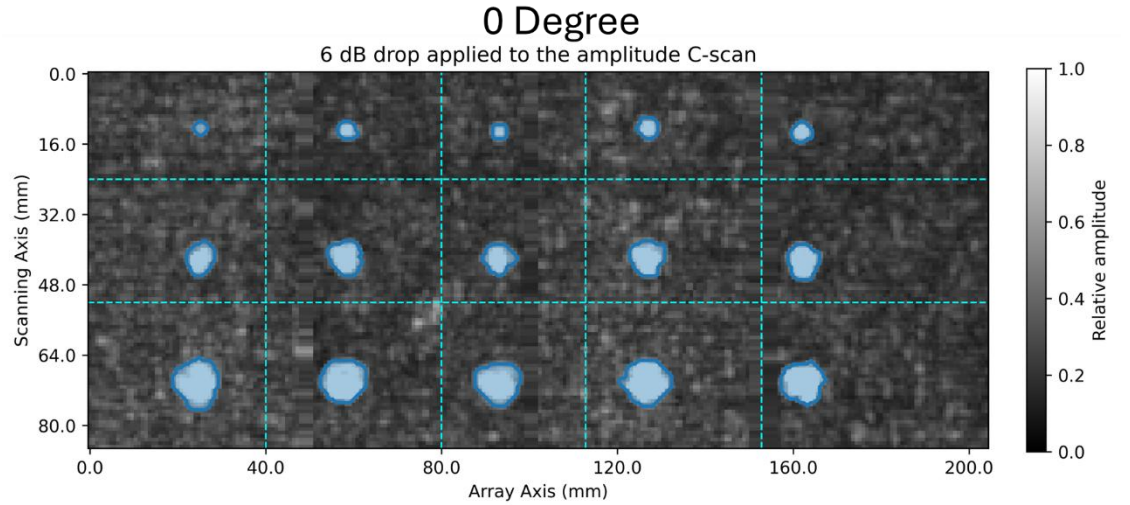


a)

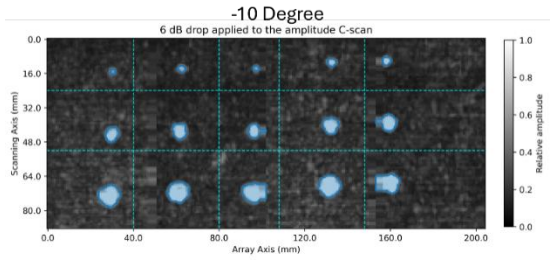


b)

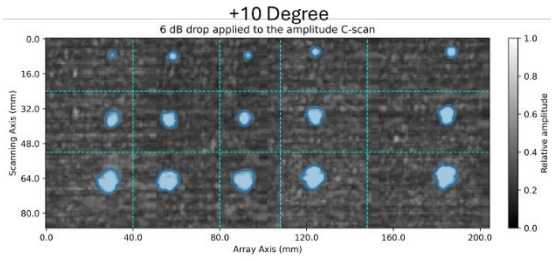


c)

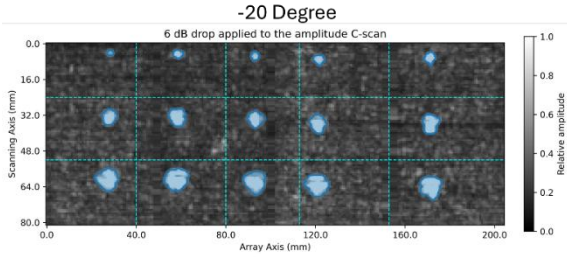


d)

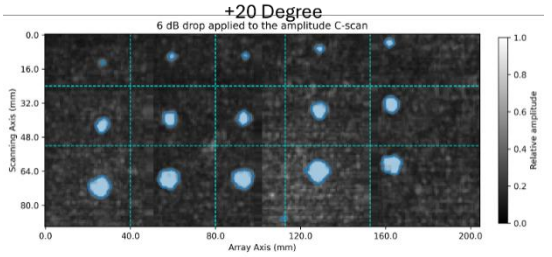


e)

# Appendix E – Full Generated Report

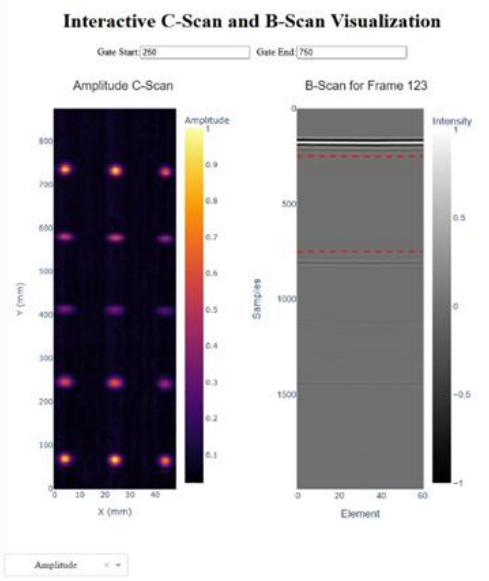


**Station 1 – 10:37 20-10-2025**

**Probe Data**

| Property | Value |
|---|---|
| Probe Name | 5L64 |
| Elements (X) | 64 |
| Elements (Y) | 1 |
| Voltage (V) | 80 |
| Gain (dB) | 40 |
| TVG (dB) | N/A |
| Sampling Frequency (MHz) | 100 |
| Centre Frequency (MHz) | 5 |
| Pitch (X) (mm) | 0.8 |
| Pitch (Y) (mm) | 1 |
| Width (X) (mm) | 0.4 |
| Width (Y) (mm) | 1 |
| Material Name | Aluminium |
| Longitudinal Velocity (m/s) | 6400 |
| Shear Velocity (m/s) | 3100 |

Show Less